POLITECNICO
MILANO 1863

SCUOLA DI INGEGNERIA INDUSTRIALE
E DELL'INFORMAZIONE

Tesi di Laurea Magistrale in
Mathematical Engineering - Statistical Learning
Ingegneria Matematica

# A New Feature Extraction Approach for Temporal Lobe Epilepsy Classification: Integrating Conventional Diffusion and Structural Network Metrics in a Multi-Scale Framework

Author:
**Elisa Broserà**

Student ID:
**10665925**

Advisor:
**Prof. Marta Gandolla**

Coadvisor:
**Dott. Alfonso Mastropietro**

Academic Year:
**2024-25**

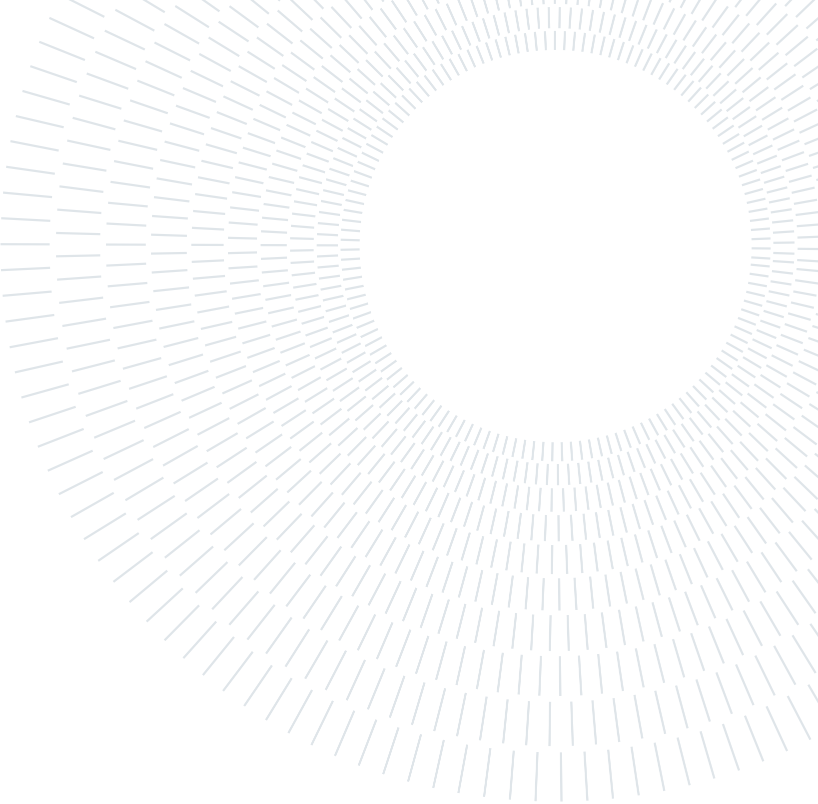

*Dedicated to my family.*

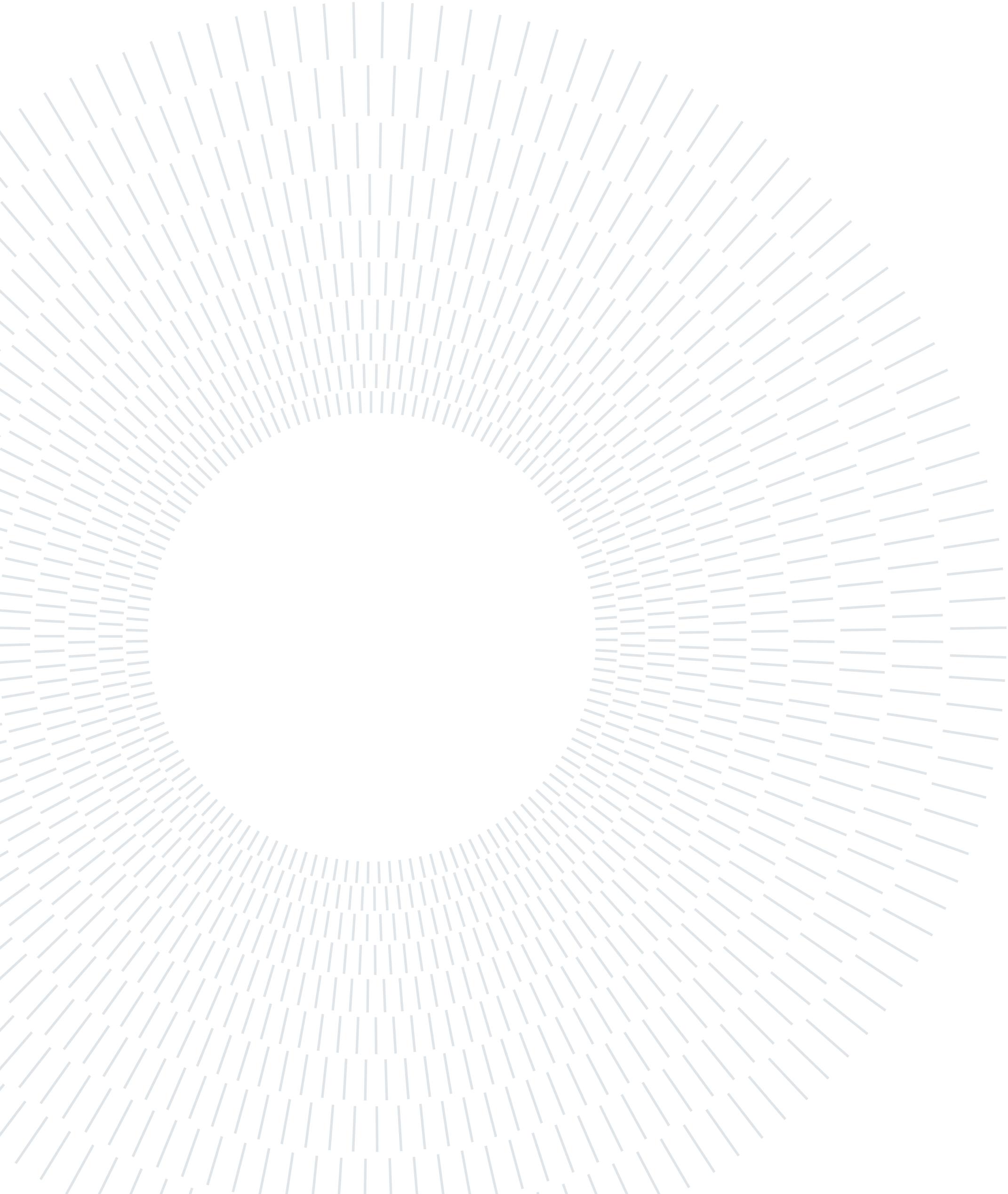

# Abstract

Temporal lobe epilepsy (TLE) is the most common drug-resistant form of epilepsy. TLE is increasingly understood not merely as a focal disorder, but as a large-scale network disease characterized by whole-brain alterations in connectivity. Using the Epilepsy Connectome Project (ECP) dataset (105 TLE, 76 HC), this thesis aims to optimally design the feature space for TLE classification by leveraging the significant differences in structural connectivity between TLE patients and healthy controls.

Our approach integrated conventional microstructural diffusion metrics with advanced network-based metrics derived from graph theory to quantify brain reorganization both locally and globally. The novelty of this work lies in the introduction of a multi-scale and multi-domain framework for feature extraction, which accounts for both anatomical and functional brain networks, such as the Limbic System and the Default Mode Network (DMN), notably the two most affected by TLE. By doing so, this work bridges the gap between advanced structural connectivity analysis and machine learning-based clinical classification.

Specifically, we developed a Machine Learning classification pipeline integrating the non-parametric Mann-Whitney U test and Spearman correlation for informed feature selection. Our final Support Vector Classifier (SVC) model, which combines local diffusion properties and global network topology derived from the hierarchical framework, reached mean cross-validation values of 84.4% for ROC-AUC, 75.3% for Balanced Accuracy and 78.6% for Recall, maintaining consistent performance on the independent test set and thus demonstrating the model's generalizability. These results confirm the efficacy of combining diffusion metrics and connectomics and demonstrate that feature design based on a multi-level hierarchical framework can effectively capture the complex pathological signatures of TLE.

**Keywords:** Temporal lobe epilepsy (TLE), conventional diffusion metrics, graph theory, structural connectivity, machine learning.

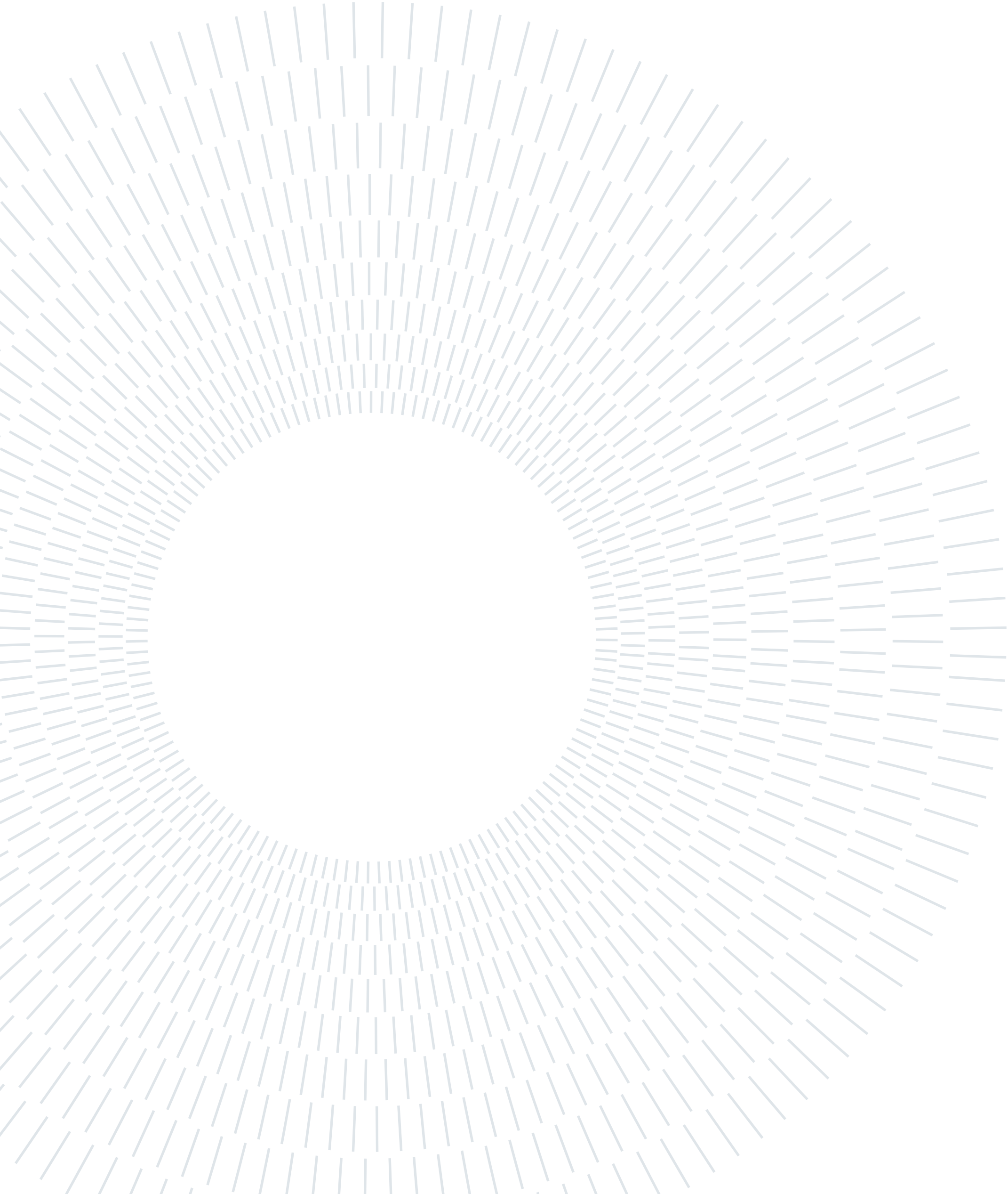

# Abstract in lingua italiana

L'epilessia del lobo temporale (TLE) è la forma più comune di epilessia farmaco-resistente. La TLE è oggi considerata non solo un disturbo focale, ma una patologia di rete, caratterizzata da alterazioni della connettività dell'intero encefalo. Utilizzando il dataset dell'Epilepsy Connectome Project (ECP) (105 TLE, 76 HC), questa tesi si propone di analizzare le differenze significative riguardanti la connettività strutturale tra pazienti con TLE e controlli sani, al fine di progettare in modo ottimale lo spazio delle variabili per la classificazione della patologia.

Il nostro approccio integra metriche di diffusione microstrutturale convenzionali con metriche di rete derivate dalla teoria dei grafi, per quantificare la riorganizzazione cerebrale sia a livello locale che globale. La novità di questo lavoro risiede nell'introduzione di un framework multiscala e multidominio per l'estrazione dei predittori, in grado di modellare sia le dinamiche delle reti cerebrali anatomiche che di quelle funzionali. Tra esse, il Sistema Limbico e la Default Mode Network (DMN) sono considerati i due sistemi più colpiti dalla TLE. Dunque, questo lavoro colma il divario tra l'analisi avanzata della connettività strutturale nella TLE e la classificazione clinica basata sul machine learning.

Nello specifico, abbiamo sviluppato una pipeline di classificazione basata sul Machine Learning che integra il test non-parametrico di Mann-Whitney e la correlazione di Spearman per la selezione delle feature. Il nostro modello finale, un Support Vector Classifier (SVC) che combina proprietà di diffusione locale e topologia di rete globale derivate dal framework gerarchico, ha raggiunto valori medi in cross-validation dell'84,4% per la ROC-AUC, del 75,3% per l'Accuratezza Bilanciata e del 78,6% per la Sensitività e ha mantenuto prestazioni coerenti sul test set indipendente, dimostrando così la generalizzabilità del modello. Infine, questi risultati supportano l'efficacia della combinazione di metriche di diffusione e connettomica e dimostrano che l'utilizzo dell'approccio a più livelli gerarchici anatomici e funzionali per la costruzione dello spazio delle variabili può catturare efficacemente le complesse dinamiche della TLE.

**Parole chiave:** epilessia del lobo temporale (TLE), metriche di diffusione classiche, teoria dei grafi, connettività strutturale, machine learning.

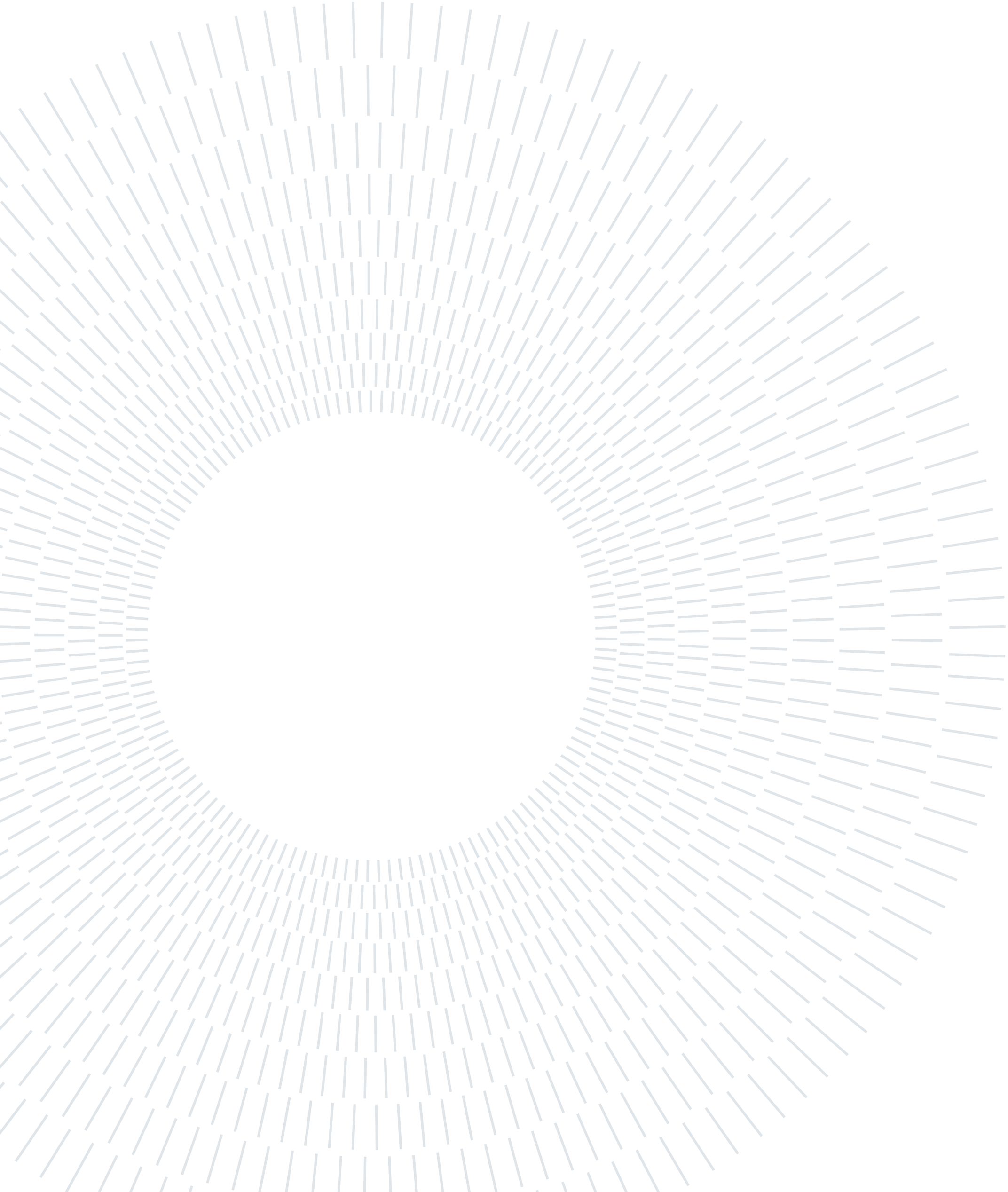

# Contents

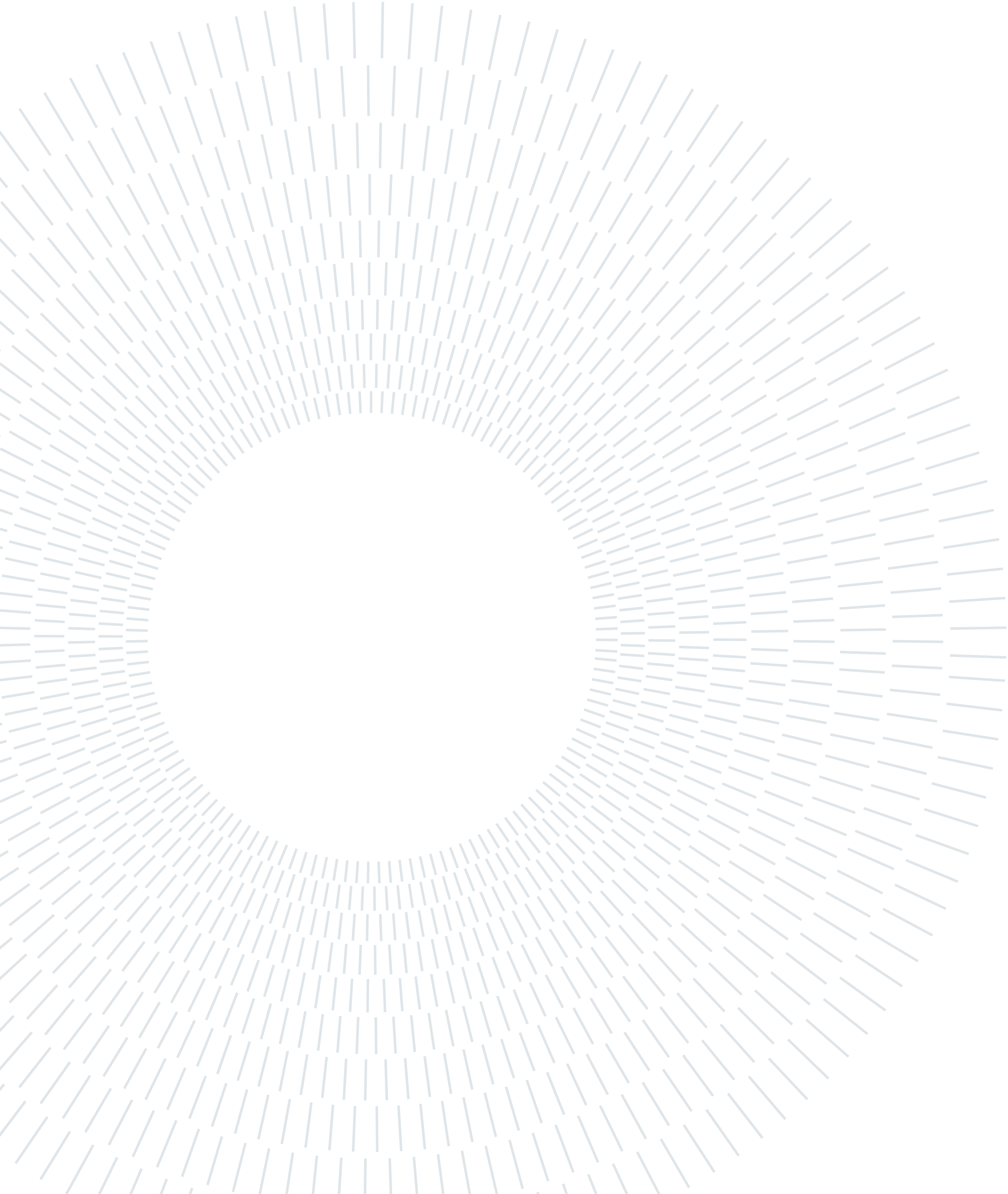

# 1 | Introduction

According to the World Health Organization (WHO), epilepsy is a chronic neurological disorder that by February 2024 affected approximately 50 million people worldwide. It is estimated that up to 70% of individuals suffering from epilepsy could live seizure free if properly diagnosed and treated. Nevertheless, nearly three-quarters of people with epilepsy that live in low-income countries do not receive adequate diagnosis or treatment. In addition, more than one-third of patients are resistant to antiepileptic drugs (AEDs) [19, 23], with the majority of these patients suffering from temporal lobe epilepsy (TLE). These statistics highlight the relevance of epilepsy in our society and underline the importance of deepening our understanding of this disease, particularly of drug-resistant forms such as TLE.

TLE usually originates in the mesial temporal structures, in particular the Hippocampus. Nevertheless, beyond the focal lesion, the pathological epileptic activity affects white matter integrity and topological organization across the entire brain, leading to substantial changes in structural brain connectivity [30]. Hence, it is nowadays recognized as a large-scale brain network disease whose dynamics can be described using graph theory [6].

The goal of this thesis is, first, to analyze the **significant differences in structural brain connectivity** between TLE patients and healthy controls using data from the *Epilepsy Connectome Project (ECP)*, focusing on both conventional diffusion-weighted imaging (DWI) metrics and network-based measures derived from graph theory. Second, we aim to **classify TLE vs controls** using a Machine Learning approach, exploiting optimally the findings related to structural significant differences to properly design the feature space.

To achieve these goals, we have explored in-depth the literature to understand how to preprocess the data and design the set of features for classification, which pipeline and models to employ and the results to expect. This work covers the entire process of transforming complex neuroimaging data into a structured set of features capable of capturing the subtle pathological signatures of TLE through Machine Learning techniques.

This thesis is organized as follows. Initially, we will give a clinical overview of epilepsy, with a specific focus on temporal lobe epilepsy. Building upon this clinical context, Chapter 3 establishes the theoretical foundations by explaining the mathematical principles behind structural connectivity reconstruction and its quantification, followed by an introduction to graph theory metrics for brain networks. Moreover, it explores the fundamentals of classification, specifically Support Vector Machines (SVM) and the relative performance evaluation metrics. In Chapter 4, we will review the literature about previous findings on diffusion and network-based alterations in TLE and classification between temporal lobe epilepsy patients and controls. The focus then shifts to the empirical data in Chapter 5, which introduces the ECP dataset, the preprocessing steps followed and the methods employed for the statistical analysis of connectivity differences and the design of the Machine Learning classification pipeline. The core results of this work are presented in the following two chapters: Chapter 6 presents the results of the structural connectivity analysis across groups, while Chapter 7 details the classification results, comparing the performance of models trained using as features first only diffusion metrics, then network-based metrics alone and finally joining both. Lastly, the thesis concludes with a discussion of our findings and critical analysis on the limitations and the future developments of this work.

# 2 | Epilepsy

## 2.1. Definition and epidemiology

A formal definition of epilepsy was first provided in 2005 by a Task Force of the International League Against Epilepsy (ILAE), which described epilepsy as *a disorder of the brain characterized by an enduring predisposition to generate epileptic seizures, and by the neurobiologic, cognitive, psychological, and social consequences of this condition.* According to this definition, epilepsy requires the occurrence of at least one epileptic seizure, defined as a transient occurrence of signs and/or symptoms due to abnormal, excessive, or synchronous neuronal activity in the brain. In December 2013, after extensive debate, the ILAE proposed a more operational and clinically oriented definition of epilepsy. *Epilepsy is a disease of the brain when any of the following conditions is met:*

- *At least two unprovoked (or reflex) seizures occurring more than 24 hours apart;*
- *One unprovoked (or reflex) seizure and a probability of further seizures similar to the general recurrence risk (at least 60%) after two unprovoked seizures, occurring over the subsequent 10 years;*
- *Diagnosis of an epilepsy syndrome. Epilepsy is considered to be resolved in individuals who had an age-dependent epilepsy syndrome and are now past the applicable age, or in those who have remained seizure-free for at least 10 years, with no antiseizure medication for the last 5 years.*

It is worth noting that after a first unprovoked seizure, the risk of recurrence is estimated to be between 40% and 52%. As seizures become more frequent, the probability of further recurrence increases. This observation explains why the operational definition places particular emphasis on the likelihood of experiencing subsequent seizures.

## 2.2. Seizures: what are they?

The process through which a healthy brain becomes capable of generating spontaneous seizures is referred to as *epileptogenesis*. This process is believed to result from an imbalance between excitatory and inhibitory neuronal activity. During an epileptic seizure, neuronal networks generate abnormal patterns of electrical activity: large populations of neurons may fire synchronously and at abnormally high frequencies. This pathological behavior disrupts normal brain function and, in severe or prolonged cases, may even lead to neuronal damage or cell death [37].

The frequency and duration of epileptic seizures play a crucial role in determining their impact on brain structure and function. Recurrent and prolonged seizures are associated with increasingly disruptive effects on neural networks, contributing to progressive structural and functional alterations.

## 2.3. Causes of Epilepsy

Epilepsy may arise from a wide range of causes, including genetic, structural, metabolic, immune, infectious, and unknown causes. According to the National Institute of Neurological Disorders and Stroke (NINDS), conditions that may lead to epilepsy include brain tumors, traumatic brain injury, chronic alcohol abuse or withdrawal, neurodegenerative diseases such as Alzheimer's disease, stroke, hypoxic-ischemic injury, vascular malformations, intracranial hemorrhage, brain inflammation, and infections such as meningitis, HIV-related infections and viral encephalitis. The precise mechanisms through which these diverse conditions lead to *epileptogenesis* are not fully understood. Much of the current knowledge derives from animal models of epilepsy, which employ epileptogenic brain insults, proconvulsant chemicals, electrical stimulation or traumatic brain injury to reproduce seizure activity [12, 32].

Importantly, epilepsy should be understood as both a cause and a consequence of brain atrophy. Recurrent seizures and network-level dysfunction contribute to the loss of neurons and synaptic connections, affecting both cortical and subcortical structures over time.

## 2.4. Classification of Epilepsy

Epilepsy classification is primarily based on the type of seizures experienced by the patient. Seizures are broadly divided into focal and generalized seizures, with several subtypes within each category.

Focal seizures originate within networks limited to one hemisphere of the brain and account for approximately 60% of epilepsy cases [27]. These seizures are often classified according to their region of onset, such as focal frontal lobe or mesial temporal lobe seizures. In contrast, generalized seizures arise from abnormal neuronal activity that rapidly engages bilateral brain networks from the onset.

According to National Institute of Neurological Disorders and Stroke (NIH), clinical manifestations vary widely depending on seizure type and brain regions involved. Some individuals remain fully conscious, while others experience impaired awareness. Symptoms may include motor phenomena such as sensory disturbances, emotional or psychic experiences, or automatisms such as repetitive movements or behaviors. Examples are blinks, twitches, mouth movements, or even walking in a circle.

The table here below summarizes this general introduction:

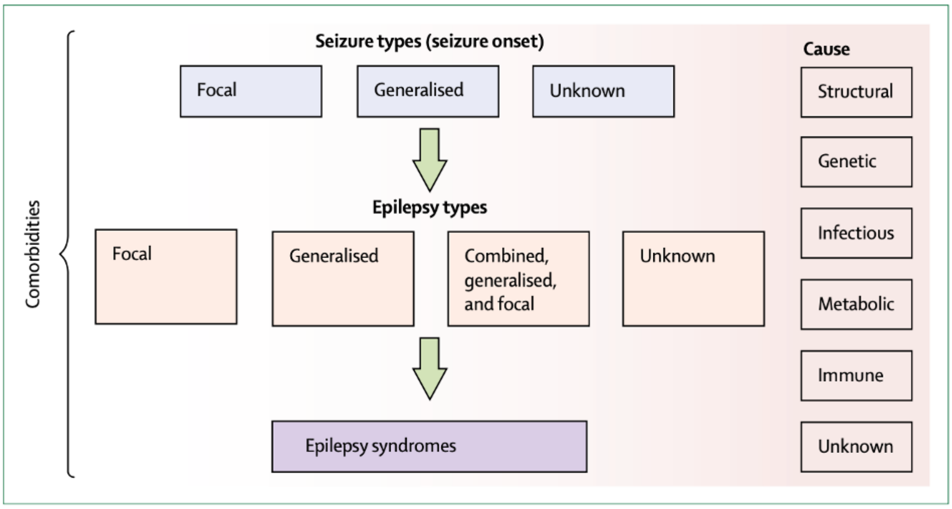

**Figure 2.1:** The International League Against Epilepsy framework for the classification of epilepsies. Source:[37]

## 2.5. Temporal Lobe Epilepsy

Temporal lobe epilepsy (TLE) is the most common and one of the best-characterized forms of focal epilepsy. It is frequently associated with mesial temporal sclerosis (MTS), an epileptogenic lesion characterized by neuronal loss and gliosis in the hippocampal formation and adjacent temporal lobe structures. Histopathological studies in patients with MTS have revealed [5, 36]:

- selective loss of excitatory and inhibitory neurons in specific hippocampal subregions
- axonal sprouting and synaptic reorganization

- alterations in glial cell function and structure

It is currently believed that an initial brain insult leads to neuronal loss in the Hippocampus. In response, surviving neurons undergo axonal sprouting, a compensatory process in which new axonal branches are formed. While this reorganization reflects neuroplasticity, it may also contribute to the formation of aberrant hyperexcitable circuits, further promoting seizure generation.

**BOX 1**: The Hippocampus
The Hippocampus is a key structure of the limbic system, which also includes the fornix, mammillary bodies, anterior thalamus, cingulum, and parahippocampal cortex. It plays a fundamental role in memory processes and exhibits material-specific lateralization: verbal memory is typically associated with the dominant (usually left) hemisphere, whereas non-verbal memory is more strongly linked to the non-dominant (usually right) hemisphere [13, 28].

## 2.6. Epilepsy as a Network Disease

Over the past decades, advances in histopathology, electrophysiology, and neuroimaging have progressively reshaped our understanding of epilepsy. In particular, it has become increasingly evident that in TLE the pathological substrate extends well beyond the Hippocampus, involving an interconnected network of limbic and extra-limbic brain regions. Early post-mortem studies primarily focused on the hippocampus and adjacent structures, such as the Amygdala, Entorhinal Cortex, Parahippocampal Gyrus, and Temporopolar Cortex. The advent of magnetic resonance imaging (MRI) revolutionized the study of epilepsy, enabling in vivo investigation of brain structure. Structural MRI studies from the early 2000s demonstrated not only hippocampal atrophy, but also gray matter loss in extra-temporal regions, including the Striatum, Frontal and Parietal Neocortex, and Bilateral Thalamus [3, 7].

Subsequent ex vivo analyses confirmed that histological abnormalities are not confined to mesial temporal structures but also involve the Thalamus and widespread neocortical regions. Diffusion MRI studies further revealed alterations in Fractional Anisotropy and Mean Diffusivity across major white matter bundles, both within and beyond temporo-limbic networks. Diffusion tensor imaging (DTI) and tractography have played a central role in reinforcing this network-based perspective. Given that this thesis is based on DTI data, these techniques and their derived metrics will be explained and discussed in detail in subsequent sections.

Structural abnormalities also impact functional connectivity, leading to a broad spectrum of cognitive, behavioral, and psychiatric comorbidities. Structural and functional connectivity are known to be statistically related, as highlighted by previous studies [9, 39]. Functional connectivity investigations using electroencephalography (EEG), magnetoencephalography (MEG), and functional MRI have consistently supported the concept of epilepsy as a network disorder. In TLE, although seizures often originate in the Hippocampus, epileptic activity frequently propagates to the Entorhinal Cortex, Lateral Temporal Regions, Inferior Frontal Cortex, and subcortical nuclei such as the Amygdala and Medial Thalamus.
Two functional networks that have been repeatedly reported to be altered in TLE are the Limbic System and the Default Mode Network (DMN).

Another compelling clinical observation which further supports the network-based view of epilepsy is that approximately 40% of drug-resistant patients continue to experience seizures even after surgical resection of the sclerotic tissue. This outcome strongly suggests that epileptic abnormalities are not confined to a single focal region but involve distributed neural circuits.
For these reasons, epilepsy has increasingly been described as a network disease, and graph theory has emerged as a powerful mathematical framework to characterize the topology and organization of brain networks.

In the following sections, we will introduce the theoretical foundations underpinning the data analysis presented in this thesis. We will first review diffusion MRI and DTI, along with the classical metrics derived from these techniques. We will then provide an overview of graph theory and its most relevant measures for brain network analysis. Only after establishing these foundations will we be prepared to introduce the dataset and the preprocessing steps.

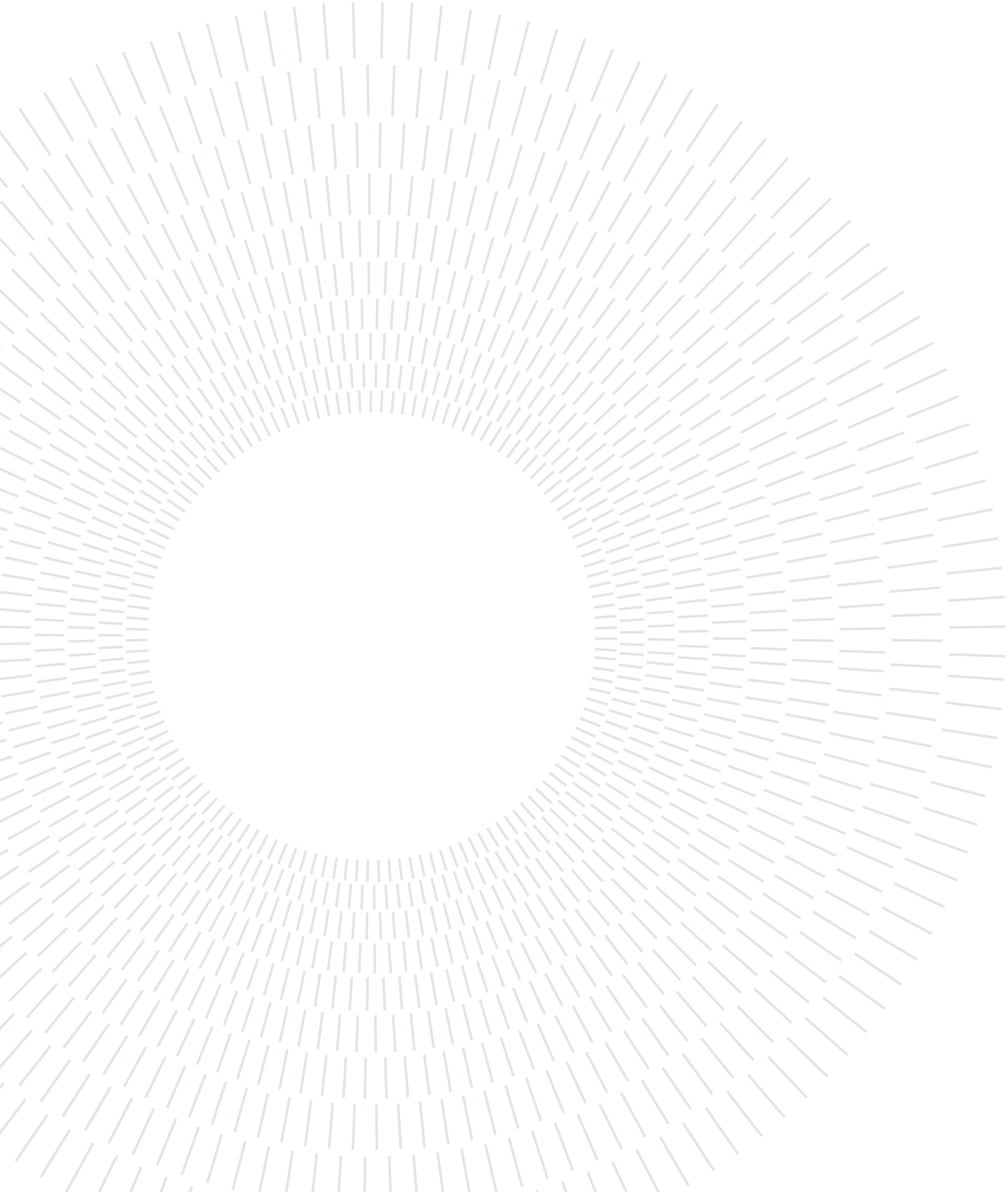

# 3 | Theorical Foundations

## 3.1. Diffusion MRI and Diffusion Tensor Imaging

### 3.1.1. From MRI to Diffusion MRI...

The human brain consists of more than 100 billion neurons and is arguably the most complex structure in our body. Imaging has been a powerful technique to navigate this vast entity and identify the locations where biological events of interest occur. MRI is probably the most famous and widely used imaging technique; it is noninvasive, three-dimensional and requires as little as a few minutes to characterize the entire brain anatomy. MRI is based on signals from 1H (proton) nuclei. While many molecules in our body contain protons, the most common is undoubtedly water. The brilliant intuition behind this technique is the use of a strong magnetic field to align the spins of water protons, which are then disturbed by radiofrequency pulses. As these protons return to their original state, they emit signals that are captured and transformed into high-resolution anatomical images. The contrast in these images is determined by the specific physical and chemical environment of the water molecules. As a matter of fact, the interest lies not in the water itself, but in the environment in which it is contained. That said, conventional MRI has a major limitation: contrast. Standard grayscale images often cannot distinguish between different anatomical regions with similar water properties [25].

Diffusion MRI (dMRI) overcomes this by adding a new dimension to imaging: the measurement of the microscopic Brownian motion of water molecules. By exploiting the differences in water diffusion, it becomes possible to map the anatomical micro-architecture of the human brain. This is possible because, while in a perfectly homogeneous medium water diffusion is random and equally probable in all directions, the human body is a complex environment. Specifically, in the brain, the diffusion of water molecules is determined by physiological factors, such as temperature, and by the microenvironmental structure, such as membranes and nerve fibers. In short, water acts as a probe for the cellular environment, where its random movement is restricted and shaped by biological structural barriers.

### 3.1.2. Molecular Diffusion

Diffusion is the random thermal motion of particles. The displacement distribution of molecules in a fluid depends on the time over which diffusion is being quantified, the fluid's viscosity, the temperature, any concentration gradients that might be present, and physical barriers the molecules might encounter. The random motion of molecules in a fluid due to the diffusion phenomenon is also called Brownian motion. The diffusion coefficient, D, can be used to describe the mean squared displacement of the diffusing water molecules per unit time. Here below Eistein diffusion equation [1]:

$$D = \frac{\langle \Delta r^2 \rangle}{2n\Delta t} \tag{3.1}$$

where D, once again, is the diffusion coefficient, r is the water molecules' displacement, n is the number of dimensions, Δ t is the diffusion time, which is the time over which the diffusion is being characterized. For example, the diffusion coefficient of pure water, in free space, at 20°C is roughly 2.0 x $10^{-3}$ $mm^2/s$ and increases at higher temperatures. While Einstein's equation provides a scalar summary of the diffusion's magnitude, it does not describe the spatial probability of finding a molecule at a specific location. In an environment without boundaries (free diffusion), this spatial distribution follows a Gaussian probability density function (PDF) [1]:

$$P(\Delta r, t_d) = \frac{1}{\sqrt{(4\pi D t_d)^3}} \exp\left(-\frac{\Delta r^2}{4Dt_d}\right) \tag{3.2}$$

Notice that the diffusion of particles increases with time.

However, within biological tissues, water diffusion is rarely free; instead, it is referred to as *hindered*. The interaction of water molecules with cellular membranes and organelles forces them to take tortuous paths. Consequently, diffusion in the brain does not theoretically follow a perfect Gaussian distribution.

Nevertheless, for the sake of simplicity, this behavior was often approximated as Gaussian in early **Diffusion Weighted Imaging (DWI)** techniques. In this context, the measured value is referred to as the Apparent Diffusion Coefficient (ADC). The ADC provides a single scalar value per voxel, representing the average water mobility regardless of direction.

In the brain, the ADC is heavily influenced by the local micro-architecture: in White Matter (WM), diffusion is highly *anisotropic*, occurring more easily along the longitudinal axis of the axons, whereas Gray Matter (GM) is typically less anisotropic and Cerebrospinal Fluid (CSF) exhibits isotropic diffusion [33].

While the ADC is a powerful tool in standard clinical settings, it fails to capture the directional information inherent in organized tissues. To overcome this limitation, **Diffusion Tensor Imaging (DTI)** was introduced by *Basser et al.* (1994). In the DTI framework, the simplification of a single scalar ADC is replaced by a $3 \times 3$ symmetric matrix: the Diffusion Tensor ($\mathbf{D}$). This shift allows us to move beyond measuring "how much" water diffuses, enabling a description of "in which direction" it moves.

The probability density function is thus generalized to a multivariate normal distribution [1]:

$$P(\mathbf{\Delta r}, t_d) = \frac{1}{\sqrt{(4\pi t_d)^3 |\mathbf{D}|}} \exp\left(-\frac{\mathbf{\Delta r}^T \mathbf{D}^{-1} \mathbf{\Delta r}}{4t_d}\right) \tag{3.3}$$

The tensor $\mathbf{D}$ represents the covariance of molecular displacements:

$$\mathbf{D} = \begin{bmatrix} D_{xx} & D_{xy} & D_{xz} \\ D_{yx} & D_{yy} & D_{yz} \\ D_{zx} & D_{zy} & D_{zz} \end{bmatrix} \tag{3.4}$$

To transform the tensor from the arbitrary coordinate system of the MRI scanner (X,Y,Z) to the intrinsic reference frame of the tissue, $\mathbf{D}$ is diagonalized to obtain three eigenvalues $(\lambda_1, \lambda_2, \lambda_3)$ and three corresponding eigenvectors $(e_1, e_2, e_3)$. Notice that the diffusion tensor D is a symmetric matrix, therefore it can always be diagonalized according to the spectral theorem.
Geometrically, these define a diffusion ellipsoid:

- The primary eigenvector $(e_1)$ points in the direction of maximum diffusivity of water, aligning with the dominant axonal orientation in white matter.
- The eigenvalues quantify the rate of diffusion along these principal axes, allowing for the calculation of parallel diffusion $(D_{\parallel} = \lambda_1)$ and perpendicular diffusion $(D_{\perp} = \frac{\lambda_2+\lambda_3}{2})$.

This provides a far more detailed description of tissue microstructure than the scalar ADC alone.

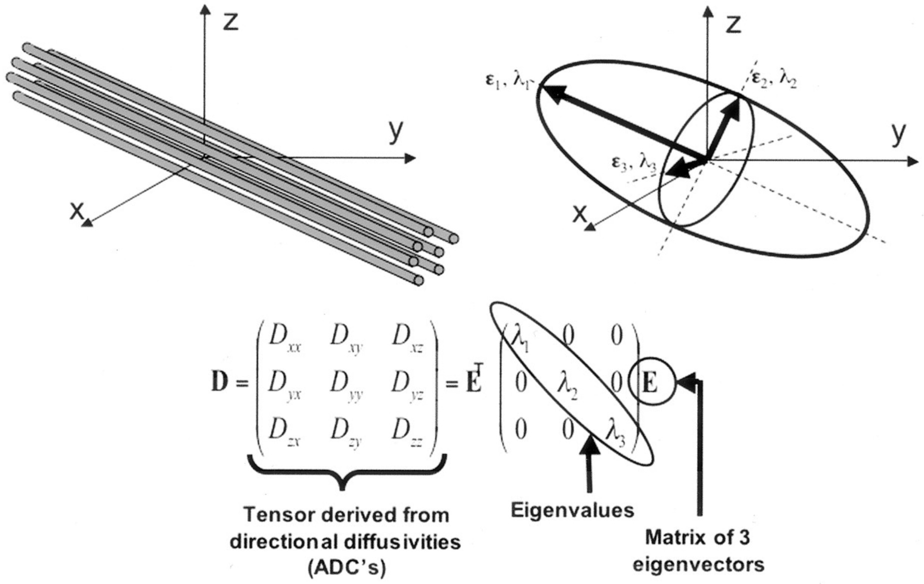

**Figure 3.1:** Top left: Fiber tracts have an arbitrary orientation with respect to scanner geometry (x, y, z axes) and impose directional dependence (anisotropy) on diffusion measurements. Top right: The three-dimensional diffusivity is modeled as an ellipsoid whose orientation is characterized by three eigenvectors ($e_1, e_2, e_3$) and whose shape is characterized three eigenvalues ($\lambda_1, \lambda_2, \lambda_3$). Bottom: This ellipsoid model is fitted to a set of at least six noncollinear diffusion measurements by solving a set of matrix equations involving the diffusivities (ADC's) and requiring a procedure known as matrix diagonalization. The major eigenvector reflects the direction of maximum diffusivity, which, in turn, reflects the orientation of fiber tracts. Source:[17]

### 3.1.3. How is the diffusion measured?

To translate these mathematical models into actual images, it is necessary to understand how the diffusion MRI signal is generated and how it is sensitized to water diffusion. As described by Mori and Zhang (2006), the contrast in magnetic resonance imaging is generated by multiple physical properties of water protons: proton density (PD), T1 and T2 relaxation times, and the diffusion coefficient ($D$). In a standard Spin-Echo sequence, the signal intensity ($S$) represents a combination of these factors:

$$S = PD \cdot \left(1 - e^{-TR/T1}\right) \cdot e^{-TE/T2} \cdot e^{-bD} \tag{3.5}$$

where $TR$ (Repetition Time) and $TE$ (Echo Time) are timing parameters that control the T1 and T2 weighting (see Appendix A), while $b$ is the diffusion-weighting factor, which

will be explained below.
The key points in this equation are:
(1) the magnitude of signal(S) is the information obtained from MR scanners;
(2) TR, TE, and b are imaging parameters that we can control, and by changing these parameters we can change the contribution (weighting) of T1, T2, and D terms to the signal;
(3) MR signal almost always contains a contribution from all four properties of water molecules.

This implies that it is impossible to compute the value of the diffusion coefficient D from a unique combination of TR, TE and b values. D and PD would both be unknown variables: indeed the proton density for each particular tissue is different. Hence, to isolate the diffusion term ($D$), the following approach is employed: we keep $TR$ and $TE$ constant, hence fixing the T1 and T2 effects, and we can acquire images with different $b$-values to measure the signal attenuation caused solely by diffusion.

### 3.1.4. Pulsed Gradient Spin Echo Sequence and the b-value

The measurement of diffusion is typically performed using the Pulsed Gradient Spin Echo (PGSE) sequence, with a single-shot, echo-planar imaging (EPI) readout. With respect to a standard Spin Echo (SE) sequence, PGSE introduces a pair of strong magnetic field gradient pulses to sensitize the MR signal to molecular motion.
Here below its main steps:

1. A first 90° radiofrequency pulse (RF) moves the magnetization from the longitudinal to the transverse plane. Only signal in this plane can be detected by MRI. This is the same in SE sequence.
2. The first gradient pulse introduces a phase shift across the water molecules depending on their position.
3. A 180° radiofrequency pulse inverts the spins.
4. After a diffusion time $\Delta$, a second gradient pulse (identical to the first) is applied to reverse the phase shift.

The signal generated from PGSE is then collected using an Echo-Planar Imaging (EPI) readout. Unlike standard sequences that acquire data line-by-line, EPI captures an entire slice of the brain in a single "shot".

EPI is most widely used DWI method. It is fast, efficient and insensitive to small motion and is readily available on most clinical MRI scanners. Being so fast, it captures water diffusion optimally by "freezing" tiny movements. However, this speed comes at a cost: EPI is sensitive to magnetic field inhomogeneities. Hence, the resulting images may suffer from artifacts. In this thesis, we will not delve into image correction methods, although they are commonly used to deal with these effects.

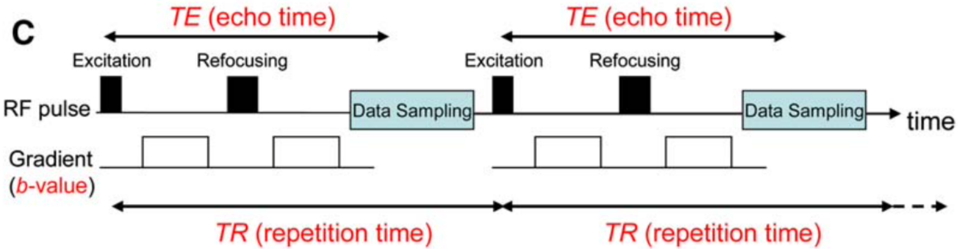

**Figure 3.2:** Gradient Pulse Spin Echo (GPSE) sequence. The TE (echo time) and TR (repetition time) are related to the timing of the radio-frequency (RF) pulse and b values are related to the pair of pulsed field gradients. By changing these parameters, the contribution (contrast) of proton density (PD), T1, T2, and diffusion weighting can be controlled. Source:[25]

If the water molecules are stationary, the second gradient perfectly refocuses the signal and all particles are in phase. However, if the molecules move during the time interval $\Delta$, the refocusing is incomplete (Figure 3.3). Because the signal at each pixel represents the sum of the signals from all the water molecules in that pixel, the incomplete refocusing leads to signal loss.

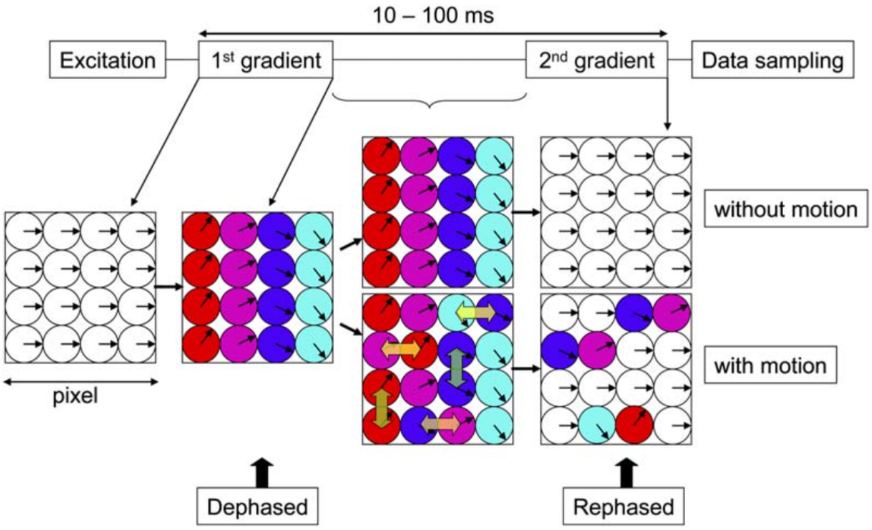

**Figure 3.3:** Relationship between water diffusion and Gradient applications. If water molecules move in between the two gradient applications, the second gradient cannot perfectly refocus the phases, which leads to signal loss. Source:[25]

As for term b, it is related to the gradient application. The most intuitive way to control b is to change the strengths and timeframes of two gradient pulses. The longer the separation is, the more time there is for water to move around, which would lead to more signal loss. The exact formula of b is not included here. As we already said, two MRI measurements with different b values are needed to determine a diffusion coefficient, along the direction of the gradient.

### 3.1.5. Reconstruction of Fiber Orientation

One of the main features of diffusion MRI is that it detects water motion only along the applied gradient axis. Although the MRI system can combine X, Y, and Z gradients to measure the ADC along any arbitrary orientation by switching the physical gradients on and off simultaneously, a simple set of three orthogonal measurements is only sufficient to calculate the ADC along those specific axes and the Mean Diffusivity.

To fully reconstruct the 3D diffusion ellipsoid and determine the precise orientation of fibers that are not aligned with the scanner's axes, the diffusion tensor model must be applied. This requires a minimum of six non-collinear directions to solve for the six independent degrees of freedom of the tensor matrix $\mathbf{D}$, which is a $3 \times 3$ symmetric matrix with six unknown entries.

Once the MRI signal is recorded for each of the six directions (typically using at least two different b-values to retrieve the ADC), the tensor is reconstructed. Mathematically, the ADC measured along a specific gradient direction $\mathbf{g} = [g_x, g_y, g_z]$ is the projection of the tensor $\mathbf{D}$ along that direction. This relationship is expressed as:

$$\begin{aligned} ADC = \mathbf{g}^T\mathbf{D}\mathbf{g} &= \begin{pmatrix} g_x & g_y & g_z \end{pmatrix} \begin{pmatrix} D_{xx} & D_{xy} & D_{xz} \\ D_{xy} & D_{yy} & D_{yz} \\ D_{xz} & D_{yz} & D_{zz} \end{pmatrix} \begin{pmatrix} g_x \\ g_y \\ g_z \end{pmatrix} \\ &= g_x^2 D_{xx} + g_y^2 D_{yy} + g_z^2 D_{zz} + 2g_x g_y D_{xy} + 2g_x g_z D_{xz} + 2g_y g_z D_{yz} \end{aligned} \tag{3.6}$$

After having acquired six (one per direction) ADC values for each voxel, we obtain a linear system of six equations with six unknown variables. Solving it, we get the six unknown entries of $\mathbf{D}$.

Finally, the tensor can be diagonalized to find its principal axes and the rate of diffusion along those. In this way, as explained above, an ellipsoid can be drawn. It is worth recalling that the dominant eigenvector corresponds to the direction of maximum diffusion and biologically to the orientation of the white matter tracts.

### 3.1.6. Classical Diffusion Metrics

Once the tensor D is diagonalized, we have three eigenvalues ($\lambda_1, \lambda_2, \lambda_3$) and three corresponding eigenvectors ($e_1, e_2, e_3$). These values quantify the magnitude of water diffusion along the three directions, which are the principal axes of the ellipsoid. Unfortunately, displaying this vast amount of information, in a single visualization, is challenging even in a 3D space. This leads to a question: how can we summarize and represent these values significantly? Here below, two answers are represented: *scalar maps* and color-*oriented diffusion maps.*

First we derive the most common *quantitative diffusion metrics* used in clinical and research settings: Mean Diffusivity (MD) and Fractional Anisotropy (FA).

- Mean Diffusivity (MD):
  The MD, also called the Apparent Diffusion Coefficient (ADC), is the measure of the total amount of diffusion within a voxel, regardless of its direction. It is the average of the three eigenvalues:

  $$MD = \frac{\lambda_1 + \lambda_2 + \lambda_3}{3} \tag{3.7}$$

High MD values typically indicate the presence of free water or tissue degradation, such as necrosis. Here, cellular barriers are either compromised or not so present at all.

- Fractional Anisotropy (FA):
  The FA is a scalar index (ranging from 0 to 1) that measures the degree of anisotropy. It describes how much the diffusion ellipsoid is "stretched". FA is rotationally invariant.

$$FA = \sqrt{\frac{3}{2}} \frac{\sqrt{(\lambda_1 - MD)^2 + (\lambda_2 - MD)^2 + (\lambda_3 - MD)^2}}{\sqrt{\lambda_1^2 + \lambda_2^2 + \lambda_3^2}} \tag{3.8}$$

  FA $\approx$ 0: Diffusion is isotropic (spherical shape), typical of cerebrospinal fluid (CSF) or gray matter.
  FA $\approx$ 1: Diffusion is anisotropic (cigar shape), typical of white matter where myelin and axonal membranes hinder movement perpendicular to the fiber.

These are slightly less common but very useful metrics:

- Radial Diffusivity (RD):

$$RD = \lambda_2 + \lambda_3 \tag{3.9}$$

- Axial Diffusivity (AD):

$$AD = \lambda_1 \tag{3.10}$$

  RD and AD have been shown to be related to brain pathology. In particular, DR appears to be modulated by myelin in white matter tracts, whereas AD is sensitive to axonal degeneration [34].

Let's now move on with *color-oriented diffusion maps.* After the diagonalization of the diffusion tensor for each voxel, the principal eigenvector, $e_1$ , can be mapped to a color based on its 3D orientation. By assigning red to the X axis, green to the Y and blue to the Z, each voxel can be mapped to specific color, based on the direction of maximum diffusivity.

However, a simple color map of eigenvectors would be noisy in regions with low anisotropy and very hard to interpret. To solve this, the color information is typically scaled by the Fractional Anisotropy (FA). The brightness of the color is proportional to the FA value: pixels with high anisotropy (white matter tracts) appear bright, while isotropic regions appear dark.

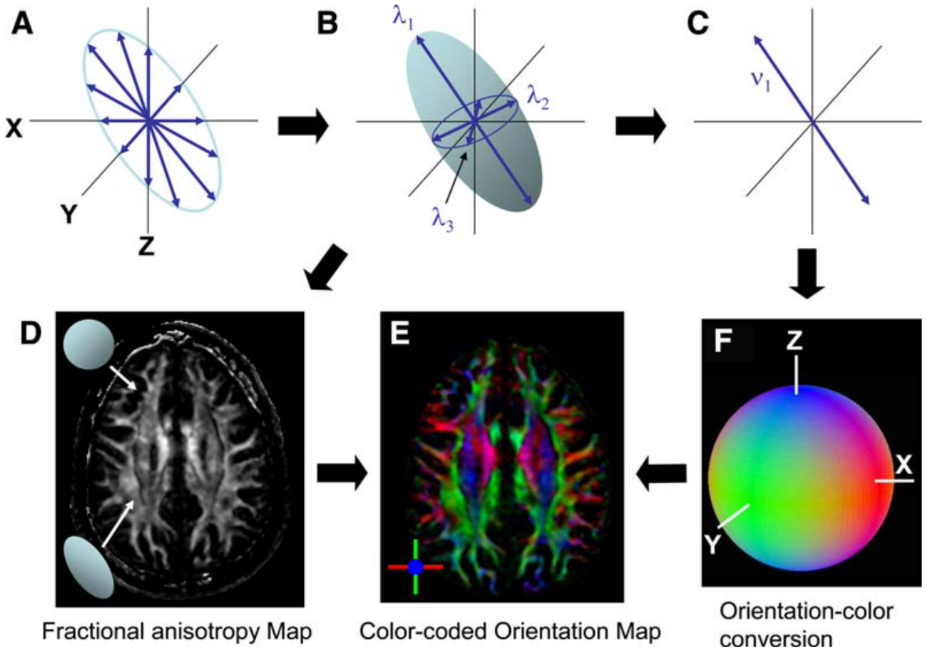

**Figure 3.4:** From diffusion measurements along multiple axes (A), the shape and the orientation of a 'diffusion ellipsoid' is estimated (B). An anisotropy map (D) can be created from FA values, which reflect the shapes of voxel-wise ellipsoids. Dark regions are isotropic (spherical), whereas bright regions are anisotropic (cigar-shaped). From the estimated ellipsoid (B), the orientation of the longest axis can be found (C), which is assumed to represent the local fiber orientation. This orientation information is converted to a color (F) at each pixel. By combining the intensity of the anisotropy map (D) and color (F), a color-coded orientation map is created (E). Source:[25]

### 3.1.7. Tractography

The last family of parameters that can be extrapolated from DTI data is based on the primary eigenvector of diffusion to obtain three-dimensional representations of white matter fiber bundles, the so-called, WM tractography [33]. This method reconstructs streamlined information from the tensor field and builds 3D trajectories of fiber pathways. Tractography processing has three main phases: seeding, propagation, and termination. Seeding consists of defining the points from which the streamlines will be drawn; one of the most common methodologies is defining Regions of Interest (ROIs) from which the fiber bundle is drawn. The ROIs can be manually selected or automatically extracted using anatomical atlases that define standard regions.

During the propagation process the fibers are gradually generated. Once a seed point is chosen, the algorithm follows the direction of the principal eigenvector to take a small step. At each new position, the direction is re-evaluated and another tiny step is taken, and so on, until the tract is terminated. There are different algorithms of fiber tracking and two main categories: deterministic and probabilistic. Deterministic tractography reconstructs one fiber from each seed, always choosing the direction of maximum diffusivity. On the other hand, probabilistic approaches take into account the uncertainty of the estimation and follow multiple possible fiber directions emanating from each seed.

The last tractography step is termination of the fiber tracking based on some termination criteria. The common termination criteria are minimum FA thresholds (typically 0.1–0.3 in adult brain and 0.1 in infant) and turning angle threshold (typically 40–70°, depending on the pathway).

It is important to note that the DTI model assumes, unrealistically, that each voxel contains only one fiber population. However, crossing, diverging or kissing fibers do exist. More complex methods exist to mitigate this issue, but won't be explained here.

### 3.1.8. Brain structural connectivity and connectivity matrix

As we described in the previous section, tractography is the computational method that estimates the anatomical trajectories of the white matter fiber pathways from dMRI data. Thanks to it, it is possible to visualize brain structural connectivity in a 3D space.

In section 2.6, we have explained why TLE can be treated as a network disorder. To move from a purely visual representation to a quantitative model of the brain as a network, it is necessary to adopt a connectome-based approach. Here below we will give an overview of what a so called *connectivity matrix* is and how it can be constructed from tractography.

According to *Zhang et al.* [43], quantitative tractography can falls into two broad categories:

- **Tract-specific analysis:** A hypothesis-driven approach that studies particular anatomical fiber tracts (e.g., the arcuate fasciculus).
- **Connectome-based analysis:** A data-driven approach that investigates the structural connectivity of the entire brain. This method is fundamental for studying TLE: it allows us to study the brain as a comprehensive map of neural connections, known

as the *structural connectome* or *connectivity matrix*. Hence, we will focus on this approach both in this theoretical introduction and in the actual data analysis part.

The construction of a structural connectome involves three processing steps: Tractography Correction, Tractography Segmentation (Parcellation), Tractography Quantification [43]. These steps are shared for both Tract-specific and Connectome-based analysis approaches.

### 1. Tractography Correction

The first step involves correcting potential biases such as the Correction Density bias, the Gyral bias and the false positive connections, inherent in the reconstruction process.

### 2. Tractography Segmentation (Parcellation)

The goal of segmentation is to identify white matter pathways that are meaningful for quantification of brain structural connectivity. In a connectome-based framework, this is typically achieved through parcellation of the whole-brain tractogram. There are two main categories: *cortical-parcellation-based* methods and *fiber clustering* methods.
*Cortical-parcellation-based* methods are the most commonly used. In this approach, a brain parcellation scheme is chosen to subdivide the gray matter into N discrete regions of interest (ROIs). Common atlases are Desikan-Killiany atlas (available in FreeSurfer), the Automated Anatomical Labeling (AAL) atlas or the Schaefer atlas. Then, these atlases, are automatically aligned to the subject space via image registration. Finally, only the streamlines that connect each pair of ROIs are extracted. This is how tractography is segmentated.

### 3. Tractography Quantification

The final step is the extraction of quantitative indices to describe the identified connections. The most common indexes are:

- **Streamline Count (NOS):** The total number of reconstructed fibers connecting two regions, often used as a proxy for connectivity density.
- **Microstructural Metrics:** The average, the maximum, or minimum value of a DTI-derived metric along the each fiber, such as Fractional Anisotropy (FA) or Mean Diffusivity (MD), which reflect the integrity and health of the white matter connection. It is also possible to recover the entire distribution of values of a classical diffusion metric along each tract.

The quantitative measures extracted for each individual fiber pathway can also be used to construct a structural connectivity matrix. This N×N symmetric matrix has as many rows and columns as the number of ROIs defined during the parcellation step. Each entry $A_{ij}$ represents the scalar metric (e.g. Streamline Count, FA or MD) associated with the connection between two specific regions, i and j.

Once this matrix is obtained, the structural organization of the brain can be rigorously analyzed using the mathematical tools of graph theory. In fact, there exists a bijective relation between every connectivity matrix and its corresponding graph. This implies that each ROI is actually a node in the network and the connection between them is an edge. The corresponding quantitative metric defines the weight of the edge joining the two nodes.

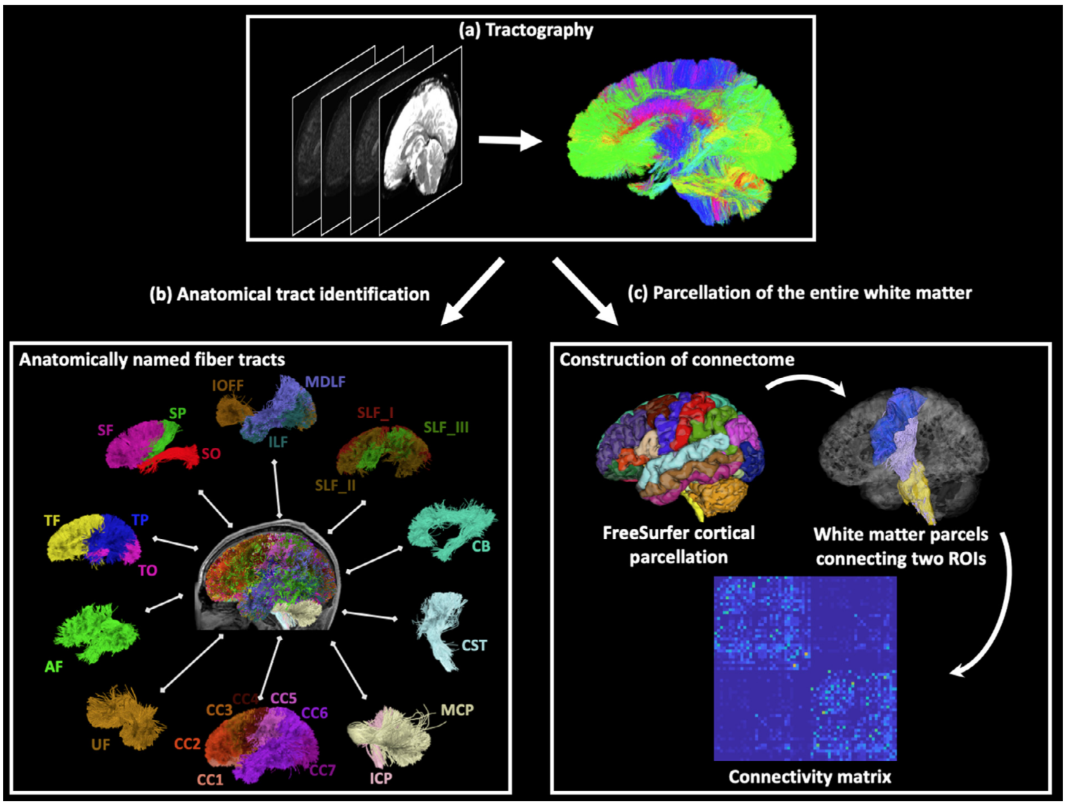

**Figure 3.5:** Tractography segmentation: (a)whole-brain tractogram computed by performing tractography in DWI data; (b)example anatomical tracts extracted from the tractogram; (c)example structural connectivity matrix constructed by performing tractography segmentation between all pairs of FreeSurfer cortical regions. Source:[43]

## 3.2. Graph Theory

In graph theory, a network G is a “set of nodes or vertices (V) and edges or lines (E) between them” [9]. In symbols, G=(V, E). Networks are classified as either *binary* or *weighted* and either *directed* or *undirected.*
The first property refers to how the "importance" of a connection is represented. If a network is binary, the edges are unweighted: they either exist or they do not. In terms of the adjacency matrix, $A_{ij}$=1 if a connection exists between node i and node j, and $A_{ij}$=0 otherwise. Conversely, if a network is weighted, edges are weighted: they carry a numerical scalar value that reflects the strengths of connection.
The second characteristic is the direction of connections. In a directed network, the connection from node i to node j is distinct from the connection from j to i. In an undirected network, the connections from i to j and from j to i coincise: edges lack direction.

Since Diffusion MRI cannot distinguish the biological direction of axonal propagation, the structural brain networks analyzed in this thesis are modeled as weighted and undirected graphs. A weighted undirected network G may be summarized by a squared adjacency matrix A having N rows and columns, where N is the number of nodes, and each entry $a_{ij}$ equal 0 if there isn't a connection between the pair of nodes $(i, j)$ or $>$0 otherwise.
Networks' topological properties can be described using a variety of summary statistics. Below, the most relevant local and global estimators, and a few network properties, are explained.

### 3.2.1. Local Summary Statistics

**Node Degree and Strength** The degree $k_i$ of a node $i$ is the number of edges connected to it. In a weighted network, instead of the degree, we use the nodal strength $s_i$, defined as the sum of the weights of all edges connected to node $i$:

$$s_i = \sum_{j \in V} a_{ij} \tag{3.11}$$

where $a_{ij}$ is the weight of the edge between nodes $i$ and $j$. Nodes with a high degree or strength are identified as *hubs.*

**Shortest Path Length** The shortest path length (or geodesic distance) $d_{ij}$ between nodes $i$ and $j$ is the minimum number of edges (for binary networks) or the minimum sum of edge weights (for weighted networks) required to connect them. It represents the most efficient route for information transfer between two regions.

**Centrality Measures** Centrality measures the relative importance of a node within the network. Two common measures are:

- **Betweenness Centrality ($BC$):** The fraction of all shortest paths in the network that pass through node $i$. It identifies nodes that act as "bridges" between different regions:
$$BC_i = \frac{1}{(n-1)(n-2)} \sum_{h \neq j \neq i \in V} \frac{\sigma_{hj}(i)}{\sigma_{hj}} \tag{3.12}$$
where $\sigma_{hj}$ is the total number of shortest paths from $h$ to $j$, and $\sigma_{hj}(i)$ is the number of those paths passing through $i$.

- **Closeness Centrality:** The inverse of the average shortest path length from node $i$ to all other nodes, representing how "close" a node is to the rest of the network:
$$CC_i = \frac{n-1}{\sum_{j \neq i} d_{ij}} \tag{3.13}$$

**Nodal and Local Efficiency** Efficiency describes the ability of processing and exchanging information.

- **Nodal Efficiency ($E_{nodal}$):** Measures how well a specific node is integrated into the network:
$$E_{nodal}(i) = \frac{1}{n-1} \sum_{j \neq i \in V} \frac{1}{d_{ij}} \tag{3.14}$$

- **Local Efficiency ($E_{loc}$):** Measures the degree of information exchange of the subnetwork composed of node i and its immediate neighbours. It characterizes the efficiency of information transfer limited to the local neighborhood.

**Clustering Coefficient** The clustering coefficient measures to which extend nodes in a graph tend to cluster together. For a binary network, the local clustering coefficient of a node is the ratio of the number of actual edges between its neighbors to the number of possible edges between them:
$$C_i = \frac{2e_i}{k_i(k_i-1)} \tag{3.15}$$
where $e_i$ is the number of connected pairs between the neighbors of node i.

In weighted networks, the weighted clustering coefficient accounts for edge weights, typically defined as:

$$C_i^w = \frac{1}{s_i(k_i - 1)} \sum_{j,h} \frac{a_{ij} + a_{ih}}{2} a_{jh} \tag{3.16}$$

where $s_i$ is the nodal strength. High clustering indicates high functional segregation.

**Eigenvector Centrality** Eigenvector centrality (EC) measures a node's influence by considering not just the quantity, but the quality of its connections. A node has high EC if it is connected to other nodes that are themselves eigenvector central.
It is defined as the i-th component of the eigenvector x corresponding to the largest eigenvalue $\lambda$ of the adjacency matrix A:

$$EC_i = \frac{1}{\lambda} \sum_{j \in V} a_{ij} x_j \tag{3.17}$$

To ensure comparability across networks of different sizes, the eigenvector is typically normalized such that its norm is 1 ($||x||$=1).

### 3.2.2. Global Summary Statistics

**Density (Cost)** Density $D$ is the ratio of the number of existing edges to the total number of possible edges. It serves as a simple estimator of the physical cost of the network in terms of axonal projections:

$$D = \frac{2|E|}{n(n-1)} \tag{3.18}$$

where |E| is the number of edges. Notice that the density is defined only in binary graphs.

**Global Integration: Characteristic Path Length and Global Efficiency** Integration measures the ability of the brain to rapidly combine information from distributed regions.

- **Characteristic Path Length ($L$):** The average of all shortest path lengths between all pairs of nodes:

$$L = \frac{1}{n} \sum_{i \in V} \frac{\sum_{j \neq i \in V} d_{ij}}{n-1} \tag{3.19}$$

- **Global Efficiency ($E_{glob}$):** Inversely related to path length, it measures the capacity for parallel information exchange across the entire network:

$$E_{glob} = \frac{1}{n} \sum_{i \in V} E_{nodal}(i) \tag{3.20}$$

**Global Segregation: Clustering, Transitivity and Modularity** Segregation quantifies the degree of specialized, local processing within densely interconnected groups of regions.

- **Average Clustering Coefficient** (C): The average of the local clustering coefficients across all nodes, representing the overall prevalence of clustered connectivity.
- **Transitivity** (T): A global measure of segregation defined as the ratio of triangles to connected triples in the entire network:

$$T = \frac{3 \times \text{number of triangles}}{\text{number of connected triples}} \tag{3.21}$$

- **Modularity ($Q$):** Given a partition of the set of nodes, $P = C_1, C_2 ... C_q$(communities), the modularity Q quantifies to what extent the intra-/inter-community link densities are anomalous in comparison to chance.

$$Q = \sum_{h=1}^{q} \left[ \frac{1}{2L} \sum_{i,j \in C_h} \left( a_{ij} - \frac{k_i k_j}{2L} \right) \right] = \sum_{h=1}^{q} \left[ \frac{L_h}{L} - \left( \frac{k_h}{2L} \right)^2 \right] \tag{3.22}$$

  where $L$ is the total number of links in the network, $L_h$ is the number of links internal to community $C_h$, and $k_h = \sum_{i \in C_h} k_i$ is the sum of the degrees of all nodes belonging to $C_h$.

- **Number of Communities ($N_c$):** The number of modules $q$ that maximizes modularity, indicating the optimal meso-scale organization of the network.

**Assortativity and the Rich-Club Effect** Assortativity is the correlation between the degrees of connected nodes. A positive assortativity coefficient indicates that high-degree nodes tend to connect to each other, a phenomenon known as the *rich-club effect.* This property provides the network with increased resilience against the failure of individual hubs.

**Network Diameter and Radius** The diameter is the maximum shortest path length between any two nodes in the network ($max(d_{ij})$).

Conversely, the radius is the minimum eccentricity of any node, where eccentricity is the maximum distance from a node to any other node.

**Algebraic Connectivity** The algebraic connectivity is the second smallest eigenvalue of the Laplacian matrix of the network. It is a measure of how well-connected the graph is; a value greater than zero implies the graph is a single connected component. It serves as an indicator of the network's robustness and its ability to synchronize processes across nodes.

**Average Centrality Measures** To summarize the overall influence and distribution of importance within the network, global averages of local metrics are often calculated:

- **Average Betweenness Centrality (BC):** The mean BC across all nodes, indicating the general reliance of the network on "bridge" nodes.
- **Average Eigenvector Centrality (EC):** The mean EC across all nodes, reflecting the global distribution of influence.

### 3.2.3. Network Properties

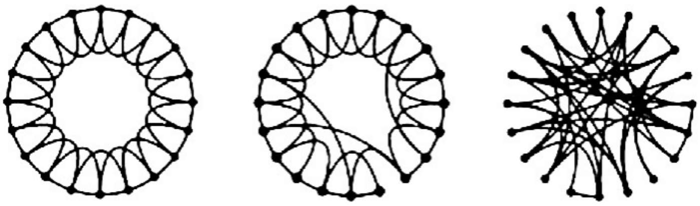

**Figure 3.6:** From left to right, Regular, Small-world and Random networks Source:[38]

Networks may be classified into four broad groups: *regular, random, small-world* or neither of them.
In *regular* networks, also known as lattices, each node has the same degree and is symmetrically connected to its neighbours. In 1998, Watts and Strogatz defined algorithmically random networks, hypothesizing to rewire each node of a regular network with probability 1. The graph on the right of figure 3.6 was obtained. Eventually, they reiterated the same procedure, rewiring the nodes of the regular network with a probability p now between 0 and 1 and coined the term *small-world* to refer to the architecture of the resulting graph. Each network category has its own features. Regular networks are characterized by high local clustering and high average path length. This means that they are locally but not globally efficient. On the other hand, *random* networks have low local clustering and low

average path length. They are globally efficient. Small-world architectures share some features of regular networks and some of random networks. They have high local clustering and low average path length, resulting in being both locally and globally efficient. Studies suggest that a wide variety of natural systems are small-world networks. One of them are healthy structural brain networks.

## 3.3. Classification and Support Vector Methods

The conventional diffusion metrics and the graph-theoretical properties derived from brain connectivity can be employed as features for a statistical classification model. Classification is a supervised learning task whose goal is to predict the class label of an observation based on a set of input variables. Among the several classification algorithms that serve this purpose, Support Vector Machine (SVM) is a relevant one for this thesis.

### 3.3.1. Support Vector Methods

The Support Vector Machine (SVM) is a supervised learning approach for classification that generalizes the concept of linear decision boundaries to handle non-linear relationships. It is based on the Maximal Margin Classifier, which finds the optimal hyperplane to separate two classes with the largest possible margin. In other words, it maximizes the distance between the hyperplane and the two groups. However, real-world data is often not perfectly and linearly separable. Hence, the Support Vector Classifier was developed to be more robust to such common cases[16].

#### The Support Vector Classifier (SVC)

The Support Vector Classifier, also known as the soft margin classifier, allows for some observations to be on the incorrect side of hyperplane or just closer to the boundary that the margin imposes. This flexibility is controlled by introducing slack variables, $\epsilon_1, \dots, \epsilon_n$, which track the relative position of each observation [16].
The optimization problem for an SVC is defined as finding the hyperplane that maximizes the margin $M$ subject to a budget constraint which allows some violations:

$$\max_{\beta_0, \beta_1, \dots, \beta_p, \epsilon_1, \dots, \epsilon_n, M} M \tag{3.23}$$

Subject to:

- **Normalization**: $\sum_{j=1}^{p} \beta_j^2 = 1$.

- **Classification Constraint**: $y_i(\beta_0 + \beta_1 x_{i1} + \cdots + \beta_p x_{ip}) \geq M(1 - \epsilon_i)$.
- **Slack Variables**: $\epsilon_i \geq 0$ and $\sum_{i=1}^{n} \epsilon_i \leq C$.

In this formulation, $C$ is a non-negative tuning parameter that represents the total budget for margin violations.

- If $\epsilon_i = 0$, the $i$-th observation is on the correct side of the margin.
- If $\epsilon_i > 0$, the $i$-th observation has violated the margin.
- If $\epsilon_i > 1$, the $i$-th observation is on the wrong side of the hyperplane.

As the book explains [16], the parameter $C$ controls the bias-variance trade-off. When $C$ is small, the model allows for fewer errors. The margin is narrow: it fits the data closely but may have high variance. Conversely, a large $C$ allows for more violations. The margin is wider: the model is more stable with lower variance but potentially higher bias. It is worth noting that the final boundary depends only on the observations that are close to the margin; these are known as *support vectors*.

### Support Vector Machines and the Kernel Trick

Support Vector Machines (SVM) extend further the Maximal Margin Classifier and the SVC by using non-linear decision boundaries. In this context, *kernels* $K(x_i, x_{i'})$ are functions that quantify the similarity between two observations. When the kernel is linear as in SVC, the similarity is simply the standard inner product. Non-linear kernels are more complex functions, which map the features into a high-dimensional space where a linear separation becomes possible [16].

The most common kernels are:

1. **Linear Kernel**: Equivalent to the Support Vector Classifier.

$$K(x_i, x_{i'}) = \sum_{j=1}^{p} x_{ij} x_{i'j} \tag{3.24}$$

2. **Polynomial Kernel**: Expands the feature space by considering polynomials of degree $d$.

$$K(x_i, x_{i'}) = \left(1 + \sum_{j=1}^{p} x_{ij} x_{i'j}\right)^d \tag{3.25}$$

3. **Radial Basis Function (RBF) Kernel or Gaussian Kernel**: captures local interactions by assigning higher similarity to points that are close in the feature space.

$$K(x_i, x_{i'}) = \exp\left(-\gamma \sum_{j=1}^{p} (x_{ij} - x_{i'j})^2\right) \tag{3.26}$$

### 3.3.2. Model Evaluation

At this point, a question arises: how is the performance of a classification model evaluated? To quantify the effectiveness of a model, several performance metrics are typically used. These metrics are derived from the *confusion matrix.* Following the implementation in Python libraries such as Scikit-learn, the matrix is organized such that the first row and column represent the negative class (controls, label 0), while the second row and column represent the positive class (patients, label 1). For a binary classification task, the confusion matrix is defined as follows:

$$CM = \begin{bmatrix} TN & FN \\ FP & TP \end{bmatrix} \tag{3.27}$$

where TP stands for True Positives, TN for True Negatives, FP for False Positives and FN for False Negatives.
Based on these values, the following metrics are defined:

- **Accuracy**: The proportion of total correct predictions.

$$Accuracy = \frac{TP + TN}{TP + TN + FP + FN} \tag{3.28}$$

- **Precision (Positive Predictive Value)**: The ability of the classifier not to label as positive a sample that is negative.

$$Precision = \frac{TP}{TP + FP} \tag{3.29}$$

- **Recall (Sensitivity)**: The ability of the classifier to find all the positive samples.

$$Recall = \frac{TP}{TP + FN} \tag{3.30}$$

- **Specificity**: The ability of the classifier to correctly identify the negative samples.

$$Specificity = \frac{TN}{TN + FP} \tag{3.31}$$

- **F1-Score**: The harmonic mean of precision and recall, providing a single score that balances both.

$$F1\text{-}Score = 2 \times \frac{Precision \times Recall}{Precision + Recall} = \frac{2TP}{2TP + FP + FN} \tag{3.32}$$

- **ROC-AUC (Area Under the Receiver Operating Characteristic Curve)**: It is the model's ability to discriminate between classes; specifically, it quantifies the probability that the model will rank a randomly chosen positive instance higher than a randomly chosen negative one.

This section concludes the theoretical foundations. Before turning to the empirical analysis from the real-world dataset on temporal lobe epilepsy (TLE), next chapter will provide a literature review. This review details the differences in quantitative DTI measures between TLE patients and healthy controls, as well as the various classification methods and their reported performances.

# 4 Related Works

## 4.1. Pathological Neural Systems in Epilepsy

To contextualize the structural alterations observed in TLE, it is necessary to properly describe the two neural systems most frequently implicated in the pathology: the Limbic System and the Default Mode Network (DMN).

The **Limbic System** represents the primary anatomical substrate for seizure generation and early propagation [8]. It comprises a set of interconnected structures, including the Hippocampus, the Amygdala, the Parahippocampal Gyrus, and the Cingulate Cortex. Beyond its clinical relevance in epilepsy, this system is fundamental for memory formation and emotional processing [24].

Parallel to these focal changes, TLE is nowadays recognized as a network-level disorder affecting the **Default Mode Network (DMN)**. The Default Mode Network (DMN) is a large-scale brain network characterized by higher activity during rest and reduced activity during demanding, goal-directed tasks, as originally described by *Raichle et al.* [29]. Its core regions include the Medial Prefrontal Cortex, involved in self-referential and evaluative processes, and the Posterior Cingulate Cortex/Precuneus, which acts as a central hub for information integration.
Additional regions include the Inferior Parietal Lobule, particularly the Angular Gyrus, and Medial Temporal Lobe structures such as the Hippocampus and Parahippocampal Cortex, which are primarily associated with memory and the integration of information over time. Overall, the DMN supports internally directed cognitive processes, including autobiographical memory, mind-wandering, and future-oriented thinking.

## 4.2. Differences in Quantitative DTI measures between TLE patients and control

As anticipated in section 2.6, we now summarize the current literature about the alterations in structural connectivity that characterize TLE. In particular, the differences in quantitative DTI measures between TLE patients and control. First, we focus on regional microstructural alterations by examining the classical diffusion metrics introduced in Chapter 3; then, we explore findings related to broader network-level disruptions, based on structural connectivity matrices.

### 4.2.1. Evidence from Classical DTI Metrics

Early investigations using Diffusion Tensor Imaging (DTI) established a clear pattern of microstructural damage in TLE patients, primarily characterized by reduced Fractional Anisotropy (FA) and increased Mean Diffusivity (MD). This phenomenon is physiologically consistent with pathological processes: cell necrosis and loss of architectural barriers lead to an increase in the magnitude of water diffusion, which simultaneously becomes more isotropic.
The meta-analysis by *Otte et al.* [26] confirms that TLE pathology is not confined to the temporal gray matter. Their analysis of 13 cross-sectional studies revealed a pooled FA reduction of 0.026 across all white matter and a pooled MD increase of $0.028 \cdot 10^{-3} mm^2/s$. Moreover, while TLE is classified as a focal epilepsy, *Otte et al.* demonstrate that FA reduction and MD increase occur significantly in both ipsilateral and contralateral white matter.

According to *Arfanakis et al.* [2], pathological changes are common in the Hippocampi of patients with hippocampal sclerosis. Beyond the medial temporal structures, significantly ($p<0.05$) reduced mean FA values have been detected in:

- **The External Capsule**: a thin sheet of white matter fibers situated between the Putamen and the Claustrum, which serves as a vital pathway for association fibers connecting the Prefrontal Cortex with other cortical areas.
- **The Posterior Corpus Callosum**: specifically the *splenium*, the thickest part of the major interhemispheric bridge, which facilitates communication between the left and right occipital and posterior temporal lobes.

Building upon these global findings, *Bonilha et al.* [8] focused on the limbic network, which is critical for understanding seizure propagation. Their results highlight a specific vulnerability in the structural backbone of the temporal lobe. Patients exhibit a significant decrease in FA within:

- **The Parahippocampal Gyrus**: a grey matter cortical region surrounding the hippocampus that acts as a primary hub for memory.
- **Temporal Subcortical White Matter**: the underlying wiring connecting the temporal pole with the rest of the neocortex.
- **The Cingulate Cortex**: a key component of the limbic system, involving both the *Anterior Cingulate* (associated with executive functions and emotion) and the *Posterior Cingulate* (a central hub for the Default Mode Network).

While FA was a sensitive indicator of limbic damage, no significant differences in MD were observed between groups. This suggests that in TLE, loss of fiber orientation, captured by decreased FA, may be a better biomarker than the simple increase in water volume, captured by increased MD.

### 4.2.2. Evidence from Network-based Metrics

While classical metrics provide information about microstructural integrity, Graph Theory offers a mathematical framework to evaluate the topological reorganization of the brain in TLE.

#### Limbic Network Reorganization (Bonilha et al. [8])

In 2012, *Bonilha et al.* investigated the structural connectome of 12 patients with unilateral medial temporal lobe epilepsy (MTLE) and hippocampal sclerosis compared to 26 healthy controls. Using 3T DTI data (15 directions, b=1000 $s/mm^2$) and probabilistic tractography, the authors constructed weighted connectivity matrices based on 20 limbic and perilimbic regions from the AAL atlas.

At the whole-network level, MTLE induces a brain structural reorganization that favors local segregation over global integration. *Bonilha et al.* observed:

- **Increased Clustering Coefficient** ($C$): Patients exhibited a significant increase in the mean network clustering coefficient. This increase suggests a higher density of local connections within the limbic circuitry.

- **Preserved Global Efficiency ($E_{glob}$):** The overall efficiency and betweenness centrality of the network were not significantly different between groups.

This combination of high clustering with stable efficiency are compatible with network *regularization* in TLE patients, showing an increased emergence of local connections and the disruption of long-range ones. In short, TLE networks are characterized by increased local re-entrant connections which might not improve the proficiency of information transfer and could instead further induce seizures.

Beyond global topology, the study investigated how TLE affects the individual nodes of the limbic network. A primary finding is that MTLE is associated **decrease in the absolute connectivity** among limbic regions, demonstrated by a significant reduction in the total number of probabilistic streamlines.
However, when examining the network through graph-theoretical metrics, a more complex picture emerges. The results concerning nodal and local analysis are summarized in Table 4.1, reconstructed directly from the findings of [8].

| **Brain Region (Ipsilateral)** | **Degree** | **Efficiency** | **Clustering** | **Betweenness** |
|---|---|---|---|---|
| Hippocampus | Increased | Decreased | Decreased | Increased |
| Thalamus | - | Increased | Increased | - |
| Insula | - | Increased | Increased | Decreased |
| Superior Temporal Region | Increased | Increased | Increased | - |

**Table 4.1:** Summary of nodal graphical property changes in MTLE patients [8].

The data shows an apparent paradox: while the absolute connectivity decreases, the nodal degree (particularly in the Hippocampus and superior temporal regions) actually increases. This suggests a pathological topological reorganization where the loss of major long-distance white matter tracts is accompanied by the birth of numerous weak and re-entrant local connections.
These findings suggest that while the Hippocampus undergoes a degenerative process, the surrounding hubs like the Thalamus and Insula might undergo a reinforcement, potentially playing a key role in maintaining the chronic seizure network.
In terms of absolute connectivity, MTLE is characterized by a widespread reduction in inter-regional connections. Table 4.2 details the altered specific pathways.

| **Connection Pathway** | **Hemisphere/Side** | **Absolute Connectivity** |
|---|---|---|
| Ant. Cingulate — Parahippocampal | Ipsilateral — Contralateral | Decreased |
| Caudate — Inf. Orbitofrontal | Ipsilateral — Bilateral | Decreased |
| Caudate — Insula | Ipsilateral — Contralateral | Decreased |
| Inf. Orbitofrontal — Thalamus | Ipsilateral — Bilateral | Decreased |
| Insula — Fusiform Area | Ipsilateral — Contralateral | Decreased |
| Hippocampus — Parahippocampal | Contralateral — Ipsilateral | Decreased |
| Post. Cingulate — Post. Cingulate | Ipsilateral — Contralateral | Decreased* |
| Hippocampus — Insula | Contralateral — Ipsilateral | Increased |

**Table 4.2:** Changes in absolute inter-regional connectivity in MTLE. (* survived FDR correction).

As shown in Table 4.2, the majority of alterations involve a reduction in probabilistic connections between temporal and extra-temporal regions. Notably, the posterior cingulate connection was the only edge to remain significant after strict FDR correction. This reinforces the key role of the PCC within the Default Mode Network. Conversely, the increased connectivity between the Contralateral Hippocampus and the Insula potentially represents a compensatory rerouting of fibers.

### Whole-Brain Network and DMN Disruption (DeSalvo et al. [11])

Another work that is worth mentioning is the one of *DeSalvo et al.*. Unlike *Bonilha et al.*, they employed a high-resolution whole-brain approach (1000 cortical and 15 subcortical ROIs).
The modularity analysis identified a single medial frontoparietal module encompassing the core nodes of the DMN: the Bilateral Superior Frontal Gyri, Posterior Cingulate Cortices (PCC) and the Precuneus.
While overall modularity did not differ significantly between groups, the global efficiency of the network showed a marked increase in left TLE patients (Table 4.3).

| **Network Metric** | **Variation in left TLE** | **Statistical Significance** |
|---|---|---|
| Global Network Efficiency ($E_{glob}$) | Increased | $P < 0.001$ |
| Overall Network Modularity ($Q$) | No Significant Change | $P > 0.05$ |

**Table 4.3:** Global network property changes in TLE [11].

The principal finding was the specific disruption of the DMN as a structural hub. Connectivity was found to be decreased both within and between modules (Table 4.4). Notice that within-module connectivity was calculated as the within-module $z$-score of degree for each node, which measures how well a node is connected to other nodes in the same module. Conversely, between-module connectivity was measured using the participation coefficient($P_u$), defined as:

$$P_u = 1 - \sum_{m=1}^{N_M} \left( \frac{k_{i,m}}{k_i} \right)^2$$

where $k_{i,m}$ is the number of links of node $i$ to nodes in module $m$, and $k_i$ is the total degree of node $i$.

| **Brain Region** | **Within-Module Connectivity** | **Between-Module Connectivity** |
|---|---|---|
| Posterior Cingulate Cortex (PCC) | Decreased | Decreased |
| Precuneus | Decreased | Decreased |
| Medial Orbitofrontal Cortex | Decreased | Decreased |
| Lateral Frontal Cortex | - | Decreased |
| Inferior Parietal Cortex | - | Decreased |
| Temporal Cortex | - | Decreased |

**Table 4.4:** Regional changes in within- and between-module connectivity [11].

In addition to these connectivity reductions, local efficiency ($E_{loc}$) was found to be significantly increased ($P < 0.01$) in several cortical areas. These regions include the Bilateral Precuneus and Posterior Cingulate Cortices, as well as the Lateral Frontal, Temporal, Insular and Occipital Cortices.

This paradoxical increase in local efficiency alongside **decreased long-range DMN connectivity** suggests that the DMN loses its role as a structural hub in patients with TLE. Similarly to [8], *DeSalvo et al.* hypothesized that the loss of microstructural white matter integrity reduces long-range connectivity but promotes local network reorganization. In particular, thanks to neuroplasticity, new short-range connections form, potentially facilitating the propagation of seizures across the cortex.

### Whole-Brain Network Disruption (Liu et al. [22])

While *Bonilha et Al.* focused on the Limbic System and *DeSalvo et al.* on the DMN and cortical regions, *Liu et al.* [22] provided a comprehensive evaluation of the whole-brain network specifically in patients with left mesial temporal lobe epilepsy (mTLE). This study is particularly relevant to us as it utilizes the AAL atlas to define nodes and employs a deterministic streamline tractography approach, choses we also made in our empirical analysis.

To define the network nodes, the brain was segmented into 78 anatomical regions (39 per hemisphere) using the AAL atlas. Connectivity was reconstructed using a deterministic streamline-tracking method, with threshold parameters defined by a Fractional Anisotropy (FA) >0.2 and a curvature angle of less than 45°.

First, both controls and mTLE patients demonstrated small-world properties. However, the topological organization was significantly different between patients and controls, as summarized in Table 4.5.

| **Global Metric** | **Variation in left mTLE** | **Statistical Significance** |
|---|---|---|
| Total Number of Edges ($K$) | Decreased | $P < 0.05$ |
| Characteristic Path Length ($L$) | Increased | $P < 0.05$ |
| Global Efficiency ($E_{glob}$) | Decreased | $P < 0.05$ |

**Table 4.5:** Global white matter network property changes in left mTLE [22].

The increase in average path length combined with the **decrease in global efficiency** suggests the degradation of long-range connections. This finding has been interpreted by *Liu et al.* as a shift toward a more regular configuration of the network as well. Unlike *Bonilha et al.* [8], who reported stable global efficiency in a network limited to the limbic system and *DeSalvo et al.*, who found quite paradoxically an increase in global efficiency (probably explained by the different brain parcellation), this whole-brain analysis reveals a clear deterioration of the network's capacity to transfer information efficiently.

Compared to controls, patients with left mTLE showed significantly **reduced local efficiency** in 17 cortical regions of the left temporal, bilateral frontal, and bilateral parietal lobes. Four frontal regions including the right paracentral lobule and supplemental motor area, and the left inferior frontal opercular gyrus and precentral gyrus; one temporal region, that is, the left superior temporal gyrus; and one parietal region, that is, the right postcentral gyrus.

A crucial finding concerns the **reorganization of hubs**: in healthy controls, the left precuneus was identified as a primary heteromodal hub, essential for visuospatial integration and episodic memory. In mTLE patients, the precuneus loses its hub status, likely due to reduced connectivity with the hippocampus and structural abnormalities in the cingulum bundle.

Another study which confirms the increase in path length and the hub reorganization is the one of *Bernhardt et al.* [4]. However, Bernhardt reported an increase in clustering, Liu found no significant changes in this metric. This discrepancy once again highlights how different imaging modalities (T1-morphometry vs. DTI-tractography in this example) and different network construction methods capture distinct and complementary aspects of TLE.

Finally, an important remark must be made about the side of TLE. In this section, we compared studies focused on left TLE with others whose unhealthy patients could have left or right or bilateral TLE. This approach aligns with our general analysis where we decided to do not separate them.

## 4.3. Classification of TLE using Quantitative DTI measures

We now move on to presenting the literature on the classification of TLE using both conventional diffusion and structural network metrics. However, before we begin, a remark must be made: only one of the papers synthesized below is about TLE; the other two are on focal epilepsy (TLE is the most common form of focal epilepsy) and on juvenile myoclonic epilepsy respectively. We chose to include them as they are relevant to our classification task and employ similar metrics as features.
Unfortunately, as it will be apparent in the next chapters, to the best of our knowledge, there is no paper in the literature that is similar enough in terms of data used, methodologies and goals selected to be perfectly comparable to our findings.

The first study we consider is the work by *Kamiya et al. (2016)* [18]. This study specifically employed DTI-based structural connectomes combined with a machine learning approach to classify the side of **TLE**. In other words, in this work, Right and Left TLE are analyzed separately.
The dataset used consists of 58 participants: 44 patients with TLE (29 left-sided and 15 right-sided) and 14 age-matched healthy controls. The neuroimaging protocol included 3D T1-weighted imaging and DTI with 13 gradient directions. For the connectivity analysis, the Desikan-Killiany Atlas was used to parcellate the brain into 83 regions of interest (ROIs). Whole-brain deterministic tractography was performed and a weighted connectivity adjacency matrix was generated for each subject.
To capture the topological properties of the brain networks, four key graph theoretical metrics were calculated for each node: Nodal Degree, Clustering Coefficient, Local Efficiency, and Betweenness Centrality. Given the high dimensionality of the feature set (332 features per subject) relative to the sample size, the authors used the Dantzig selector, a sparse linear regression technique, to reduce the feature space.
The classification was performed using a Support Vector Machine (SVM) with a Radial

Basis Function (RBF) kernel. The study involved three distinct classification tasks: RTLE vs. Controls, LTLE vs. Controls, and LTLE vs. RTLE. The performance of the classifier was not validated on an external test set, but using a Leave-One-Out Cross-Validation (LOOCV) strategy.

The results demonstrated that the SVM could successfully distinguish between groups with high accuracy. As for feature importance, the most discriminating features were predominantly located in the Limbic System and the Default Mode Network (DMN), particularly involving the hippocampi and the posterior cingulate gyrus. Performance metrics are summarized in Table 4.6.

| **Classification Task** | **Accuracy Range** | **AUC Range** |
|---|---|---|
| RTLE vs. Controls | 75.9% – 89.7% | 0.79 – 0.97 |
| LTLE vs. Controls | 74.4% – 86.0% | 0.84 – 0.91 |
| LTLE vs. RTLE | 72.7% – 86.4% | 0.82 – 0.91 |

**Table 4.6:** Classification results from Kamiya et al. (2016).

On a final note, although the primary goal of this study was classification, the authors also analyzed the significant differences in terms of network metrics. They did not observe the paradoxical increase in clustering coefficient or local efficiency previously reported by *Bonilha et al.* [8] and *DeSalvo et al.* [11].

The second study we consider is by *Lee et al. (2020)* [21]. This study focuses on focal epilepsy more broadly and employs a relevant methodological framework based on conventional diffusion metrics and graph theory to classify **focal epilepsy** patients.

This study involved a significantly larger cohort of 556 participants: 456 patients with focal epilepsy and 100 age- and sex-matched healthy controls. Hence, the dataset is unbalanced. Imaging was performed using a 3.0T scanner with 32 diffusion gradient directions. The brain was parcellated into regions defined by the Automated Anatomical Labeling (AAL) template. Data processing was performed using DSI Studio, where the raw diffusion-weighted images (DWI) were reconstructed using Q-Space Diffeomorphic Reconstruction (QSDR). This method was preferred over the conventional DTI model as it handles crossing fibers and spatial normalization more effectively. We will provide an in-depth discussion of QSDR in the next chapter, as it is the mathematical model used to process our own raw DWI data and estimate diffusion orientations and intensities.

Then, for each subject, conventional diffusion measures were extracted and connectivity matrices were generated. As a matter of fact, the researchers used two distinct sets of features: conventional DTI measures, such as Fractional Anisotropy (FA), Mean Diffusivity (MD), Axial Diffusivity (AD), and Radial Diffusivity (RD), and structural connectomic profiles, including mean clustering coefficient, transitivity, characteristic path length, small-worldness, global/local efficiency, diameter, radius, and assortativity. For feature selection, the authors performed Student's $t$-tests to keep only the variables with significant differences between groups ($p < 0.05$). All features were standardized using Z-scores.

The classification was implemented once again using a Support Vector Machine (SVM); however, in this study, a linear kernel was employed. The model parameters were tuned using 10-fold cross-validation on the training set, and then performance was evaluated on an unbiased test set, accounting for 20% of the data.

| **Task** | **Features** | **Acc** | **Sens** | **Spec** | **PPV** | **NPV** | **AUC** |
|---|---|---|---|---|---|---|---|
| Epilepsy vs. HC | DTI only | 76.5% | 85.7% | 35.0% | 85.7% | 35.0% | 0.604 |
| Epilepsy vs. HC | DTI + Conn. | 82.8% | 90.1% | 50.0% | 89.1% | 52.6% | 0.701 |

**Table 4.7:** Classification performance for focal epilepsy vs. healthy controls (Lee et al., 2021). Acc: Accuracy; Sens: Sensitivity; Spec: Specificity; PPV: Positive Predictive Value; NPV: Negative Predictive Value.

The study found that combining conventional DTI measures with structural connectomic profiles improved classification performance compared to using DTI measures alone. However, a limitation is that the primary scoring metric reported is Accuracy, even though the dataset is unbalanced. This may overestimate the performance: indeed, we observe that metrics such as Specificity and AUC are much lower.

The third study we consider is by *Lee et al. (2021)* [20]. This work is included as it employs the same methodological pipeline as the previous study on focal epilepsy: both conventional DTI and network metrics are used. Nevertheless, it focuses on **Juvenile Myoclonic Epilepsy (JME)**.

The study included a total of 113 participants: 55 patients with JME and 58 age- and sex-matched healthy controls. In this case, the dataset is balanced. Similarly to the previous paper, the imaging was performed with a 3.0T scanner using 32 diffusion gradient directions. The AAL template was used for brain parcellation. Data processing followed the same pipeline using DSI Studio, with raw DWI data reconstructed via Q-Space Diffeomorphic Reconstruction (QSDR).

The researchers extracted both global and regional features. These included conventional DTI measures (FA, MD, AD, and RD values) and structural connectomic profiles, such as global network metrics (clustering coefficient, efficiency, path length, etc.) and regional betweenness centrality for the AAL-based ROIs. Feature selection used Student's $t$-tests

to keep variables with significant differences between groups ($p < 0.05$). All variables were standardized using Z-scores before classification.
The classification task consisted of separating JME patients from healthy controls, and the model used was a Support Vector Machine (SVM).

| **Task** | **Features** | **Acc** | **Sens** | **Spec** | **PPV** | **NPV** | **AUC** |
|---|---|---|---|---|---|---|---|
| JME vs. HC | DTI only | 68.1% | 63.6% | 72.7% | 70.0% | 66.6% | 0.682 |
| JME vs. HC | Connectomics | 72.7% | 54.5% | 90.9% | 85.7% | 66.6% | 0.727 |
| JME vs. HC | DTI + Conn. | 81.8% | 81.8% | 81.8% | 81.8% | 81.8% | 0.818 |

**Table 4.8:** Classification performance for JME vs. healthy controls (Lee et al., 2021). Acc: Accuracy; Sens: Sensitivity; Spec: Specificity; PPV: Positive Predictive Value; NPV: Negative Predictive Value.

The results confirmed that the combination of microstructural diffusion measures and macrostructural network profiles determines the best predictive power. While global network measures did not show significant differences alone, regional alterations were discriminant for classification. Particularly in the Frontal Lobe, FA was consistently lower, and the betweenness centrality of limbic structures was altered. In particular, increases were observed in the left Amygdala, right Posterior Cingulum, left Superior Orbitofrontal Gyrus, right Heschl's Gyrus, left Hippocampus, left Olfactory Cortex and left Inferior Parietal Gyrus, whereas a decrease was found in the left Middle Temporal Gyrus.
Notice that this last study does not classify temporal lobe epilepsy so results can not be directly compared to our own analysis.

Finally, another relevant study is the work by *Cantor-Rivera et al. (2015)* [10], which combines DTI with T1 and T2 quantitative mapping to classify **TLE** via SVM. Although it incorporates relaxometry measures which we do not have in our dataset, it introduces few filtering-based feature selection pipelines, which inspired our own explained in Chapter 6. The authors performed 4 different pipelines: each one has "one of two possible feature selection methods (correlation-based or ANOVA-based); the option or not of performing dimensionality reduction with PCA" [10].
Notice that the best performances in this study were achieved using only the T1 images with an accuracy of 88.9% (sensitivity: 82.4%, recall: 94.7%), whereas classic DTI metrics reached as high as 80.6% (sensitivity: 64.7%, recall: 94.7%). Moreover, these results were obtained on the Leave-One-Out (LOO) Cross-Validation, not on an independent test set.
We are now ready to introduce the dataset, detail the preprocessing steps and the data analysis methodology.

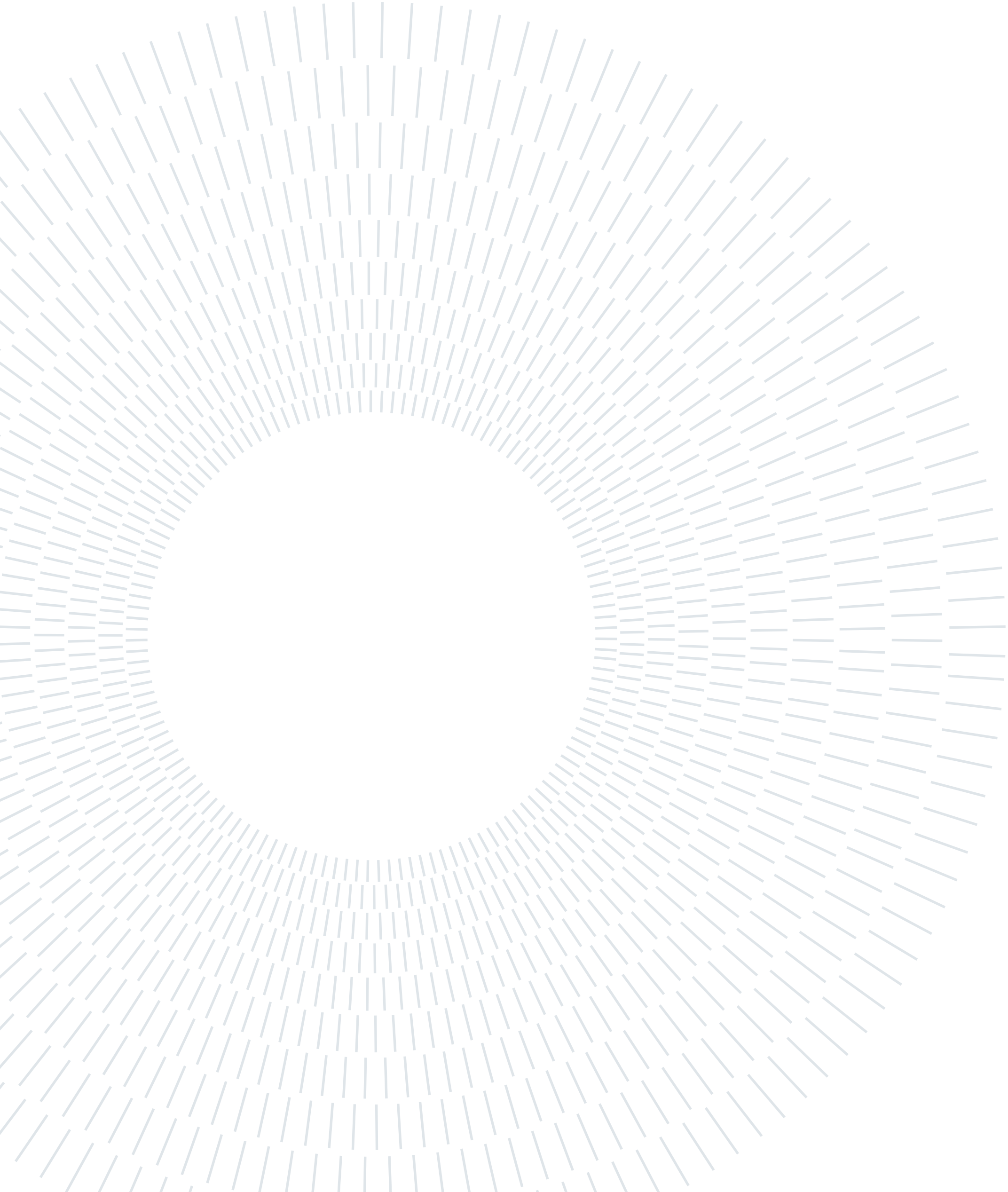

# 5 | Materials and Methods

## 5.1. Dataset and Preprocessing

The dataset used for this thesis belongs to the *Epilepsy Connectome Project (ECP)* (https://www.humanconnectome.org/study/epilepsy-connectome-project), which aims to use imaging tools for quantitatively characterizing the structural and functional brain connectivity to aid in treating refractory temporal lobe epilepsy (TLE). The data collected include demographic data, medical and seizure history, clinical/behavioral assessments, with a focus on memory and language and multi-modal imaging data for 340 participants. Specifically, the cohort includes subjects aged 18 to 50 years-old, divided between 140 healthy controls and 200 participants with idiopathic TLE.

Regarding imaging, MR data collection was conducted on a GE MR750 3T scanner and the modalities include Diffusion-Weighted Imaging (DWI) for structural connectivity, Resting-State and Task-Based fMRI for functional network analysis and Magnetoencephalography. Since the goal of this thesis is to study structural brain connectivity, we will exclusively utilize DWI data and the clinical label (healthy vs TLE). Our analysis does not start from raw DWI data but from a partially preprocessed dataset provided by Fang-Cheng Yeh and downloaded via *DSI Studio* (http://dsi-studio.labsolver.org). This dataset includes only 181 subjects: 105 TLE patients and 76 controls. Below are the details regarding the diffusion parameters and the preprocessing steps applied to ECP data and retrieved from *DSI Studio*.

### 5.1.1. Diffusion Parameters and Preprocessing

The diffusion analysis followed a multi-step pipeline. Data were acquired using a multishell diffusion scheme with b-values of 1000 and 2000 s/mm$^2$. The number of diffusion sampling directions were 75 and 75, respectively. The in-plane resolution was 0.863 mm with a slice thickness of 1.50 mm.

To correct for geometric distortions, the pipeline utilized a pair of $b_0$ scans with opposite phase-encoding directions: Posterior-Anterior (PA) and Anterior-Posterior (AP). 19 PA encoding and 19 AP encoding b0 images were used to estimate susceptibility using FSL topup. The eddy current distortions of 169 DWI and 169 opposite phase DWI were corrected using FSL eddy.

Then the images were resampled to 1.00 mm isotropic resolution and the bias field was corrected using b0 image. The diffusion data were reconstructed in the MNI space using **Q-Space Diffeomorphic Reconstruction (QSDR)** [40] to obtain the spin distribution function [41] (see BOX 3). For the reconstruction, a diffusion sampling length ratio of 1.25 was used, ensuring that the output resolution in diffeomorphic reconstruction was 1 mm isotropic. Additionally, the restricted diffusion was quantified using Restricted Diffusion Imaging [42]. The tensor metrics were calculated using DWI with b-value lower than 1750 s/mm$^2$.

While this thesis does not delve into the technical details of every parameters reported, for the sake of completeness, the following box is an overview about Q-Space Diffeomorphic Reconstruction (QSDR) to better understand the context.

### BOX 3: Q-Space Diffeomorphic Reconstruction (QSDR)

Once diffusion data were preprocessed and resampled to a 1.00 mm isotropic resolution, structural reconstruction was performed in the MNI space using Q-Space Diffeomorphic Reconstruction (QSDR) [40]. But what is this method? Q-Space Diffeomorphic Reconstruction (QSDR) was developed by Yeh in 2011 to overcome one of the main limitations of traditional Diffusion Tensor Imaging (DTI): its inability to resolve crossing fibers. Instead of computing for each voxel the principal direction of water diffusion, QSDR reconstructs the so called Spin Distribution Function (SDF) [41]. SDF is indeed a distribution function whose peaks identify the directions of multiple fiber populations within a single voxel. The other essential feature of QSDR is that it directly reconstructs such SDF in the MNI (ICBM-152) standard space. This is achieved through a nonlinear (diffeomorphic) warping process that maintains the conservation of diffusion spins through Jacobian transformation, ensuring that the density of the fiber tracts is preserved during normalization. This implies that anatomical brain parcellation with anatomical atlases does not require any further registration.

One of the main additional classical metric which can be extracted for each voxel with QSDR is Quantitative Anisotropy (QA). Unlike Fractional Anisotropy (FA) which measures the variance of diffusion, QA quantifies the density of spins diffusing along a specific direction. Other characteristic metrics are the Restricted

Diffusion Index (RDI) and Quantitative Isotropy Reconstruction (QIR). The first measures how much water is trapped in tiny spaces. High RDI means that the tissue is very crowded with cells. The second quantifies water that moves freely in all directions. High QIR is an indicator of free fluid between cells.

### 5.1.2. Participants and Demographics

To have a better understanding of our data, we will give an overview of the demographics of the subjects included in the study. However, apart from subjects' labels, this data will not be used in our analysis.

From the original ECP cohort, a subset of 181 subjects was selected for this thesis based on data availability on *DSI Studio*. The final cohort consists of 105 patients with temporal lobe epilepsy (TLE) and 76 healthy controls (HC).

Regarding the demographic distribution, the HC group had a mean age of 35.21±10.81 years, while the TLE group was slightly older with a mean of 39.08±11.87 years. Although a t-test revealed a statistically significant difference in age between the two groups ($p=0.026$), both cohorts fall within the same biological life stage. In terms of sex distribution, the HC group (32M/43F) and the TLE group (38M/67F) showed no significant differences ($\chi^2$ test, $p=0.34$), indicating a well-balanced sample for this variable.

Moreover, additional clinical statistics to add about the TLE group. Within the patient cohort, only 26 out of 105 patients had Mesial Temporal Sclerosis (MTS). Regarding seizure lateralization, the majority of ill subjects (63) suffered from left TLE; 20 of them had right TLE; 8 were diagnosed with bilateral TLE and 13 were uncertain. This split, in particular the presence of several either bilateral or uncertain cases, and the limited size of the dataset justify why in this thesis we chose to classify TLE vs controls rather than separating left and right patients.

## 5.2. Methods

### 5.2.1. Extraction of Quantitative measures and Tractography

The files which we downloaded from DSI studio are *.qsdr.fz* files. They contain the voxel-wise Spin Distribution Functions (SDF), Quantitative Anisotropy (QA), Restricted Diffusion Index (RDI) and Quantitative Isotropy Reconstruction (QIR) maps and standard DTI metrics, such as MD, FA, RD, AD.

As quantitative measures for our empirical analysis, we first extracted classical diffusion metrics. However, to transition from voxel-wise data to regional measures, we computed the mean and standard deviation of these scalars within each Region of Interest (ROI). These ROIs were defined using the Automated Anatomical Labeling 2 (AAL2). While the mean of the diffusion metrics measures general tissue characteristics, the standard deviation was included to capture microstructural heterogeneity within the regions. To investigate further structural connectivity, we applied a deterministic tractography algorithm (Method 0 in DSI Studio) with a seeding density of 1,000,000 streamlines per subject. By mapping these streamlines onto anatomical parcellations, we constructed weighted connectivity matrices. Each entry of those represents the streamline count between two brain regions (see Appendix B for the implementation on DSI Studio).

Brain segmentation was performed using the established Anatomical Automatic Labeling (AAL2) atlas. Given that TLE involves crucial interactions between cortical and subcortical structures, such as the Hippocampus and the Thalamus, AAL2 was selected as our primary reference parcellation. It was preferred over the purely cortical high-resolution Human Connectome Project Multi-Modal Parcellation (HCP-MMP) atlas after initial explorative attempts showed the latter's limitations in capturing these essential subcortical dynamics.
AAL2 is an anatomical atlas based on 120 macro-regions [31]. We have reported below the brain parcellation for subject EC2113, created with DSI Studio.

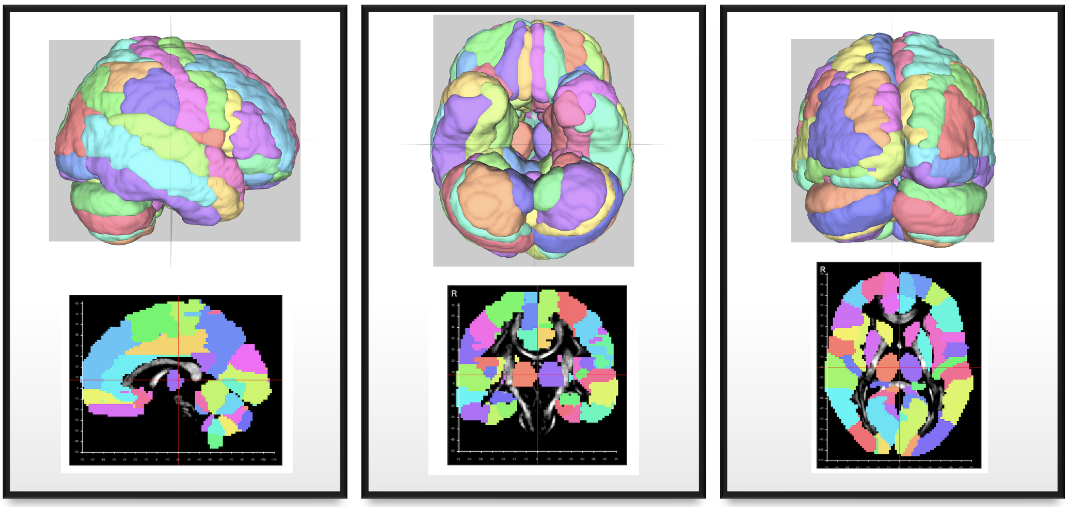

**Figure 5.1:** From left to right, Sagital, Axial and Coronal views of AAL2 for subject EC2113. Created with DSI Studio.

We conclude this section showing the connectivity matrix and the corresponding graph for subject EC2132:

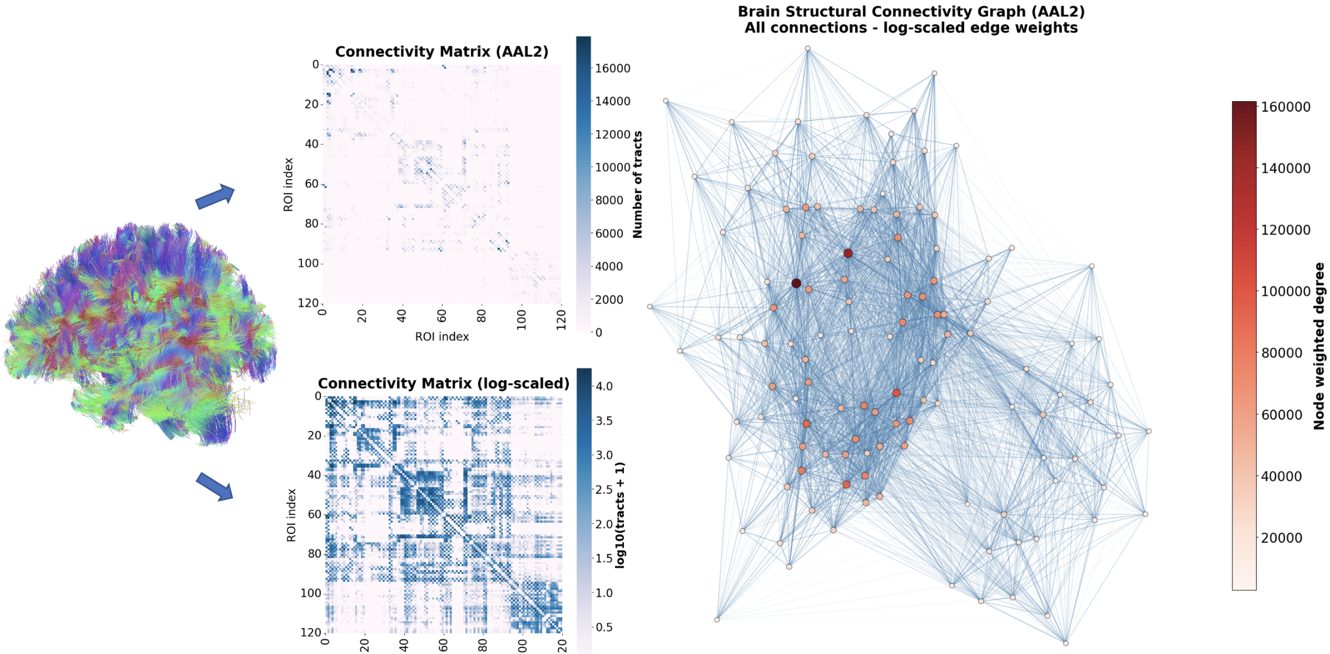

**Figure 5.2:** From Tractography to Brain Graph. The weighted connectivity matrix for subject EC2132 was generated using the AAL2 atlas parcellation, with the resulting network visualized via the Fruchterman-Reingold (FR) force-directed algorithm (see BOX 4). Visualization created with DSI Studio and Python.

**BOX 4**: The Fruchterman-Reingold (FR) Algorithm

The Fruchterman-Reingold algorithm [14] is a force-directed placement algorithm aimed at interpreting the network as a physical system of charged particles and springs. The algorithm treats vertices as *atomic particles or celestial bodies, exerting attractive and repulsive forces on one another* [14]. The attractive and the repulsive forces, inspired by Hooke's law, are constructed as follows:

$$f_a(d) = \frac{d^2}{k} \tag{5.1}$$

$$f_r(d) = \frac{k^2}{d} \tag{5.2}$$

where $f_a$ is the attractive force between neighbor nodes $i$ and $j$, $f_r$ is the repulsive force between nodes $i$ and $j$, $d$ is the Euclidean distance between the nodes, and $k$ is the optimal distance between $i$ and $j$.

According to the model specifications, $k$ is computed as:

$$k = C\sqrt{\frac{\text{Area}}{N}} \tag{5.3}$$

where $C$ is an experimental constant, $Area$ is the area available to draw the graph, and $N$ is the number of nodes in the network.

The goal of the algorithm is to minimize the sum of all attractive and repulsive forces by repositioning nodes in an iterative process in order to reach a potential equilibrium state in which all forces balance. The FR algorithm operates as follows. At every iteration, three steps are performed:

- First: For each pair of neighbor nodes, the attractive force is computed.
- Second: For each pair of vertices, the repulsive force is computed.
- Third: Each node is repositioned.

Specifically, node $i$ is moved by a displacement $d_i$ in the direction of $F_i$, which is the net force vector acting on vertex $v$. The displacement is limited by a parameter $T$, called "temperature": it is a coefficient, initially set between 0 and 1, that gradually decays at each iteration towards 0.

Given that a perfect equilibrium state is unlikely to be achieved, the cooling schedule of $T$ is necessary to terminate the algorithm by gradually stopping the movements of the nodes. Other termination mechanisms include stopping the algorithm after a fixed number of iterations or when the temperature $T < \epsilon$, where $\epsilon$ is a predefined precision threshold.

### 5.2.2. Graph Construction and Network Metrics

Once the connectivity matrices were constructed for each subject, we modeled the brain as a mathematical graph $G = (V, E)$, where V is the set of nodes and E is the set of edges. To capture different aspects of the brain's topological organization, we built in Python two types of networks:

- **Weighted Graphs**: In this model, the edge weight $w_{ij}$ represents the streamline count between nodes i and j. This provides a measure of the strength of the structural connection.
- **Binary Graphs**: These are obtained by thresholding the connectivity matrices. An edge $e_{ij}$ exists ($e = 1$) if the streamline count is greater than zero, and $e = 0$ otherwise. This model focuses exclusively on the network's topological existence of connections.

$$e_{ij} = \begin{cases} 1 & \text{if } w_{ij} > 0 \\ 0 & \text{if } w_{ij} = 0 \end{cases} \tag{5.4}$$

Using the Python library NetworkX, we extracted a comprehensive set of metrics categorized into global and nodal levels:

- *Weighted global metrics*: number of nodes, number of edges, average strength, total strength, standard deviation of strength, average clustering coefficient, global efficiency, average shortest path, average degree centrality, average betweenness centrality, average closeness centrality, average eigenvector centrality, algebraic connectivity, modularity, number of communities, and small-worldness.
- *Binary global metrics*: density, average clustering coefficient, transitivity, average shortest path, diameter, radius, average degree centrality, average betweenness centrality, average closeness centrality, average eigenvector centrality, modularity, number of communities, small-worldness, and number of connected components.
- *Nodal metrics*: degree, strength, binary clustering, weighted clustering, betweenness, closeness, weighted local efficiency, binary local efficiency, eigenvector.

Since certain graph properties are mathematically sensitive to the number of nodes or require a minimum topological complexity to be meaningful, we implemented specific size thresholds. In cases where a graph (or a subgraph) has only few nodes, only the metrics compatible with its dimension were computed.

- **Minimum 3 nodes**: required to compute average clustering and transitivity.

- **Minimum 5 nodes**: required for centrality indices and average shortest path.
- **Minimum 10 nodes**: required for diameter, radius, eigenvector centrality, and small-worldness.

For weighted measures requiring distance calculations, the distance $d_{ij}$ between two nodes $i$ and $j$ has been defined as the sum of the inverse of the weights of the edges along the shortest path.

A final remark on how the small-worldness coefficient was computed. A network exhibits small-world properties if it possesses high local clustering and a short average distance between nodes. We computed it as:

$$\sigma = \frac{C/C_{rand}}{L/L_{rand}} \tag{5.5}$$

where C and L represent respectively the average clustering coefficient and the characteristic path length of the network, while $C_{rand}$ and $L_{rand}$ are the values obtained from a random graph with the same number of nodes and edges.

### 5.2.3. Statistical Analysis: Significant Differences

To examine the differences in conventional DTI and network-based metrics between groups, we perform a statistical analysis in Python employing the non-parametric Mann-Whitney U test, since the connectivity data does not follow a normal distribution.

Since multiple contemporaneous tests are performed, we correct the p-values using the False Discovery Rate (FDR). It is worth noting that we are not exclusively interested in whether p-values fall below the standard $\alpha$=0.05 threshold; identifying statistical trends is equally important. This perspective allows us to better understand the structural dynamics of TLE.

### 5.2.4. Classification Pipeline

Lastly, we detail the classification pipeline designed in Python to distinguish TLE patients from healthy controls using structural connectivity data. Its major steps include:

1. Feature Extraction
2. Feature Selection (Mann-Whitney and Correlation)
3. Classification Model Training
4. Feature Importance

Following the feature extraction process, we built a dataset containing the metrics and respective labels for all 181 subjects. In case of any missing values, if they were less than 5%, we handled them by filling them in with the median; otherwise, we removed the corresponding variable. We chose this approach because our dataset is relatively small and we did not want to lose any subject.

Since the initial space of diffusion and network-based metrics consisted of hundreds or even thousands of variables, to properly train a machine learning model on a reasonable number of features, we introduced two feature selection steps involving a *Mann-Whitney selector* and a *correlation selector*. Notice that feature selection was not conducted on the entire dataset, but only on the training set (85% of the data) in order to avoid any data leakage.

The first filter performs a Mann-Whitney U test on each feature and keeps the ones whose p-value (without any correction for multiple tests) is below a certain threshold $\alpha$. It is worth noting that we are not necessarily looking for features whose difference across groups is inherently statistically significant; rather, we want to eliminate variables that are not related to temporal lobe epilepsy and retain those that, alone or in combination with others, may define epilepsy dynamics in terms of structural brain connectivity.

The second filter, after computing the Spearman correlation for each pair of features, eliminates one of the two if a certain threshold $\beta$ is reached, specifically the feature that correlates less with the label. We chose Spearman correlation instead of Pearson because it is more robust to outliers and does not assume a linear relationship between variables. This additional selector is crucial in such a task as both conventional diffusion and network-based connectivity metrics are highly correlated between each other. Selectors' thresholds were selected conducting a 5-fold cross-validation procedure (5.3).

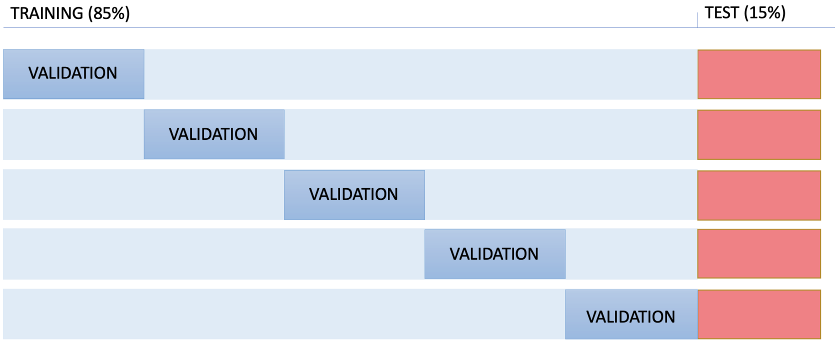

**Figure 5.3:** Partitioning of the dataset in the machine learning analysis. After dividing the dataset into Training and Test sets, the Training set is further divided in 5 folds for Cross-Validation.

Additionally, data were scaled using a *RobustScaler* to minimize the influence of outliers. While several classification models were initially explored, including Logistic Regression, Random Forest and Boosting, this work focuses on Support Vector Machines (SVM). This decision was motivated by the superior performance observed in preliminary tests and is consistent with existing literature. Model's parameters were tuned using the Python *GridSearchCV* tool. We chose to adopt as scoring metric the Balanced Accuracy, to maintain a neutral preference regarding which group is prioritized during classification. Additional metrics including the Accuracy, the Precision, the Recall, the Specificity and F1-Score and the ROC-AUC were utilized to evaluate the performance of the classification models.

If we had used, for example, the F1 score, final performances would have looked more optimistic since our dataset is unbalanced toward epileptic patients. This implies that the model might learn to predict epilepsy more effectively than to predict a control.

Few additional attempts were also made to further filter the feature space by removing the least relevant features for prediction. Lastly, a feature importance analysis was conducted to better understand and interpret the final model. This section concludes this chapter.

# 6 | Significant Differences across Groups: a Multi-Scale and Multi-Domain Approach

We are now ready to investigate the significant differences in structural brain connectivity between TLE patients and healthy controls. To simultaneously examine the local and global organization of the brain network, the connectivity analysis was conducted using a **hierarchical framework**. This approach allows for the characterization of TLE-induced alterations across different levels of cerebral organization, ranging from local regions to large-scale anatomical and functional systems.

This framework is inspired by the body of literature on TLE presented in the previous chapters, which identifies temporal lobe epilepsy as a complex network disease. Consequently, focusing on isolated brain regions is often insufficient to capture the full extent of the pathology. Throughout the years, specific regions and large-scale networks have been shown to play a crucial role in seizure generation and propagation. This multi-scale approach aims to leverage and integrate the findings reported by various authors who utilized different brain parcellations or focused on specific anatomical subsystems.

In the following sections, we first define the hierarchical levels for AAL2 brain parcellation and then discuss the significant group differences identified at each stage. For every level, both conventional diffusion metrics and network-based measures are computed.

## 6.1. Hierarchical Levels

### Level 1: ROI-based Global Graph

The first level of analysis models structural connectivity as a graph based on the AAL2 atlas. In particular, the network's nodes are the 120 Regions of Interest (ROIs) from the AAL2 atlas. The metrics extracted are global and nodal graph theory metrics (e.g. nodal strength and betweenness centrality) and global and regional mean and standard deviation values of diffusion scalars (e.g. QA and MD). This level allows for the characterization of microstructures in the whole-brain, but this perspective on the brain, a network with 120 nodes, risks to capture too much noise.

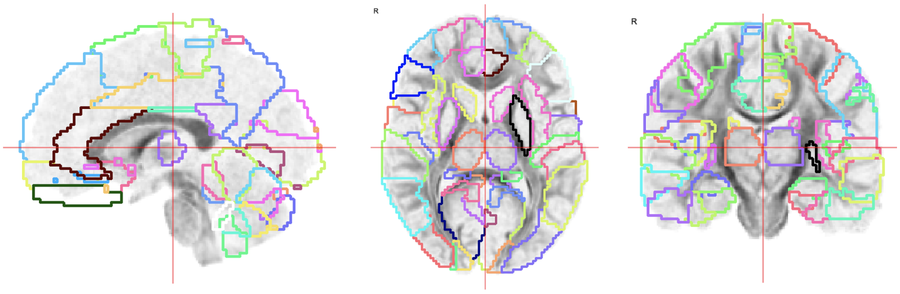

**Figure 6.1:** Regions of Interest (ROIs) of AAL2 atlas. From left to right, sagittal, axial and coronal views for subject EC2132.

### Level 2: Anatomical Macro-Regions

To assess the connectivity of broader anatomical systems, AAL2 ROIs were grouped into macro-regions based on neuroanatomical literature (Table 6.1 and Figure 6.2). Notice that AAL2 atlas provides the anatomical macro-region corresponding to each ROI. For each macro-region, a subgraph was constructed containing exclusively the nodes and the edges internal to that region. Integration and segregation global and nodal indices were calculated specifically on these subgraphs. This allows us to understand if the internal connectivity of macro-anatomical regions such as the Temporal Lobe is degraded in TLE patients compared to controls. Additionally, we evaluated the interactions between anatomical regions building a *super-graph*, whose nodes are the anatomical regions. This level is crucial for understanding how focal alterations might propagate in macro-regions.

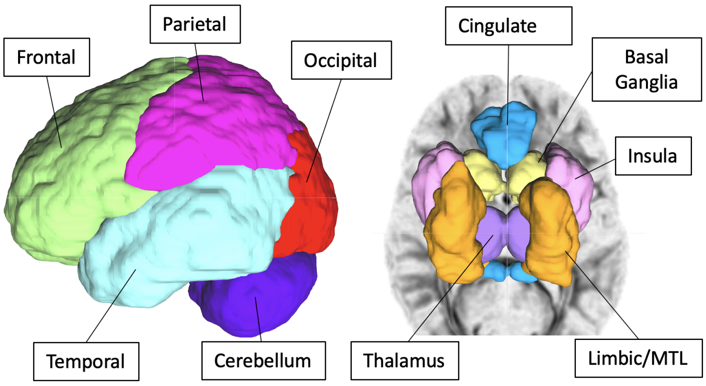

**Figure 6.2:** Anatomical Macro-Regions. On the left, cortical regions, while on the right subcortical ones for subject EC2132.

**Table 6.1:** Macro-anatomical subdivision of the brain regions based on the 120-ROI AAL2 atlas mapping.

| Macro-Region | Included AAL2 Anatomical Areas | N. ROI |
|---|---|---|
| Frontal | Precentral, Frontal Sup/Mid/Inf, SMA, Rectus, OFC, Olfactory | 32 |
| Insula | Insula (L/R) | 2 |
| Cingulate | Anterior, Middle, and Posterior Cingulate gyri | 6 |
| Limbic_MTL | Medial Temporal Lobe: Hippocampus, Parahippocampal, Amygdala | 6 |
| Temporal | Heschl's gyrus, Temporal Sup/Mid/Inf, Temporal Pole | 12 |
| Parietal | Postcentral, Parietal Sup/Inf, SupraMarginal, Angular, Precuneus | 14 |
| Occipital | Calcarine, Cuneus, Lingual, Occipital Sup/Mid/Inf, Fusiform | 14 |
| Basal_Ganglia | Caudate, Putamen, and Pallidum | 6 |
| Thalamus | Thalamus (L/R) | 2 |
| Cerebellum | Cerebellar Hemispheres (Crus I-II, 3-10) and Vermis (1-10) | 26 |
| **Total** | | **120** |

### Level 3: Functional Networks

Finally, a functional level was added. AAL2 ROIs were reorganized according to established functional networks, specifically the *Default Mode Network (DMN)* [29] and the *Limbic System* [24]. Here, unlike the anatomical where each ROI is mapped to a region, the functional level focuses exclusively on the specific subset of ROIs constituting these two networks, as detailed in Tables 6.2 and 6.3. Therefore, also for this level, a super-graph was created with few super-nodes. The mean and the standard deviation of conventional diffusion metrics were computed within each functional region and across the regions; local and global network-based metrics were calculated as well.

**Table 6.2:** Mapping of the Default Mode Network (DMN) sub-regions to the corresponding anatomical regions of the AAL2 atlas.

| DMN Sub-region | AAL2 Constituent ROIs | N. ROI |
|---|---|---|
| DMN_PCC_Precuneus | Precuneus (L/R), Cingulum Post (L/R) | 4 |
| DMN_mPFC | Frontal Med Orb (L/R), Frontal Sup Medial (L/R) | 4 |
| DMN_Hippocampus_MTL | Hippocampus (L/R), ParaHippocampal (L/R) | 4 |
| DMN_Angular | Angular (L/R) | 2 |
| DMN_IPL | Parietal Inf (L/R) | 2 |
| **Total** | | **16** |

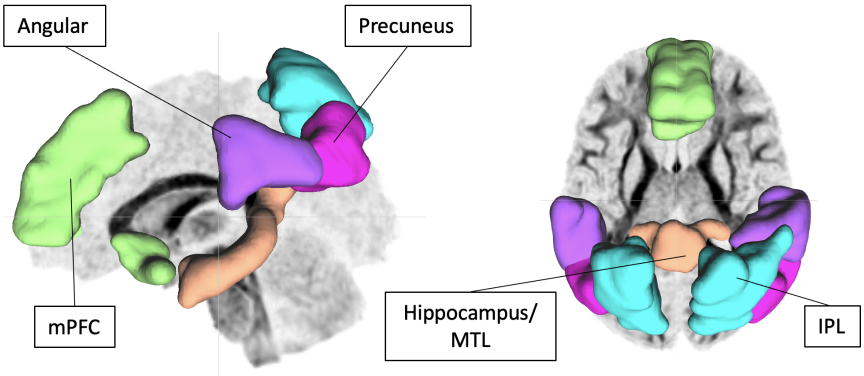

**Figure 6.3:** From left to right, sagittal and axial views of the Default Mode Network (DMN) system. These illustrations were created via *DSI Studio* and refer to subject EC2132 of the real-world dataset analyzed in this thesis.

**Table 6.3:** Mapping of the Limbic System sub-regions to the corresponding anatomical regions of the AAL2 atlas.

| **Limbic Sub-region** | **AAL2 Constituent ROIs** | **N. ROI** |
|---|---|---|
| LIMBIC_Hippocampus | Hippocampus (L/R) | 2 |
| LIMBIC_Parahippocampal | ParaHippocampal (L/R) | 2 |
| LIMBIC_Amygdala | Amygdala (L/R) | 2 |
| LIMBIC_Cingulate | Cingulate Ant/Mid/Post (L/R) | 6 |
| LIMBIC_Temporal_Pole | Temporal Pole Sup/Mid (L/R) | 4 |
| **Total** | | **16** |

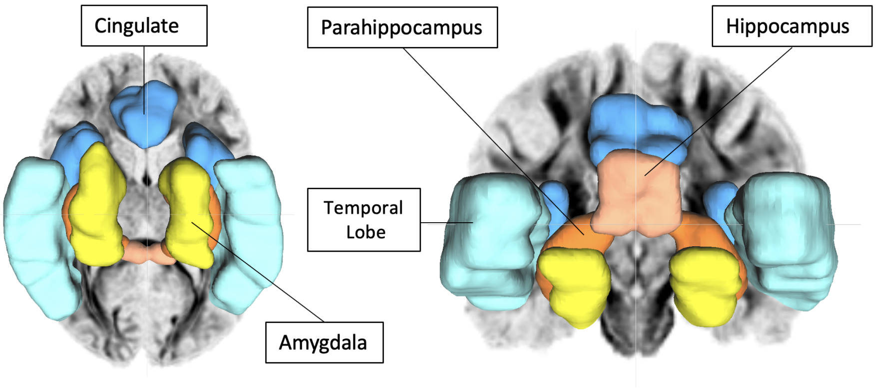

**Figure 6.4:** From left to right, axial and coronal view of the Limbic System. These illustrations were created via *DSI Studio* and refer to subject EC2132 of the real-world dataset analysed in this thesis.

### Level 4: Macro-Edges

The last level involves the direct analysis of the edges (connections) themselves. This *edge-based* approach focuses on the specific white matter fascicles connecting two regions. In particular, we considered every connection between anatomical macro regions and DMN and Limbic functional regions as well.

Figure 6.5 provides a schematic representation of the hierarchical framework. Notice that the sketch below is manually drawn and imprecise but should make the concept of brain levels clearer.

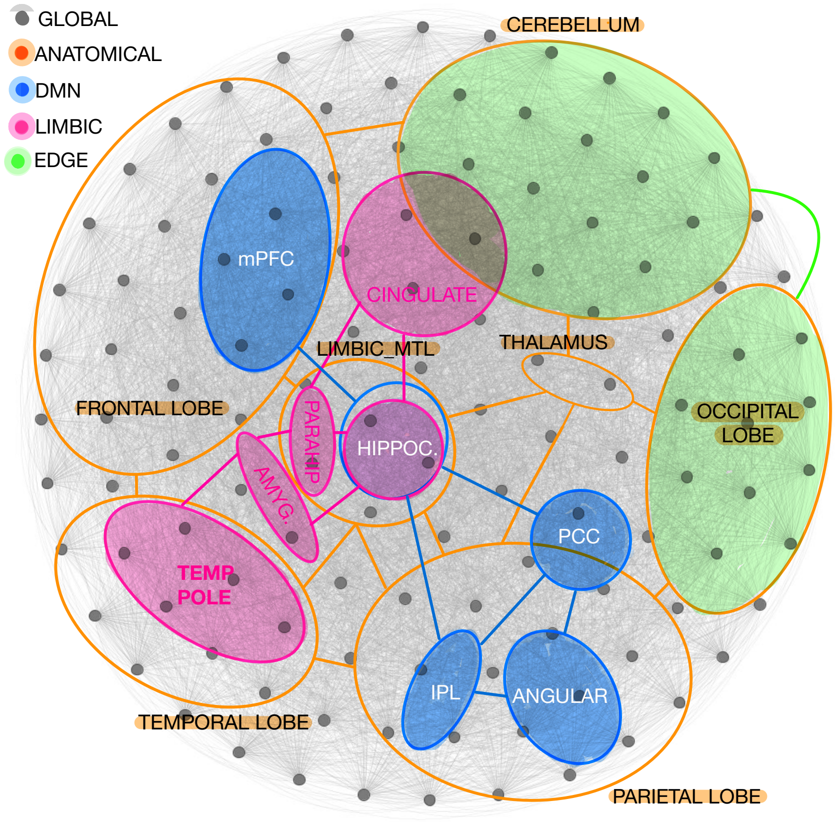

**Figure 6.5:** Illustrative sketch of the Multi-Scale Framework for AAL2 atlas. Underlying graph created with Gephi.

We will now examine more closely which conventional DTI and network-based differ across groups.

## 6.2. Conventional Diffusion Metrics across levels

Regarding conventional diffusion metrics, the following were considered: Quantitative Anisotropy (QA), Fractional Anisotropy (FA), Mean Diffusivity (MD), Radial Diffusivity (RD), Restricted Diffusion Index (RDI) and Quantitative Isotropy Reconstruction (QIR). Some of them are DTI metrics, while others are specific to QSDR.

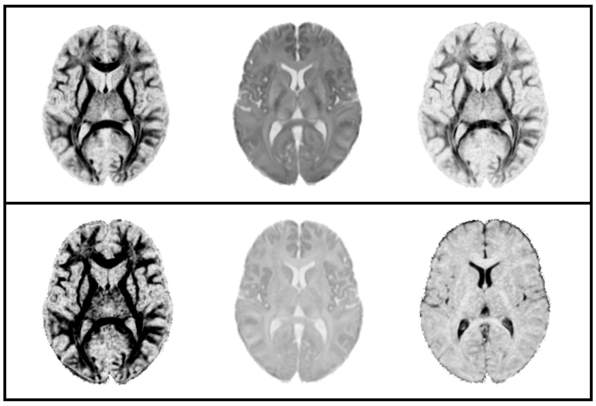

**Figure 6.6:** Diffusion Metrics. On the first row, QSDR Metrics for subject EC2132: QA, RDI, QIR. On the second row, DTI Metrics: FA, MD, RD.

In Level 1, we directly analyzed the metric values extracted from DSI Studio for each ROI. In addition, we computed the mean and the standard deviation across all ROIs in the whole brain. The standard deviation was introduced as a measure of strucutural heterogeneity. For Level 2 and 3, once again, we computed the mean and standard deviation within each macro-region, either anatomical or functional, and across macro-regions as well. These allowed to assess micro-structural tissue degradation. Finally, Level 4 wasn't performed for classical metrics.

As reported in table 6.4, which summarizes significant differences in white matter metrics, we observe lower FA in the Temporal Lobe and Cingulate of TLE patients, consistent with the findings of *Bonilha et al.* [8]. Furthermore, it is evident that the Frontal Lobe is highly affected by TLE, confirming the degradation evidence commonly reported.

Figure 6.7 illustrates the AAL2 regions where diffusion metrics are significantly increased in healthy controls with respect to TLE patients. In these regions, represented in red, TLE patients present a loss of structural integrity.

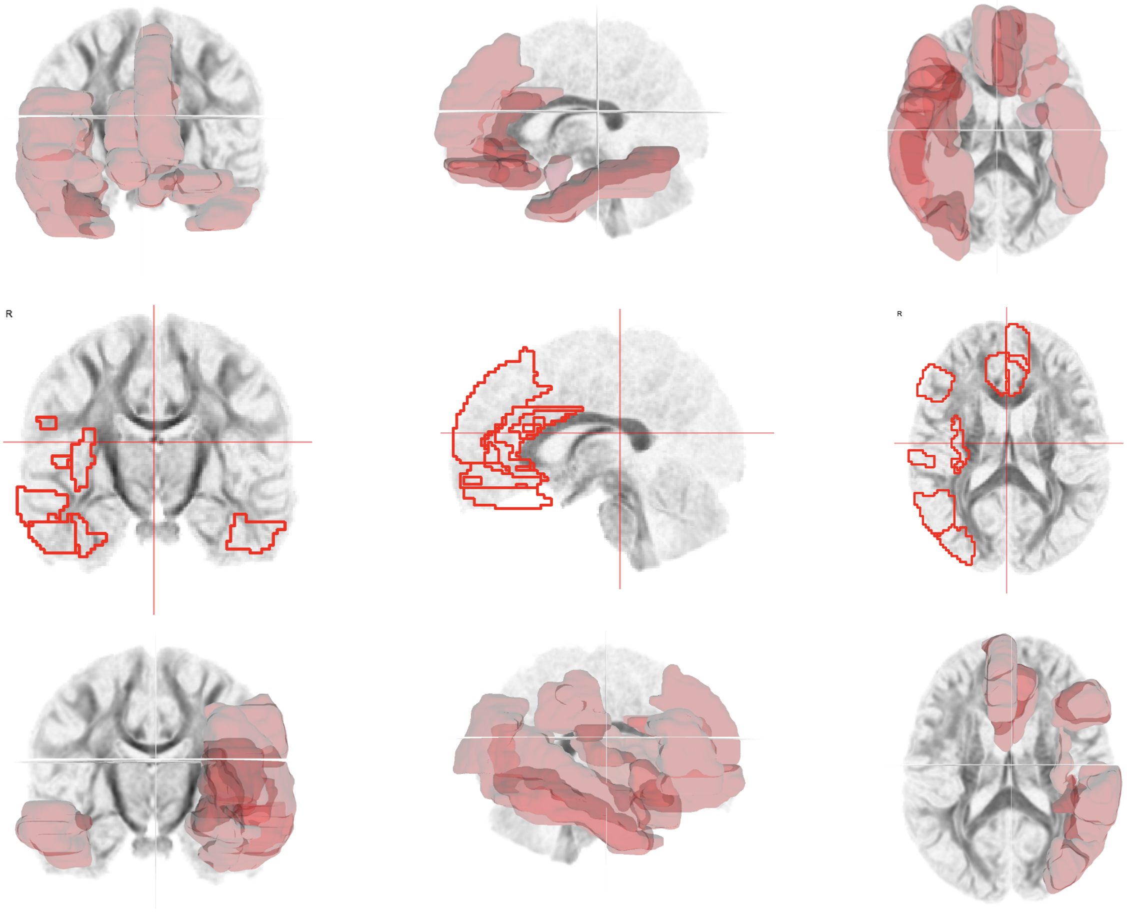

**Figure 6.7:** AAL2 regions where diffusion metrics are significantly increased in healthy controls compared to TLE patients are highlighted in red. From left to right, the images display the coronal, sagittal, and axial views.

Another interesting and logical result is the increase in RDI and QIR variance within the Hippocampus and the Thalamus of TLE patients, respectively. This phenomenon reflects a higher micro-structural *heterogeneity* in TLE, likely implied by the simultaneous presence of cell necrosis and the formation of novel local re-entrant connections within this focal region.

**Table 6.4:** Significant differences in white matter metrics between Healthy Controls (HC) and Temporal Lobe Epilepsy (TLE) patients.

| **Region / Metric** | ***p*-raw** | ***p*-FDR** | **Direction** |
|---|---|---|---|
| Frontal_Med_Orb_R (FA) | 0.0000 | 0.0002 | HC > TLE |
| Rectus_L (FA) | 0.0000 | 0.0000 | HC > TLE |
| Temporal_Inf_R (FA) | 0.0000 | 0.0000 | HC > TLE |
| OFCant_L (FA) | 0.0000 | 0.0001 | HC > TLE |
| OFCpost_L (FA) | 0.0000 | 0.0002 | HC > TLE |
| Frontal_Sup_Medial_L (FA) | 0.0000 | 0.0010 | HC > TLE |
| Temporal_Pole_Sup_R (FA) | 0.0000 | 0.0009 | HC > TLE |
| mean_DMN_mPFC (FA) | 0.0000 | 0.0001 | HC > TLE |
| mean_Temporal (FA) | 0.0000 | 0.0001 | HC > TLE |
| mean_DMN (FA) | 0.0000 | 0.0005 | HC > TLE |
| Frontal_Inf_Orb_2_R (FA) | 0.0000 | 0.0011 | HC > TLE |
| Fusiform_R (FA) | 0.0000 | 0.0016 | HC > TLE |
| Occipital_Mid_R (FA) | 0.0000 | 0.0012 | HC > TLE |
| SupraMarginal_R (FA) | 0.0000 | 0.0013 | HC > TLE |
| Temporal_Mid_R (FA) | 0.0000 | 0.0014 | HC > TLE |
| Cingulate_Ant_R (FA) | 0.0005 | 0.0145 | HC > TLE |
| Frontal_Inf_Tri_R (FA) | 0.0001 | 0.0064 | HC > TLE |
| Heschl_R (FA) | 0.0001 | 0.0054 | HC > TLE |
| Insula_R (FA) | 0.0004 | 0.0127 | HC > TLE |
| Amygdala_L (FA) | 0.0013 | 0.0293 | HC > TLE |
| Cingulate_Ant_L (FA) | 0.0008 | 0.0213 | HC > TLE |
| Temporal_Inf_L (FA) | 0.0002 | 0.0081 | HC > TLE |
| Heschl_R (RD) | 0.0017 | 0.0338 | TLE > HC |
| stdev_Thalamus (QIR) | 0.0023 | 0.0439 | TLE > HC |
| stdev_DMN_Hippocampus (RDI) | 0.0017 | 0.0338 | TLE > HC |

## 6.3. Structural Connectomic Profiles across Levels

Let's now analyze structural network-based measures: from Level 1 to Level 4.

### 6.3.1. Level 1

In Level 1, a graph is built for every subject directly from the 120x120 connectivity matrix resulting from tractography with AAL2 brain parcellation. Below we include a visual comparison of the average connectivity matrices for both groups. We immediately see a generalized decrease in connectivity shown by the reddish color of the third matrix.

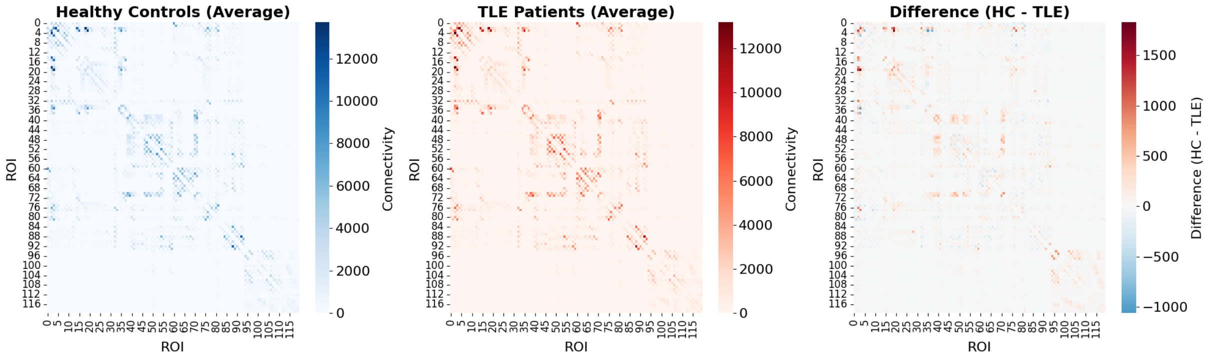

**Figure 6.8:** From right to left: Average HC connectivity matrix, Average TLE connectivity matrix and heatmap of difference of previous two. Average matrices were computed by averaging the number of streamlines connecting each couple of regions.

Moreover, as detailed in Chapter 4, a second binary matrix is constructed where a 0 corresponds to the absence of streamlines between two regions and a 1 to the presence of at least 1. Then graph properties are computed for each subject's two graphs.

Table 6.5 summarizes relevant results for *global metrics*. The most relevant finding is the increased number of communities ($p = 0.0379$) in TLE, which indicates a **fragmentation** of the brain network into more isolated modules. Furthermore, we observe trends of connectivity loss, shown by a reduction in average strength and global efficiency. Paradoxically, the average clustering coefficient, although not significant, is higher in TLE patients. These patterns suggest a reduction in long-range connections and super-hubs, which function as information bridges in the brain. These alterations cause inefficiencies in information transfer, increased vulnerability when nodes are attacked and hyper-synchronization of local networks. In summary, they depict a picture of network *regularization*, which is consistent with the literature.

**Table 6.5:** Differences in global graph metrics between Healthy Controls (HC) and TLE patients (Uncorrected $p < 0.05$). Metrics reported for weighted and binary matrices.

| **Metric** | **$p$-raw** | **$p$-FDR** | **Direction** | **Significance** |
|---|---|---|---|---|
| *Weighted Connectivity Matrix* | | | | |
| Num. Communities | 0.0379 | 0.1883 | TLE > HC | Difference Found |
| Global Efficiency | 0.0508 | 0.1883 | HC > TLE | Near Significance |
| Avg. Strength | 0.0554 | 0.1883 | HC > TLE | Near Significance |
| Avg. Clustering | 0.0981 | 0.2084 | TLE > HC | Near Significance |
| *Binary Connectivity Matrix* | | | | |
| Small Worldness | 0.0584 | 0.1829 | HC > TLE | Near Significance |
| Avg. Closeness Centrality | 0.0704 | 0.1829 | HC > TLE | Near Significance |
| Density | 0.0773 | 0.1829 | HC > TLE | Near Significance |

Just a final remark on global efficiency: we observed a lower trend in TLE. In their respective works, *Bonilha et al.* reported no significance, *DeSalvo et al.* demonstrated an increase, and *Liu et al.* noted a decrease. These results may seem in contrast, but they depend on the parcellation chosen and on the actual formula used to compute efficiency.

Regarding *local* properties, involving specific ROIs, there isn't any nodal metric which is significant after FDR correction. Nevertheless, we have included in Appendix C uncorrected significant metrics. In general, we notice that several Frontal ROIs exhibit a loss in connectivity, local efficiency and centrality. Conversely, Temporal ROIs show an increase in the clustering coefficient, reflecting a pathological local hyper-connectivity and potentially reinforcing the seizure mechanisms.

### 6.3.2. Level 2

In Level 2 we mapped each AAL2 ROI to one of 12 anatomical macro-regions. The illustration below displays the connected components for both weighted and binary graphs, where nodes are color-coded according to their respective macro-regions.

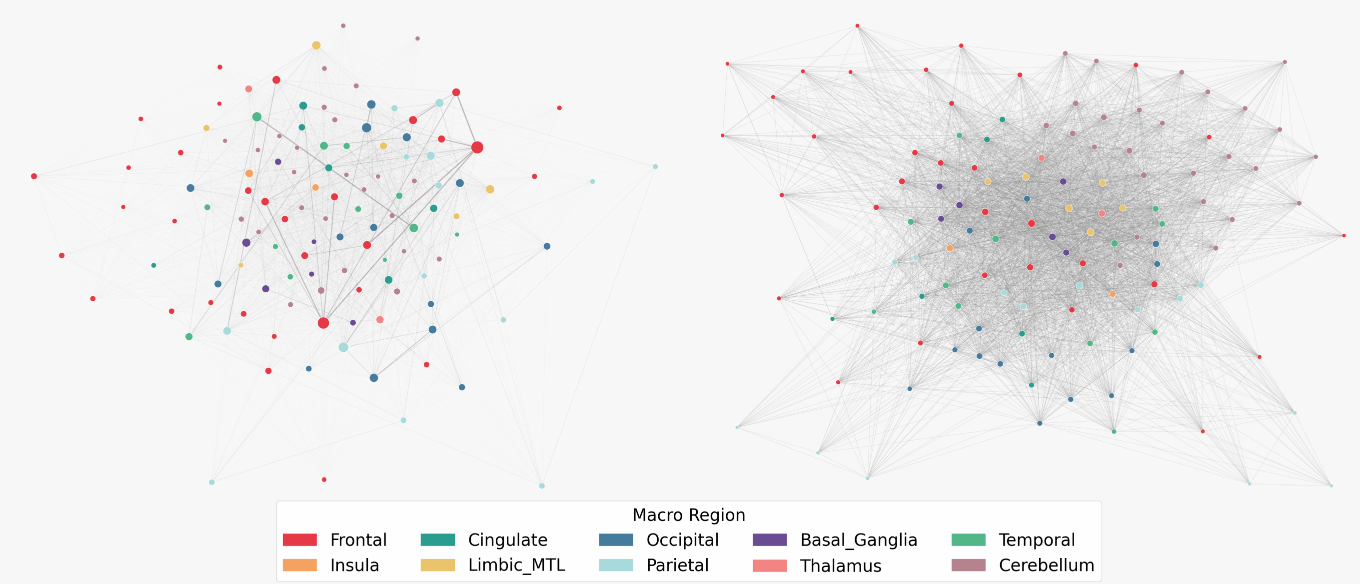

**Figure 6.9:** Connected component of Weighted (left) and Binary (right) global networks for EC2132. Spatial distribution is determined by the FR algorithm; node colors by macro-regional partitions.

First, for each region, a subgraph was built considering only the corresponding nodes and edges. We then conducted an *intra-region* connectivity analysis. Notice that not all the metrics computed in Level 1 are defined for all anatomical regions, as the subgraphs were sometimes too small.

As shown in table 6.6, none of the metrics is statistically significant after FDR correction. Nevertheless, we observe a pattern of **diffuse degradation** and inefficiency in the Frontal Lobe, Occipital Lobe and the Cerebellum. This confirms that structural damages of temporal lobe epilepsy actually extend outside the epileptogenic centers. At this point, one may wonder why the limbic and temporal regions are not intra-regionally significant. It is likely that neuroplastic reorganization processes mask local intra-regional alterations; in other words, cell necrosis might be balanced by new pathological re-entrant connections.

**Table 6.6:** Significant differences in intra-regional network metrics between Healthy Controls (HC) and TLE patients (Uncorrected $p < 0.05$).

| **Region / Metric** | **$p$-raw** | **$p$-FDR** | **Direction** |
|---|---|---|---|
| *Frontal* | | | |
| Avg. Shortest Path (Weighted) | 0.0168 | 0.2551 | TLE > HC |
| Avg. Strength Centrality (Weighted) | 0.0462 | 0.3619 | HC > TLE |
| Avg. Closeness Centrality (Weighted) | 0.0256 | 0.3168 | HC > TLE |
| Avg. Strength (Weighted) | 0.0462 | 0.3619 | HC > TLE |
| Total Strength (Weighted) | 0.0462 | 0.3619 | HC > TLE |
| *Occipital* | | | |
| Avg. Shortest Path (Weighted) | 0.0049 | 0.1758 | TLE > HC |
| Avg. Degree Centrality (Weighted) | 0.0097 | 0.1758 | HC > TLE |
| Avg. Closeness Centrality (Weighted) | 0.0053 | 0.1758 | HC > TLE |
| Avg. Eigenvector Centrality (Weighted) | 0.0032 | 0.1758 | HC > TLE |
| Density (Binary) | 0.0087 | 0.1758 | HC > TLE |
| Avg. Clustering (Binary) | 0.0347 | 0.3508 | HC > TLE |
| Transitivity (Binary) | 0.0138 | 0.2244 | HC > TLE |
| Avg. Shortest Path (Binary) | 0.0097 | 0.1758 | TLE > HC |
| Avg. Degree Centrality (Binary) | 0.0097 | 0.1758 | HC > TLE |
| Avg. Betweenness Centrality (Binary) | 0.0100 | 0.1758 | TLE > HC |
| Avg. Closeness Centrality (Binary) | 0.0084 | 0.1758 | HC > TLE |
| Avg. Eigenvector Centrality (Binary) | 0.0331 | 0.3504 | HC > TLE |
| Small-Worldness (Binary) | 0.0094 | 0.1758 | TLE > HC |
| *Parietal* | | | |
| Avg. Betweenness Centrality (Weighted) | 0.0065 | 0.1758 | HC > TLE |
| *Temporal* | | | |
| Avg. Betweenness Centrality (Weighted) | 0.0456 | 0.3619 | TLE > HC |
| *Cerebellum* | | | |
| Global Efficiency (Weighted) | 0.03424 | 0.3466 | HC > TLE |
| Avg. Strength Centrality (Weighted) | 0.0284 | 0.3345 | HC > TLE |
| Avg. Strength (Weighted) | 0.0284 | 0.3345 | HC > TLE |
| Total Strength (Weighted) | 0.0284 | 0.3345 | HC > TLE |
| Avg. Edge Weight (Weighted) | 0.0400 | 0.3753 | HC > TLE |
| Avg. Clustering (Binary) | 0.0478 | 0.3753 | HC > TLE |

Additionally, we analyzed the interactions between anatomical macro-regions by building a *super-graph* of 12 nodes. By looking at the visualizations below, which compare graphically the average control with the average TLE patient, the overall reduction in brain connectivity is clearly visible. Indeed, in the third matrix, the red color dominates. Additionally, the connectogram suggests that the intra-regional degradation of the Frontal and Occipital lobes, as well as the Cerebellum, may be associated with a more complex **isolation** mechanism of such regions. Generally, it appears that several regions actually suffer from this: the network appears quite fragmented. However, there are few exceptions. One of them is the Thalamus, as also found in *Bonilha et al.* [8], which on average interacts more with the Limbic System, the Cingulate and the Insula in TLE patients. On a final note, it's crucial to remember that these visualizations do not reflect significant differences but are comparisons between the mean control and the mean TLE patient.

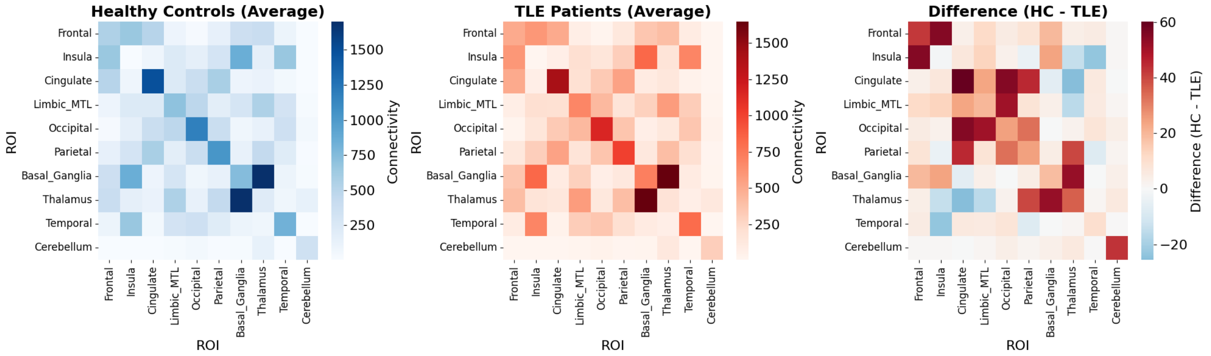

**Figure 6.10:** From right to left: Average HC connectivity matrix, Average TLE connectivity matrix and heatmap of difference of previous two. Average matrices were computed by averaging the number of streamlines connecting each couple of regions.

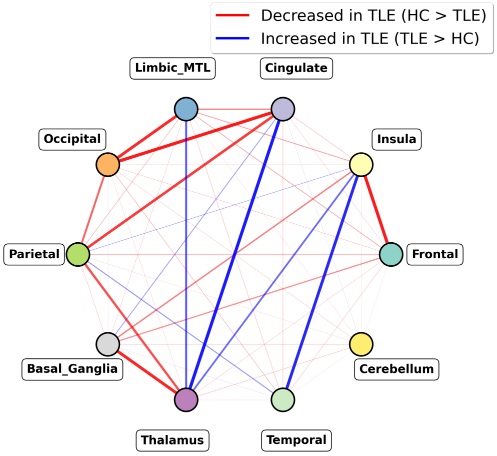

**Figure 6.11:** Connectogram of the anatomical super-graph.

Regarding significant differences at a *global* level, although no metric is significant after FDR, we observe a stronger trend toward *regularization* with respect to Level 1. The p-values of global indicators such as average strength and closeness centrality, total strength and the standard deviation of strength, are now below the threshold of 0.05 if uncorrected (6.7). This increased in statistical power suggests that the macro-regional aggregation of ROIs reduces noise and better capture general epilepsy brain dynamics.

**Table 6.7:** Significant differences in whole-brain anatomical supergraph metrics between Healthy Controls (HC) and TLE patients (Uncorrected $p < 0.05$).

| **Metric** | ***p*-raw** | ***p*-FDR** | **Direction** |
|---|---|---|---|
| *Weighted Metrics* | | | |
| Avg. Shortest Path | 0.0423 | 0.1570 | TLE > HC |
| Avg. Strength Centrality | 0.0384 | 0.1570 | HC > TLE |
| Avg. Closeness Centrality | 0.0319 | 0.1570 | HC > TLE |
| Avg. Strength | 0.0384 | 0.1570 | HC > TLE |
| Total Strength | 0.0384 | 0.1570 | HC > TLE |
| Std. Strength | 0.0417 | 0.1570 | HC > TLE |
| Avg. Edge Weight | 0.0328 | 0.1570 | HC > TLE |

Moving on to super-graph's significant *local* metrics, several regions show a pattern of **reduction in local efficiency and closeness centrality**. This confirms the connectogram's findings about nodal isolation. In other words, many regions no longer act as effectively as before as bridges for information transfer in the network.

These results are partially different from the findings of *Liu et al.* [22], which reported a decrease in 17 cortical regions of the left temporal, bilateral frontal, and bilateral parietal lobes.

**Table 6.8:** Significant differences in super-node metrics (Uncorrected $p < 0.05$).

| **Region** | **Metric** | ***p*-raw** | ***p*-FDR** | **Direction** |
|---|---|---|---|---|
| Insula | Closeness | 0.0376 | 0.3291 | HC > TLE |
| Insula | Local Efficiency (Weighted) | 0.0333 | 0.3291 | HC > TLE |
| Cingulate | Closeness | 0.0222 | 0.3291 | HC > TLE |
| Limbic MTL | Closeness | 0.0137 | 0.3291 | HC > TLE |
| Occipital | Closeness | 0.0084 | 0.3291 | HC > TLE |
| Parietal | Closeness | 0.0159 | 0.3291 | HC > TLE |
| Cerebellum | Strength | 0.0231 | 0.3291 | HC > TLE |

### 6.3.3. Level 3

The third level is the functional one. While in Level 2 we built an anatomical dictionary associating to each AAL2 ROI an anatomical macro-region, in Level 3 we focused only on the ROIs belonging to the Default Mode Network (DMN) and the Limbic System and constructed functional *super-graphs*. Since these networks consist of a limited number of nodes, for this level we omitted the intra-region connectivity analysis and performed only the inter-region one.

**Default Mode Network (DMN):**

Regarding the DMN, we finally observe several metrics that remain significant after FDR correction (Table 6.9). As established in the work of *DeSalvo et al.* [11], the DMN is extremely affected by TLE, and our structural results provide a quantitative basis for its alterations. In this specific network, TLE patients exhibit a significant decrease in **average strength and density**. Furthermore, the increase in the average shortest path and the decrease in closeness centrality suggest a loss of internal integration, characterizing a less efficient information transfer. If aggregating the ROIs anatomically was effective in reducing noise, restricting the analysis to the DMN allows us to focus precisely on the core of network-based alterations.

**Table 6.9:** Significant differences in DMN Supergraph metrics between Healthy Controls (HC) and Temporal Lobe Epilepsy (TLE) patients after FDR correction.

| **Feature / Metric** | **$p$-raw** | **$p$-FDR** | **Direction** |
|---|---|---|---|
| *Weighted Metrics* | | | |
| Avg. Strength Centrality | 0.0029 | 0.0193 | HC > TLE |
| Avg. Strength | 0.0029 | 0.0193 | HC > TLE |
| Total Strength | 0.0029 | 0.0193 | HC > TLE |
| Avg. Edge Weight | 0.0192 | 0.0489 | HC > TLE |
| *Binary Metrics* | | | |
| Num. Edges | 0.0244 | 0.0489 | HC > TLE |
| Density | 0.0244 | 0.0489 | HC > TLE |
| Avg. Degree Centrality | 0.0244 | 0.0489 | HC > TLE |
| Transitivity | 0.0304 | 0.0489 | HC > TLE |
| Avg. Shortest Path | 0.0304 | 0.0489 | TLE > HC |
| Avg. Betweenness Centrality | 0.0305 | 0.0489 | TLE > HC |
| Avg. Closeness Centrality | 0.0306 | 0.0489 | HC > TLE |
| Avg. Clustering | 0.0318 | 0.0489 | HC > TLE |

The boxplots in Figure 6.12 give a closer look to the most relevant significant weighted and binary global DMN metrics.

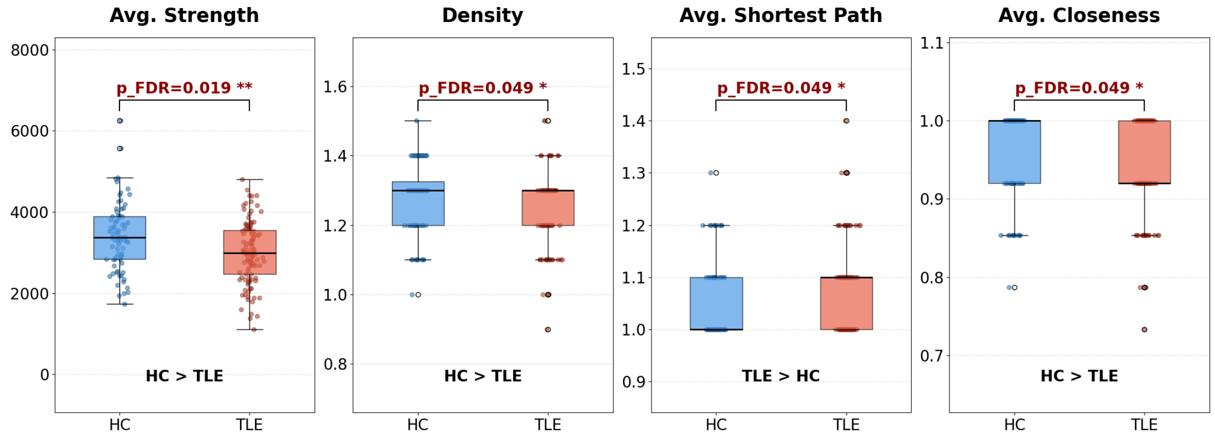

**Figure 6.12:** Boxplots of DMN significant global metrics across Groups.

Concerning nodal properties (Table 6.10), we observe a widespread pattern of **decreased local efficiency** in key regions such as the Medial Temporal Lobe (MTL), the Posterior Cingulate Cortex and the Precuneus (PCC/Precuneus). Aditionally, the Medial Prefrontal Cortex (mPFC) and the Posterior Cingulate Cortex/Precuneus (PCC/Precuneus) show a reduction in strength (p=0.0057 and p=0.0238, respectively). Hence, not only is their intra-regional connectivity disrupted, but also their inter-regional one.

**Table 6.10:** Differences in DMN Super-Node metrics between Healthy Controls (HC) and TLE patients (Uncorrected $p < 0.05$).

| Region | Metric | $p$-raw | $p$-FDR | Direction |
|---|---|---|---|---|
| *mPFC* | | | | |
| | Strength | 0.0057 | $> 0.05$ | HC > TLE |
| | Eigenvector Centrality | 0.0252 | $> 0.05$ | HC > TLE |
| | Local Efficiency (Weighted) | 0.0319 | $> 0.05$ | HC > TLE |
| *PCC / Precuneus* | | | | |
| | Strength | 0.0238 | $> 0.05$ | HC > TLE |
| | Local Efficiency (Binary) | 0.0420 | $> 0.05$ | HC > TLE |

To gain a clearer picture of the network's reorganization, we examined the strength distribution across DMN regions. As shown in the violin plots for the mPFC and the Precuneus, there is a clear **loss of super-hubs** in the TLE group. In Healthy Controls, these regions exhibit a high-density long tail of strong connections that guarantees the efficiency of the network; in TLE patients, this distribution collapses, indicating that these former hubs have been downgraded to peripheral nodes. This *de-hubbing* of the mPFC and Precuneus likely drives the global DMN inefficiencies observed.

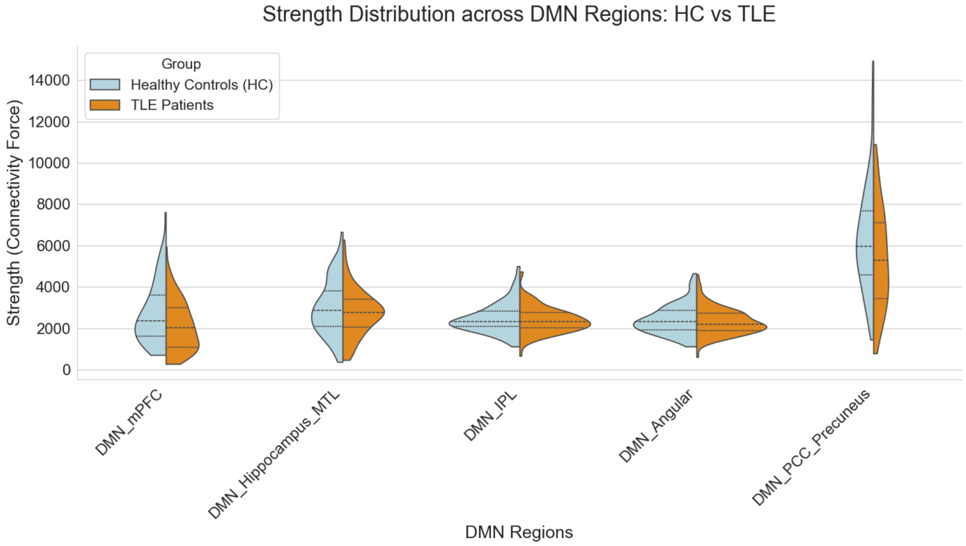

**Figure 6.13:** Violin plots for DMN strength distribution across Groups.

We conclude this subsection by presenting two weighted graphs rapresenting the principal connected components at the ROI level (Level 1) for TLE patient EC2118 and control subject EC2103. In these networks, DMN nodes are specifically color-coded to summarize our findings. These visualizations help integrate the results obtained so far. The graphs were generated using *Gephi* with the ForceAtlas2 algorithm [15]. To improve visual clarity, only connections with a strength exceeding 1000 streamlines are displayed.

Several differences are immediately apparent. First, the cerebellar nodes are absent from the connected component of the TLE patient at this threshold. Furthermore, the DMN connections in the control subject are denser and have thicker edges, visually confirming the higher average DMN strength compared to the TLE group. Another interesting detail is the evident degradation of the Frontal Lobe network (represented in green), which appears with thinner and more sparse edges in the patient. Lastly, it is worth noticing that connections appear to remain robust within the Precuneus (in fuchsia) and the Limbic Area (in orange) for both subjects. This pattern suggests that while local connectivity is relatively preserved, the long-range pathways are damaged in the TLE patient.

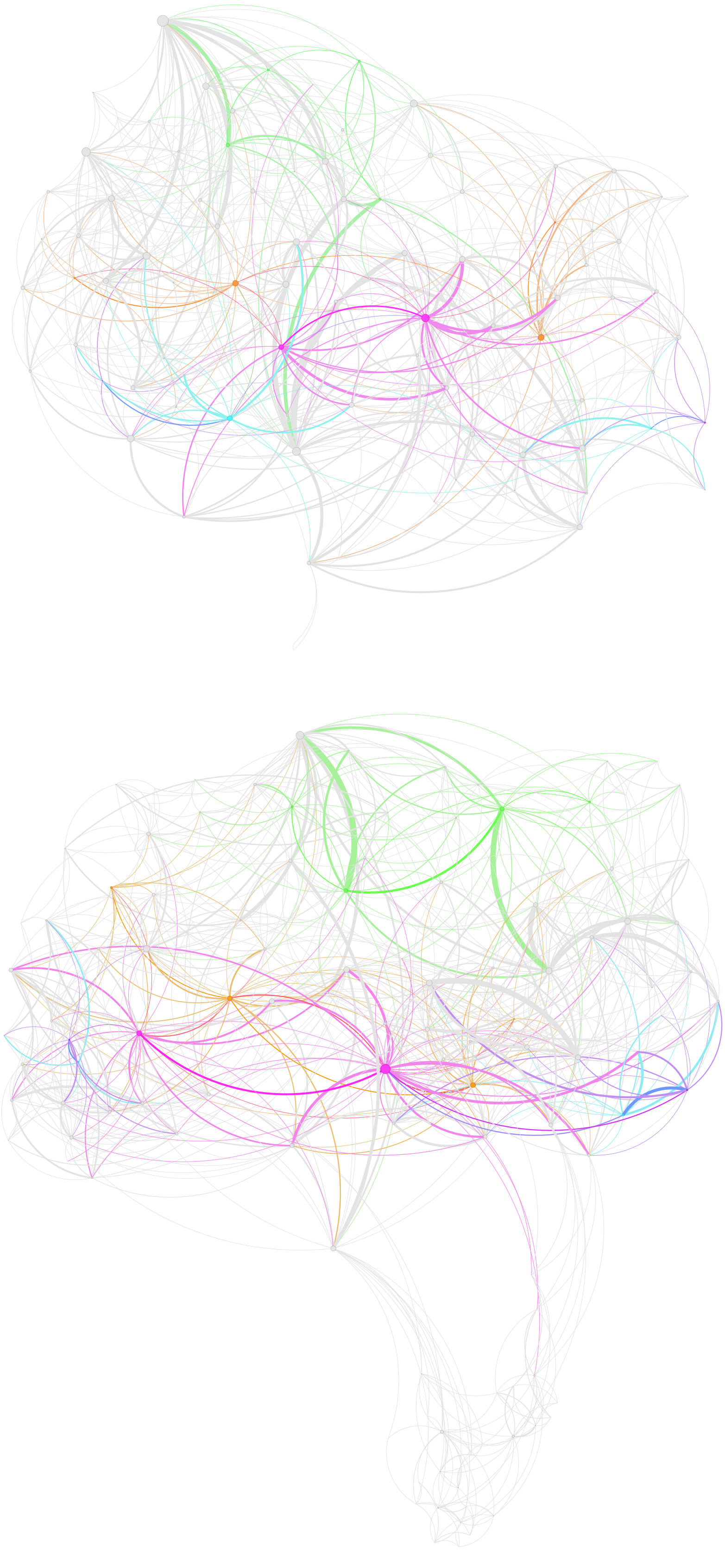

**Figure 6.14:** The visualizations, generated via the ForceAtlas2 algorithm, show the principal connected components with a threshold set at >1000 streamlines, for HC EC2103 and TLE EC2118. Specific DMN nodes are colored: mPFC in green, Hippocampus/MTL in orange, Precuneus in fuchsia, Angular gyrus in purple, and IPL in light blue.

### Limbic System:

We replicated the same analysis for the **Limbic System**, which is the center of structural damage in epilepsy. However, given that our dataset includes a heterogeneous cohort of patients, comprising left, right, and bilateral TLE, both with and without Medial Temporal Sclerosis (MTS), obtaining significant results is challenging: in fact, localized alterations may balanced out across groups.

In general, we found a significant reduction of the standard deviation of node strength (p-value=0.0097 before FDR correction). This means a decrease in heterogenity within the limbic system, further suggesting the *regularization* of the network. Regarding local metrics, we observed a trend toward lower degree for the amygdala in TLE patients.

Furthermore, we have generated violin plots for each functional region of the lymbic system. Specifically, representing the distribution of *super-node* strengths across groups. In the hippocampus, parahippocampal gyrus, amygdala, and temporal pole, we observed a distinct widening of the tummies of the TLE side of the violins. This means that a great density of observations fall around the median, which corresponds to the contraction of the inter-quartile range. This definitely confirms pathological *regularization*.

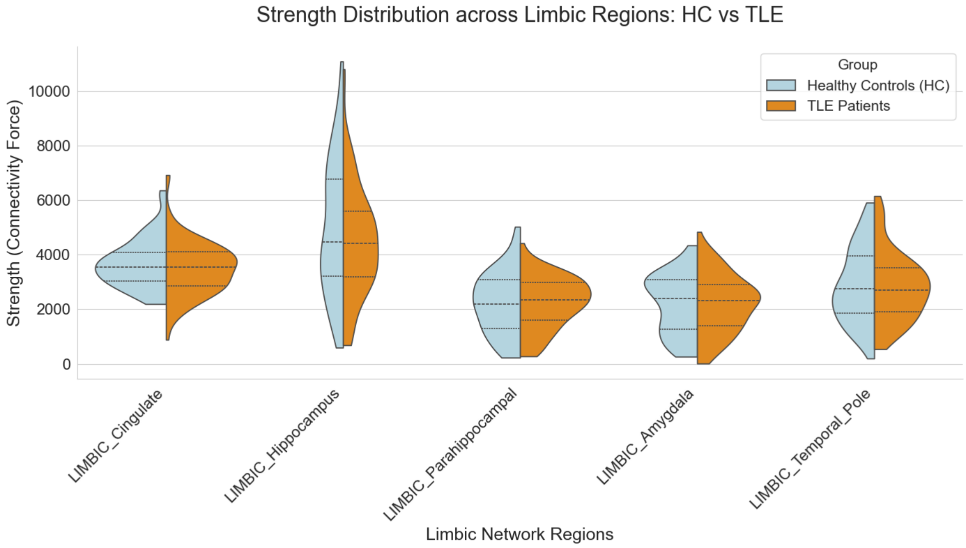

**Figure 6.15:** Violin plots for Limbic System strength distribution across Groups.

Finally, we replicated the visual graph analysis using *Gephi* by specifically color-coding the nodes of the Limbic System. Consistent with the DMN results, the TLE patient's graph is globally sparser in connections compared to the control. However, the intra-network connections within the limbic circuit appear notably thicker in the patient. This visual evidence confirms that while the global network is damaged, connectivity remains robust and exacerbated within the limbic area.

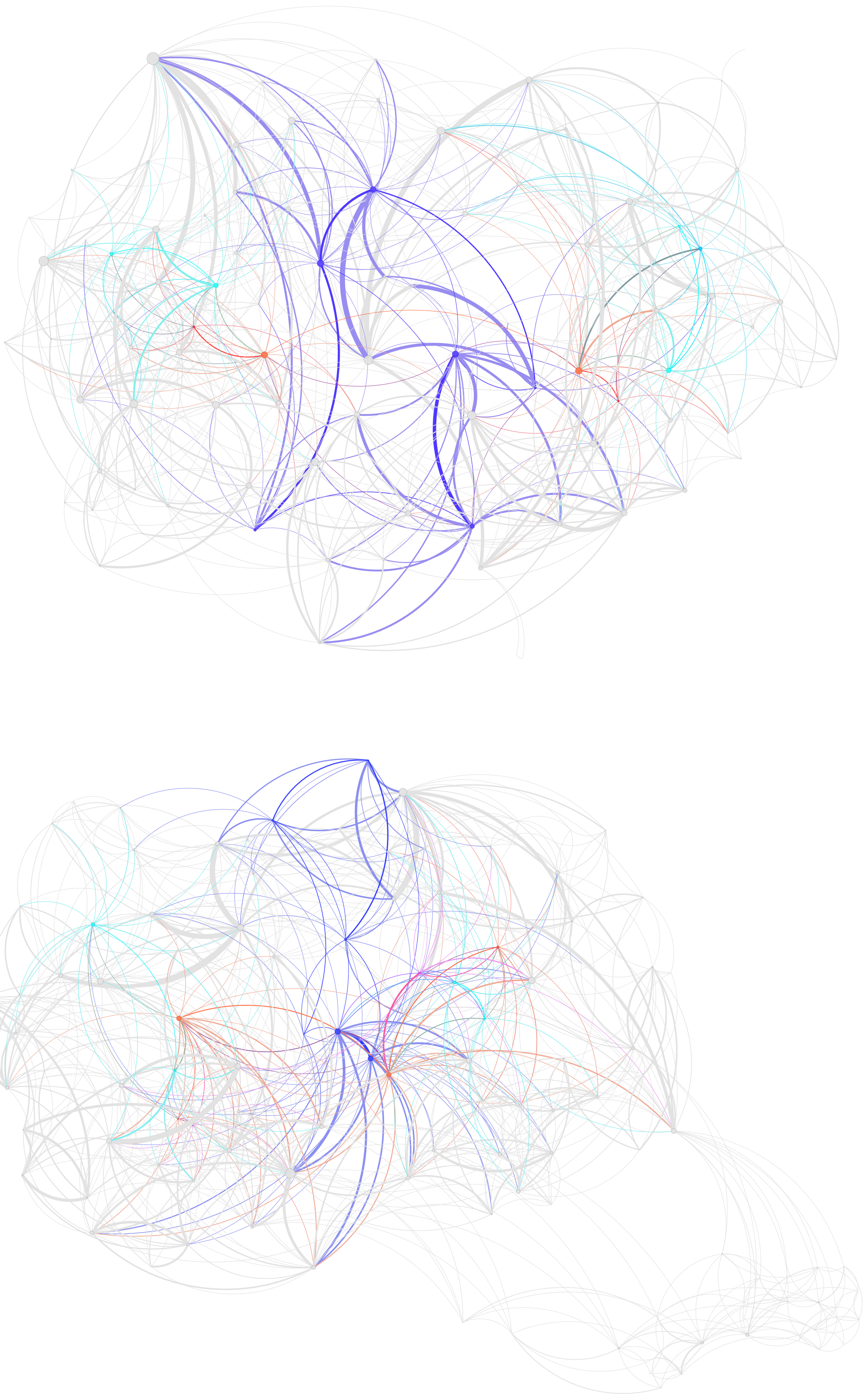

**Figure 6.16:** Comparison of weighted brain networks for a healthy control EC2103 (top) and a TLE patient EC2118 (bottom). The visualizations, generated via the ForceAtlas2 algorithm, illustrate the principal connected components using a threshold of >1000 streamlines. Specific nodes of the Limbic System are color-coded to highlight regional connectivity: Cingulate in blue, Temporal Pole in light blue, Hippocampus in orange, Parahippocampal Gyrus in red and Amygdala in yellow.

### 6.3.4. Level 4

Lastly, we analyzed specific connections between macro-regions. Specifically, we tested the difference in the number of streamlines connecting each pair of anatomical macro-regions and each pair of functional regions within the DMN and the Limbic System.

The only edge that remains significant after FDR correction is the one between the Hippocampus/MTL and the mPFC (p-value=0.0037, p-FDR=0.0374), which is reduced in TLE. This reduction in structural connectivity clinically justifies memory loss and decreased attention, as it reflects a breakdown in the synchronization between the encoding centers and the executive control hubs [35].

We also found several trends of reduced connectivity between the Parietal and Temporal Lobes and between the Limbic System and the Temporal Lobe. The former justifies the impairment in visuospatial processing and the integration of sensory information often observed in chronic TLE patients; the latter justifies the hypersynchrony and isolation of the Limbic System, that could facilitate the propagation of seizures.

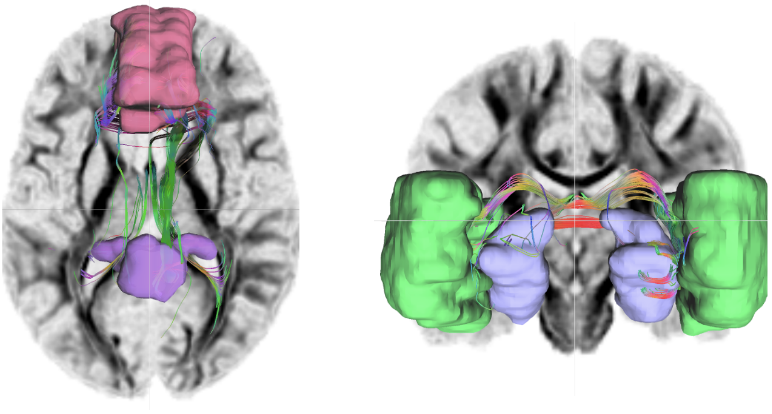

**Figure 6.17:** Tractography between Hippocampus and Prefrontal Cortex (Left); Tractography between Limbic System and Temporal Lobe (Right).

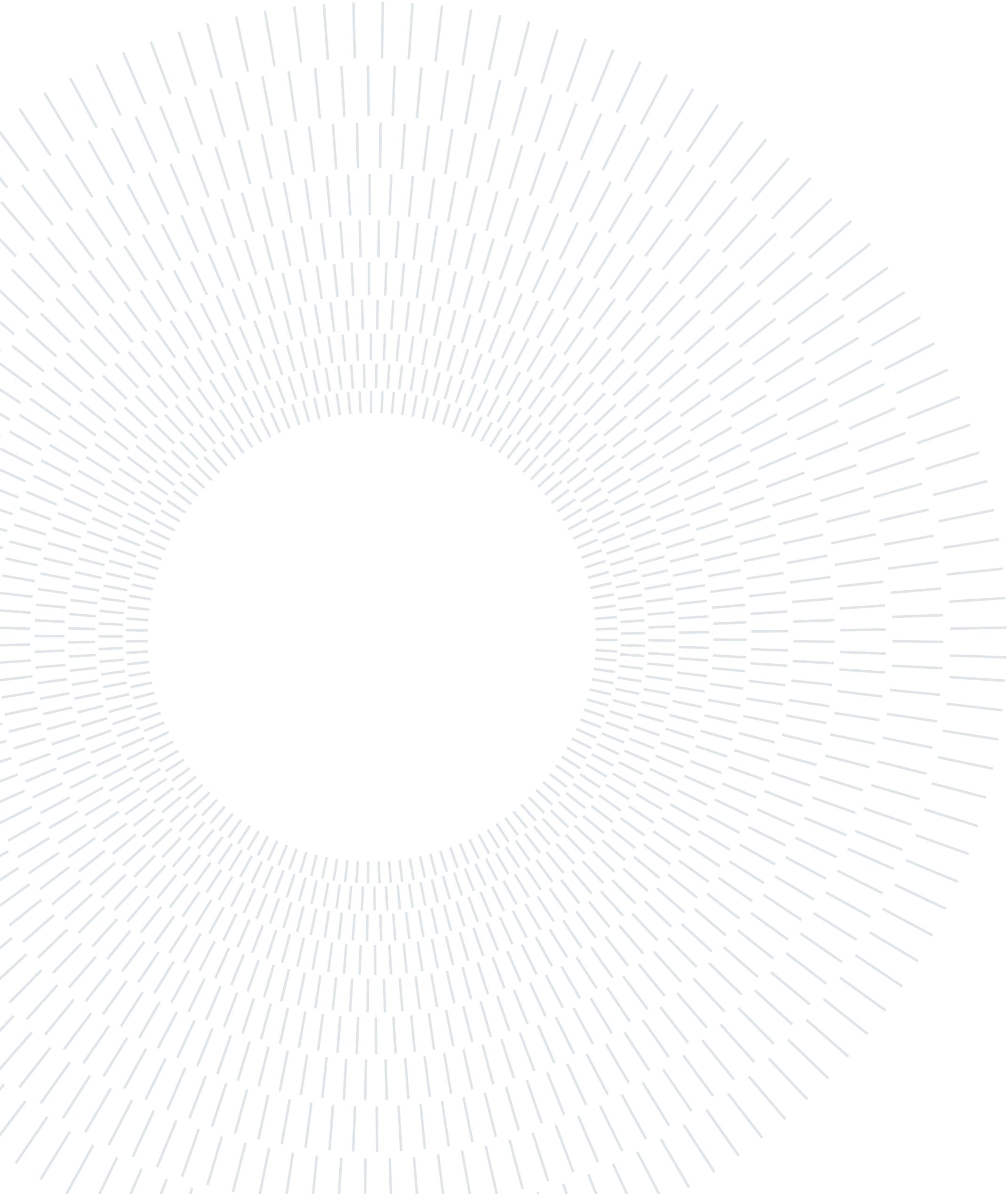

# 7 | Classification of TLE patients vs Controls

After analysing the connectivity differences between temporal lobe epilepsy subjects and controls, we now proceed to classify TLE subjects vs controls. The in-depth analysis presented in the previous chapter served two main goals. First, it allowed us to better understand structural connectivity alterations in epilepsy; second, and more importantly, because exploring significant conventional diffusion and network-based metrics at different hierarchical anatomical and functional levels may also be conceived as a feature extraction process from a classification point of view. Particularly in a medical setting, the optimal design of the features is crucial to guarantee model performance and interpretability.

In this thesis, we performed classification in three distinct scenarios: using *exclusively conventional diffusion metrics*, using *only network-based metrics*, and finally, incorporating *all features* within our multi-scale framework. In the pages below, we present the best classification models for each feature set and we discuss our findings.

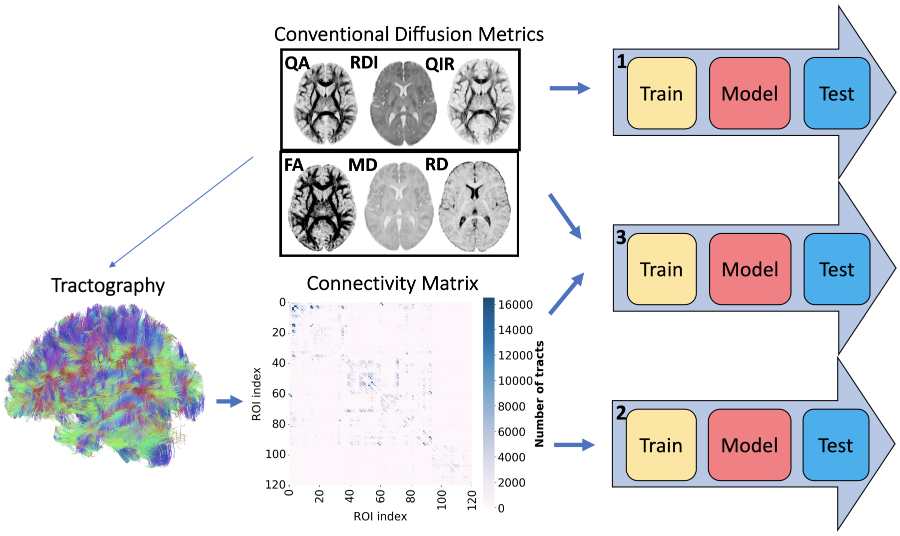

**Figure 7.1:** Overview of the Machine Learning Pipeline. The workflow illustrates the extraction of conventional diffusion metrics and the generation of the connectivity matrix via tractography. These data are then fed into 3 distinct classification models.

### 7.0.1. Classification between TLE and Controls using Conventional Diffusion Metrics

First, we focused exclusively on Conventional Diffusion Metrics. Following feature extraction, conducted through a multi-level approach based on AAL2 connectivity measures, we built a dataset containing the metrics and respective labels for all 181 subjects. As mentioned before, after handling missing values, the pipeline consisted of the *Mann-Whitney* and *Correlation* selectors. Additionally, data were scaled using a *RobustScaler*. Finally, a Support Vector Machine (SVM) was employed, as it proved to be the best model. We set class weight parameter to *balanced* to handle the class imbalance of our dataset. In this pipeline, the parameters to be tuned are several: the thresholds for feature selection and the model's parameters. To optimally select the parameters' configuration, 5-fold Stratified GridSearch was performed. First, it identified the best Mann-Whitney $\alpha$-threshold at 0.05 and the correlation $\beta$-threshold at 0.55. This filter reduced the initial high-dimensional space of 1002 variables to a low-dimensional one of 19 features. Second, the optimized SVM parameters were kernel=rbf, C=10 and gamma=0.001.
The performance of the best model is summarized in the table below:

| **Metric** | **Cross-Validation (Mean ± SD)** | **Test Set** |
|---|---|---|
| Balanced Accuracy | 0.7567 ± 0.048 | 0.7083 |
| F1 Score | 0.7830 ± 0.053 | 0.7500 |
| Precision | 0.8196 ± 0.065 | 0.7500 |
| Recall | 0.7634 ± 0.115 | 0.7500 |
| ROC-AUC | 0.7201 ± 0.046 | 0.7865 |
| Accuracy | 0.7578 ± 0.051 | 0.7143 |
| Specificity | 0.7500 ±0.123 | 0.6667 |

**Table 7.1:** Classification results using Conventional Diffusion metrics. Cross-validation results refer to the training set (85% of the data), while the test set represents the final evaluation on the unseen 15%.

The confusion matrix for the test set is reported below:

$$CM = \begin{bmatrix} 8 & 4 \\ 4 & 12 \end{bmatrix} \tag{7.1}$$

where we correctly identified 8 controls and 12 TLE patients and wrongly labelled 4 false positives and 4 false negatives.

The 19 features selected by the model highlight the involvement of critical regions. In particular, the selection includes diffusion indices from the Temporal and Frontal regions, the Thalamus, the Hippocampus and the Limbic System. To interpret the contribution of different variables in classifying the subjects, we computed the Permutation Importance on the test set. The analysis revealed that out of the 19 initially selected features, two variables (*Temporal Pole Mid Right FA* and *stdev Limbic Temporal Pole RDI*) exhibited near-zero importance. Hence, we further pruned the feature space, retaining only the variables with an absolute importance score >0.0001. After this additional step of feature selection, we ended up with 17 features.

As we can see in table 7.2, while the accuracy and F1 mean scores remained quite stable on the cross-validation and test set, the reduced model showed some improvements. First, the general stability increased, as we can see from the reduced standard deviations; the cross-validation ROC-AUC rose from 72.0% to 79.1% and the recall from 76.3% to 80.8%. However, mean Specificity decreased from 75.0% to 68.9%, signalling the shift towards a more sensitive and less specific model.

Two comments must be made regarding this sensitivity-specificity trade-off. First, the model inherently learns to recognize pathological patterns more effectively than healthy ones due to the dataset imbalance. Hence, the low or unstable specificity is partially a consequence of this. Second, we unfiltered model may present a higher specificity, because it contains features that are not specifically focused on the disease, potentially introducing noise.

Mostly in a medical setting, where recognizing an unhealthy patient is much more important than correctly identifying a healthy one, we favor the second filtered model.

| **Metric** | **Cross-Validation (Mean ± SD)** | **Test Set** |
|---|---|---|
| Balanced Accuracy | 0.7482±0.031 | 0.7083 |
| F1 Score | 0.7925±0.041 | 0.7500 |
| Precision | 0.7893±0.042 | 0.7500 |
| Recall | 0.8078±0.106 | 0.7500 |
| ROC-AUC | 0.7914±0.043 | 0.7917 |
| Accuracy | 0.7578±0.036 | 0.7143 |
| Specificity | 0.6885±0.106 | 0.6667 |

**Table 7.2:** Classification results of the Reduced Model (17 features), using only Conventional Diffusion metrics.

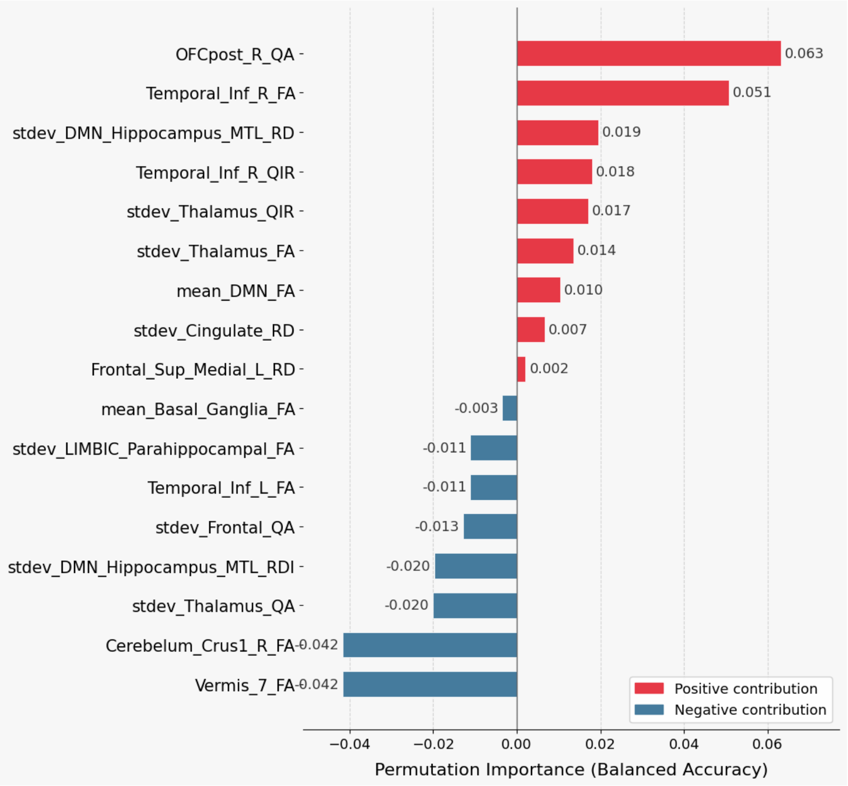

**Figure 7.2:** Permutation Importance for the best model with only Conventional Diffusion features.

Regarding the Permutation Importance analysis (7.2), the most predictive variables primarily involve the right Orbitofrontal Cortex and the Right Inferior Temporal Lobe. These findings are highly consistent with the neurobiological literature on TLE. Moreover, among the selected features, we notice the presence of the standard deviation of diffusion metrics within key regions such as the Hippocampus, the Thalamus, the Cingulate and the Frontal Lobe. This suggests that the structural heterogeneity within these regions is a significant biomarker for TLE. Moreover, features based on a *functional* parcellation were included as well. An example is the inclusion of the mean Fractional Anisotropy (FA) across the Default Mode Network (DMN). This suggests that TLE-related alterations are not confined to isolated structures, as highlighted several times.

### 7.0.2. Classification between TLE and Controls using Network-based Metrics

We now explore the second scenario: here, we approached the classification task using exclusively network-based metrics.
In this pipeline, we employed all four levels of features: the ROI-based global graph, the anatomical macro-regions, the functional networks and the macro-edges. However, we intentionally excluded the nodal features from Level 1. Their inclusion led to severe overfitting; while cross-validation scores remained high, performance on the unseen test set was near-random. By removing these local nodal descriptors, that were 1080 features calculated across the 120 ROIs of the AAL2 atlas, we obtained a more robust model.

The best pipeline has the following characteristics: $\alpha$ threshold 0.1, $\beta$ threshold 0.8, SVM classifier with linear kernel, C=100 and gamma=scale. The performance is summarized in the table below:

| **Metric** | **Cross-Validation (Mean)** | **Test Set** |
|---|---|---|
| Balanced Accuracy | 0.6383 | 0.6042 |
| F1 Score | 0.6736 | 0.6452 |
| Precision | 0.7053 | 0.6667 |
| Recall | 0.6510 | 0.6250 |
| ROC-AUC | 0.6235 | 0.6667 |
| Accuracy | 0.6406 | 0.6071 |
| Specificity | 0.6385 | 0.5000 |

**Table 7.3:** Classification results using Network-based metrics.

The confusion matrix for the test set is reported below:

$$CM = \begin{bmatrix} 7 & 5 \\ 6 & 10 \end{bmatrix} \tag{7.2}$$

In this case, the model correctly identified 7 controls and 10 TLE patients, while failing to classify 5 controls (false positives) and 6 patients (false negatives).
Overall, these results indicate that while network-based metrics do contain a predictive signal, it is notably less specific and more subtle than the one provided by microstructural diffusion indices. The performance dropped substantially compared to the previous models.
However, the fact that the model still performs above chance (ROC-AUC of 66.7%) con-

firms that TLE involves a systemic reorganization of brain connectivity. And perhaps the signal of brain network reorganization, while not sufficient for high-accuracy diagnosis on their own, could provide complementary information to local diffusion markers. In next section, we will join the two set of features to test this hypothesis in our dataset.

### 7.0.3. Classification between TLE and Controls using Conventional Diffusion and Network-based Metrics

Lastly, we tried to combine both conventional diffusion and network-based metrics from AAL2 atlas to classify TLE patients vs controls. For the former category of measures, we integrated as explained in the previous chapter levels 1,2 and 3, while for the latter category 1,2,3 and 4. We will now present the best pipeline in terms of parameter tuning and model selection.

The selected classification model, after several attempts involving Random Forest and Boosting, was once again the Support Vector Machine (SVM). The best Mann-Whitney $\alpha$-threshold was identified at 0.05 and the correlation $\beta$-threshold at 0.6. The two-step filter selected 43 variables from the initial 1500. The optimized SVM parameters were kernel=rbf, C=1 and $\gamma$=0.01. The performance of the model is summarized below:

| **Metric** | **Cross-Validation (Mean ± SD)** | **Test Set** |
|---|---|---|
| Balanced Accuracy | 0.7256±0.027 | 0.7604 |
| F1 Score | 0.7660±0.031 | 0.8333 |
| Precision | 0.7822±0.052 | 0.7500 |
| Recall | 0.7627±0.094 | 0.9375 |
| ROC-AUC | 0.7438±0.033 | 0.7552 |
| Accuracy | 0.7323±0.021 | 0.7857 |
| Specificity | 0.6885±0.127 | 0.5833 |

**Table 7.4:** Classification results using integrated Diffusion and Network metrics (43 features).

The confusion matrix for the test set is reported below:

$$CM = \begin{bmatrix} 7 & 5 \\ 1 & 15 \end{bmatrix} \tag{7.3}$$

where we correctly identified 7 controls and 15 TLE patients, with 5 false positives and 1 false negative.

Once again, also in this third scenario, we computed the Permutation Importance on the test set. This analysis revealed that several variables (such as *Temporal Inf L FA* and *Edge Parietal Temporal*) held zero importance. We therefore pruned the feature space and retained only the variables with an absolute importance score >0.0001: 34 features were preserved.

As shown in Table 7.5, the reduced model (34 features) demonstrated a relevant increase in the discriminative power in cross-validation. Specifically, the mean ROC-AUC rose from 0.7438±0.033 to 0.8442±0.051. This substantial gain in AUC indicates that removing redundant features allowed the model to better distinguish between the two classes by focusing only on the most informative signals. However, this improvement came at the cost of decreased stability. We notice that the standard deviation increases for almost all indexes. In other words, the model is now more sensitive to data patterns specific to epilepsy; however, in the absence of them within certain cross-validation folds, the model hasn't anymore the *safety net* provided by the additional 11 variables that previously stabilized the classification. This is exactly the bias-variance trade-off. The first model has a lower variance and higher bias, whereas the second further filtered model has a higher variance and lower bias.

| **Metric** | **Cross-Validation (Mean ± SD)** | **Test Set** |
|---|---|---|
| Balanced Accuracy | 0.7534±0.056 | 0.7292 |
| F1 Score | 0.7907±0.038 | 0.8000 |
| Precision | 0.8053±0.068 | 0.7368 |
| Recall | 0.7863±0.074 | 0.8750 |
| ROC-AUC | 0.8442±0.051 | 0.7604 |
| Accuracy | 0.7585±0.047 | 0.7500 |
| Specificity | 0.7205±0.141 | 0.5833 |

**Table 7.5:** Classification results using the Final Reduced Model (34 features).

Regarding the Permutation Importance analysis (figure 7.4), the most predictive variables are primarily local and macro-regional conventional diffusion metrics. Nonetheless, several network-based features also appear in top positions, revealing a synergistic interaction between local and systemic markers in distinguishing epilepsy patients.

Specifically, the highest-ranking features include the Fractional Anisotropy (FA) of the Right Inferior Temporal Lobe, the Quantitative Anisotropy (QA) of the Posterior Orbitofrontal Cortex and the standard deviation of diffusion metrics in the Thalamus, the Limbic Area and the Cingulate. These findings are consistent with the models using only classical diffusion measures. However, high importance was also attributed to network-based metrics, such as the *Small-worldness of the Occipital network* and the *Betweenness Centrality of the Parietal weighted network.* Occupying slightly lower positions are the *Closeness in the Limbic area*, the *Edge between the Frontal and the Parietal region* and the *Global Number of Communities* in the weighted network.

These features involve regions and network dynamics typical of epilepsy, as discussed in the previous chapter. It is important to note that our objective in identifying these top-ranked features is not necessarily to find those with the highest statistical difference between groups, but rather to isolate those whose pathological signal is independent and not already captured by conventional diffusion indices.

Lastly, as observed in figure 7.3, the selected features span **all levels of our hierarchical framework**. This suggests that higher hierarchical levels, such as the anatomical and functional supergraphs, capture structural and functional information that is not intrinsically incorporated in lower-level metrics.

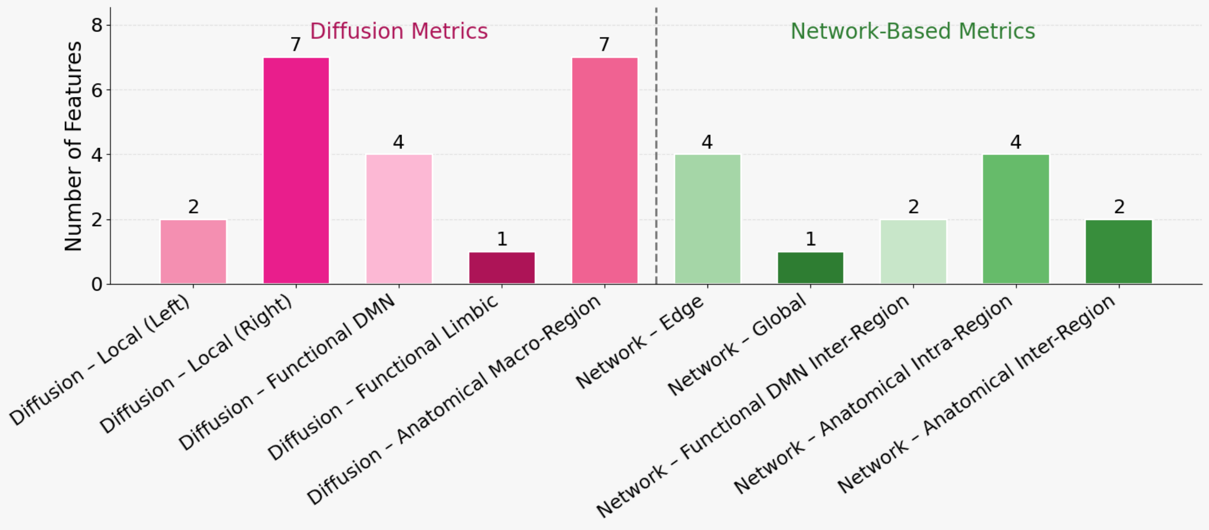

**Figure 7.3:** Selected features by category, after feature selection by Permutation Importance.

In summary, the presence of both domains, diffusion metrics and topological features, across all four levels suggests that TLE is not just a disease of focal microstructural lesions, but a condition characterized by local and global reorganization of brain networks.

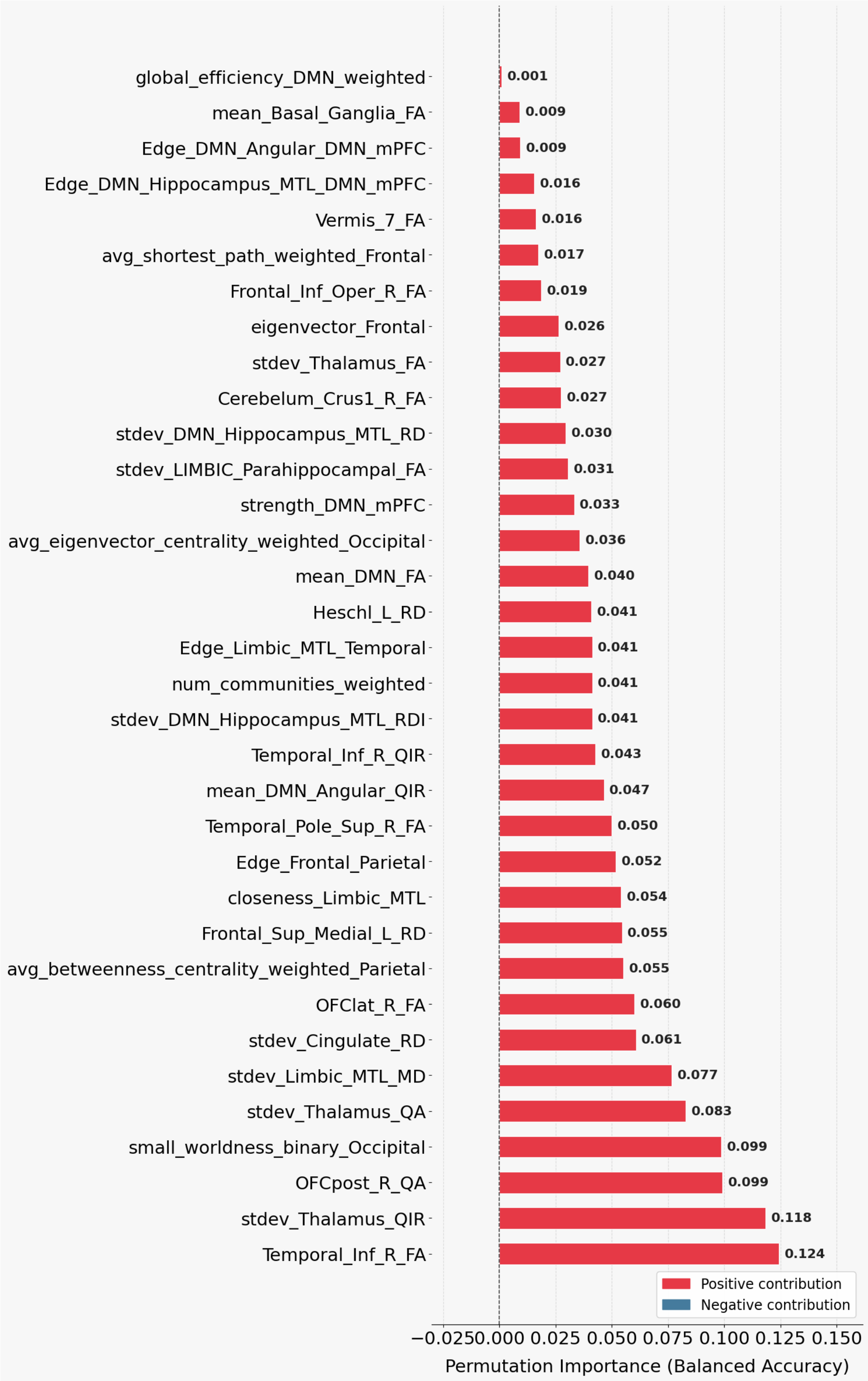

**Figure 7.4:** Permutation Importance for the best model with only Conventional Diffusion features.

## 7.1. Model Comparison and Discussion

Let's now discuss the results of the previous models, with a critical eye on the literature. Regarding the best model using *only diffusion metrics*, the findings are encouraging, as the model slightly outperforms existing literature in the classification of TLE using similar metrics. In cross-validation, it achieved a mean Balanced Accuracy of 74.8% and a mean ROC-AUC of 79.1%. Aditionally, all the other metrics, apart from specificity, are above 75%. The results on the test set are slightly decreased and not showing any overfitting.
With respect to previous models, such as the work of *Cantor-Rivera et al.* [10], which reported an Accuracy of 80.6% at the cost of a low recall of 64.7%, which would mean missing unhealthy subjects, our model has a lower Accuracy of 75.8% but a much higher recall of 80.78%. Notice that in the clinical setting, missing patients may be far worse that having a false positive. Moreover, it's tested on a test set and has a wider dataset (181 vs 38).
Another comparison may be made with the study of *Lee at al.* [21]. Although they focused on general focal epilepsy, they achieved an Accuracy of 76.5% on an unbalanced dataset and with a ROC-AUC of only 60.4%, substantially lower than ours.
Hence, our results indicate that the integration of both anatomical and functional levels, along with local microstructural features, may have improved the model's discriminative power.

Concerning the second scenario, namely the use of *only connectomics*, it is hard to compare our study with the existing literature. Most published studies do not employ a rigorous separation between training and independent test sets, often reporting only cross-validation results. Furthermore, our analysis does not distinguish between right and left TLE, which is a common practice in clinical research and improves classification accuracy. Overall, our model appears to show lower performance compared to studies such as those by *Kamiya et al.* [18] and *Lee et al.* [20]. However, a direct comparison of performance metrics is of limited value given the significant differences in methodological and dataset characteristics.

Moving on to the models incorporating *both diffusion metrics and connectomic profiles*, the first model presented with 43 features showed in cross-validation a mean Balanced Accuracy of 72.6% and mean ROC-AUC of 74.4%. All the other metrics, apart from specificity, performed above 73%. The results on the test set showed slight improvements achieving a Balanced Accuracy of 76.0%, a ROC-AUC of 75.5% and an F1 Score of 83%. While these results do not outperform the best model using exclusively diffusion metrics in terms of absolute mean scores in cross-validation, the standard deviation of these metrics is slightly lower. This suggests that adding network-based features may reduce the variance of the model at the cost of a minimal decrease in performance.

The reduced model with 34 features showed exceptional performance, with a Balanced Accuracy of 75.3%, a ROC-AUC of 84.4%, and an F1-score of 79.0%; the remaining metrics are high as well and the results on the test set consistent (Balanced Accuracy: 72.9%, ROC-AUC: 76.0%, F1 Score: 80.0%). This model outperforms all others presented so far in terms of mean metrics. However, it introduces higher variance compared to both the best model in Scenario 1 and the previous non-reduced model. As previously explained, this suggests that the model is more sensitive to data patterns specific to epilepsy: it has a lower bias and higher variance. Therefore, when these pathological signals don't show up in the data, the model is challenged.

Once again, comparing performances with the literature is difficult and often of limited utility given the differences in methods, classification tasks, and datasets. Nonetheless, our results appear to be consistent with the works of *Kamiya et al.* [18] and *Lee et al.* [20, 21]. Notably, a strength of our model compared to many works is the achievement of high recall without excessively compromising specificity. Said so, a more useful endeavor would be further understanding which of our models should be preferred in specific clinical or research contexts.

In conclusion, the choice between these models depends on the specific objective. The diffusion-only model offers good performances but is slightly unstable in its metrics. It has 17 features, an optimal number to avoid overfitting, considering 181 subjects.

To achieve a better stability without losing performance the first unfiltered model using both diffusion and network-based metrics should be preferred. In a conservative clinical setting, this model's reduced variance ensures more consistent predictions across diverse patient profiles, making it a reliable tool for standardized assessments.

Lastly, the integrated 34-feature model provides superior discriminative power (ROC-AUC=84.4%) at the cost of higher variance. What this score tells us is that the model in 84% of the cases, when provided with a randomly selected TLE and a randomly selected control, assigns a higher probability of illness to the patient. This model should be chosen when the goal is to separate the classes of TLE and controls without being strictly bound by a fixed classification threshold of 0.5, which means that a subject is classified as a TLE patient only when their predicted output is above that value. The model's strength is its ranking ability rather than a binary "yes/no" output, determined by a 0.5 classification threshold.

Our findings suggest that while microstructural metrics remain the primary drivers for TLE classification, the inclusion of connectomic profiles captures **complementary pathological signals**. Lastly, our multi-level approach not only achieves competitive performance but also allows for a clearer and deeper understanding of the final selected features. The decrease in small-worldness in the Occipital Lobe or in closeness centrality of the Limbic Area within the global network tell us much more about the real consequences of TLE on the brain and human symptoms than a diffusion metric from a ROI of the AAL2 atlas.

# 8 | Conclusion

This thesis provides a comprehensive characterization of structural connectivity alterations in temporal lobe epilepsy (TLE). Specifically, the introduction of **four different levels** of investigation (the global ROI-based, the anatomical macro-regional, the functional networks and the specific edges), inspired by the current literature and applied to conventional diffusion metrics and network-based measures, allows for a deep understanding of the disease.

The hierarchical analysis revealed a pattern of systemic network fragmentation, apparent from the higher number of communities in the global ROI-based network. At the macro-regional level, we identified a pattern of isolation across most of the macro regions, in particular the Occipital and the Limbic/Medial Temporal Lobe (MTL), evidenced by a marked reduction in local efficiency and closeness centrality. This suggests that these regions are topologically sequestered, hindering effective information transfer across the brain. Moreover, evidence of intra-connectivity degradation in regions such as the Frontal, the Occipital and the Parietal, points at a brain-wide disruption extending in regions far from the focal lesion.

Crucially, our investigation into functional networks provided quantitative evidence of the severe impact of TLE on the Default Mode Network (DMN), which shows a significant reduction in global efficiency, after FDR correction. We also observed a distinct *de-hubbing* of critical nodes, specifically the Medial Prefrontal Cortex (mPFC) and the Precuneus. The loss of former super-hubs, reflected by missing right tail of the strength distribution in these regions, drives the global DMN inefficiencies and likely underpins the executive and cognitive deficits observed in chronic patients. Regarding Limbic System, it exhibited a trend toward pathological *regularization*. The contraction in strength variance observed in the Hippocampus and the Temporal Pole suggests a more homogeneous network architecture, which may facilitate the synchronization and propagation of pathological neural activity.

A relevant finding of this structural analysis is the identification of the Hippocampus-mPFC edge as a primary biomarker. The significant reduction, after FDR correction, in this specific connection provides a clear anatomical basis for memory loss and decreased

attention.
Our findings reinforce the contemporary paradigm shift viewing TLE not merely as a focal disorder, but as a large-scale network pathology characterized by widespread systemic reorganization. In general, the disease damages long-range connections and favors local re-entrant ones.

The multi-level framework of investigation represents also a **novel approach to feature extraction** for TLE classification, which bridges the gap between advanced structural connectivity analysis and machine learning-based clinical classification. Rather than feeding a black box model with raw data, we propose a methodology where the feature space is constructed based on the connectivity signatures of TLE.
On the classification front, we developed a Machine Learning classification pipeline integrating the non-parametric Mann-Whitney U test and Spearman correlation for feature selection. The use of conventional diffusion metrics alone, computed across the hierarchical levels as features for an SVM, showed promising results, outperforming the existing literature. In cross-validation, a mean Balanced Accuracy of 74.8%, a mean ROC-AUC of 79.1% and a mean Recall of 80.8% were obtained. Moreover, the integration of local microstructural diffusion metrics with topological network-based properties further improved the pathological predictive signal. Specifically, the best Support Vector Machines (SVM) model trained on both domains reached mean cross-validation values of 84.4% for ROC-AUC, 75.3% for Balanced Accuracy and 78.6% for Recall. Regarding the test set, the model maintained robust performance. Not only do these results support the integration of conventional diffusion and network-based metrics, but they also demonstrate that feature design based on a multi-level hierarchical framework is a novel and successful approach that can effectively capture the complex pathological signatures of TLE.

Despite the strengths and novelty of this work, we cannot omit its limitations. First, while a statistically significant difference in age was observed between groups, both cohorts belong to the same biological life stage (young-to-middle adulthood), suggesting that the observed connectivity changes are primarily driven by pathology rather than aging processes. Future studies could further validate these findings by employing age-matching datasets or age-correction models. In addition, this thesis did not distinguish between right and left TLE patients, which could mask results related to lesion laterality. However, developing a classifier that considers both sides simultaneously offers the advantage of identifying common core pathological markers of TLE regardless of the focus. Furthermore, while a sample size of 181 subjects is substantial for clinical neuroimaging, it remains relatively small for complex machine learning tasks. Replicating this multi-level approach on more extensive datasets would be of great interest.

Additionally, although in the literature deep learning models haven't proven to outperform classical ML algorithms and could further hinder feature interpretability, it would be valuable to explore state of the art models such as graph neural networks, on larger datasets. Lastly, following a growing interest in the literature in multi-modal approaches, a promising direction would be to extend this framework by incorporating functional connectivity.

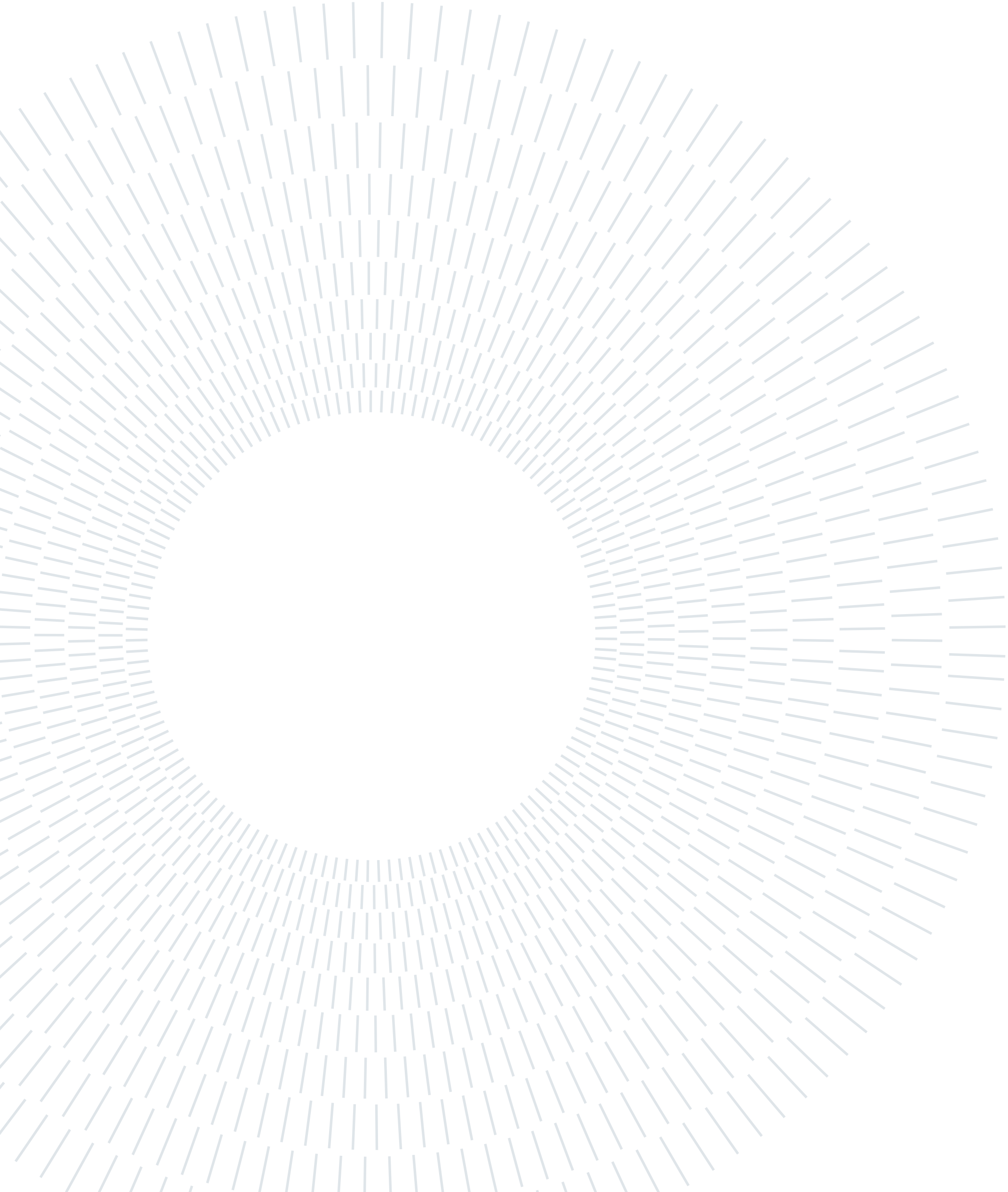

# Bibliography

[1] A. L. Alexander, J. E. Lee, M. Lazar, and A. S. Field. Diffusion tensor imaging of the brain. *Neurotherapeutics*, 4(3):316–329, 2007.

[2] K. Arfanakis, B. P. Hermann, B. P. Rogers, J. D. Carew, M. Seidenberg, and M. E. Meyerand. Diffusion tensor MRI in temporal lobe epilepsy. *Magnetic Resonance Imaging*, 20(7):511–519, 2002. doi: 10.1016/S0730-725X(02)00543-1.

[3] N. Bernasconi, A. Bernasconi, Z. Caramanos, S. B. Antel, F. Andermann, and D. L. Arnold. Mesial temporal damage in temporal lobe epilepsy: a volumetric MRI study of the hippocampus, amygdala and entorhinal cortex. *Brain*, 126(2):462–469, 2003. doi: 10.1093/brain/awg034.

[4] B. C. Bernhardt, Z. Chen, Y. He, A. C. Evans, and N. Bernasconi. Altered network topology in temporal lobe epilepsy: a structural correlation network analysis. *Cerebral Cortex*, 21(9):2148–2159, 2011. doi: 10.1093/cercor/bhq287.

[5] B. C. Bernhardt, N. Bernasconi, S.-J. Hong, S. Dery, and A. Bernasconi. Subregional mesiotemporal network topology is altered in temporal lobe epilepsy. *Cerebral Cortex*, 26(7):3172–3185, 2015.

[6] B. C. Bernhardt, L. Bonilha, and D. W. Gross. Network analysis for a network disorder: the emerging role of graph theory in the study of epilepsy. *Epilepsy & Behavior*, 50:162–170, 2015.

[7] L. Bonilha, C. Rorden, G. Castellano, F. Pereira, P. A. Rio, F. Cendes, and L. M. Li. Voxel-based morphometry reveals excess gray matter loss in patients with mesial temporal lobe epilepsy. *NeuroImage*, 20(3):1641–1651, 2003. doi: 10.1016/s1053-8119(03)00409-4.

[8] L. Bonilha, T. Nesland, G. U. Martz, J. E. Joseph, M. V. Spampinato, J. C. Edwards, and A. Tabesh. Medial temporal lobe epilepsy is associated with neuronal fibre loss and paradoxical increase in structural connectivity of limbic structures. *Journal of Neurology, Neurosurgery & Psychiatry*, 83(9):903–909, 2012. doi: 10.1136/jnnp-2012-302476.

[9] E. Bullmore and O. Sporns. Complex brain networks: graph theoretical analysis of structural and functional systems. *Nature Reviews Neuroscience*, 10(3):186–198, 2009. doi: 10.1038/nrn2575.

[10] D. Cantor-Rivera, A. R. Khan, M. Goubran, S. M. Mirsattari, and T. M. Peters. Detection of temporal lobe epilepsy using support vector machines in multi-parametric quantitative MR imaging. *Computerized Medical Imaging and Graphics*, 46:158–168, 2015.

[11] M. N. DeSalvo, L. Douw, N. Tanaka, C. Reinsberger, and S. M. Stufflebeam. Altered structural connectome in temporal lobe epilepsy. *Radiology*, 270(3):842–848, 2014. doi: 10.1148/radiol.13131044. URL `https://doi.org/10.1148/radiol.13131044`.

[12] R. S. Fisher. Animal models of the epilepsies. *Brain Research Reviews*, 14(3):245–278, 1995. doi: 10.1016/0165-0173(89)90003-9.

[13] V. Frisk and B. Milner. The role of the left hippocampal region in the acquisition and retention of the content of a short story. *Neuropsychologia*, 28(10):1069–1079, 1990. doi: 10.1016/0028-3932(90)90141-8.

[14] T. M. Fruchterman and E. M. Reingold. Graph drawing by force-directed placement. *Software: Practice and Experience*, 21(11):1129–1164, 1991.

[15] M. Jacomy, T. Venturini, S. Heymann, and M. Bastian. Forceatlas2, a continuous graph layout algorithm for handy network visualization designed for the gephi software. *PLOS ONE*, 9(6):e98679, 2014. doi: 10.1371/journal.pone.0098679.

[16] G. James, D. Witten, T. Hastie, and R. Tibshirani. *An Introduction to Statistical Learning: with Applications in R*. Springer Texts in Statistics. Springer, 2nd edition, 2021. ISBN 978-1-0716-1417-4. doi: 10.1007/978-1-0716-1418-1.

[17] B. J. Jellison, A. S. Field, J. Medow, M. Lazar, M. S. Salamat, and A. L. Alexander. Diffusion tensor imaging of cerebral white matter: a pictorial review of physics, fiber tract anatomy, and tumor imaging patterns. *American Journal of Neuroradiology*, 25(3):356–369, 2004.

[18] K. Kamiya, S. Amemiya, Y. Suzuki, N. Kunii, K. Kawai, H. Mori, A. Kunimatsu, N. Saito, S. Aoki, and K. Ohtomo. Machine learning of dti structural brain connectomes for lateralization of temporal lobe epilepsy. *Magnetic Resonance in Medical Sciences*, 15(1):121–133, 2016. doi: 10.2463/mrms.2015-0027.

[19] P. Kwan and M. J. Brodie. Early identification of refractory epilepsy. *New England Journal of Medicine*, 342(5):314–319, 2000. doi: 10.1056/NEJM200002033420503.

[20] D. A. Lee, J. Ko, H. C. Kim, K. J. Shin, B. S. Park, I. H. Kim, J. H. Park, S. Park, and K. M. Park. Identifying juvenile myoclonic epilepsy via diffusion tensor imaging using machine learning analysis. *Journal of Clinical Neuroscience*, 77:105–110, 2020. doi: 10.1016/j.jocn.2020.05.018.

[21] D. A. Lee, H.-J. Lee, and K. M. Park. Identification of focal epilepsy by diffusion tensor imaging using machine learning. *Scientific Reports*, 10(1):1–9, 2020. doi: 10.1038/s41598-020-63713-w.

[22] M. Liu, Z. Chen, C. Beaulieu, and D. W. Gross. Disrupted anatomic white matter network in left mesial temporal lobe epilepsy. *Epilepsia*, 55(5):674–682, 2014. doi: 10.1111/epi.12581.

[23] R. S. McLachlan. Commentary on epilepsy surgery in canada. *Canadian Journal of Neurological Sciences*, 28(1):4–5, 2001. doi: 10.1017/s0317167100001111.

[24] M. S. Mega, J. L. Cummings, S. Salloway, and P. Malloy. The limbic system: an anatomic, phylogenetic, and clinical perspective. *The Journal of Neuropsychiatry and Clinical Neurosciences*, 9(3):315–330, 1997. doi: 10.1176/jnp.9.3.315.

[25] S. Mori and J. Zhang. Principles of diffusion tensor imaging and its applications to basic neuroscience research. *Neuron*, 51(5):527–539, 2006.

[26] W. M. Otte, P. van Eijsden, J. W. Sander, J. S. Duncan, R. M. Dijkhuizen, and K. P. J. Braun. A meta-analysis of white matter changes in temporal lobe epilepsy as studied with diffusion tensor imaging. *Epilepsia*, 53(4):659–667, 2012. doi: 10.1111/j.1528-1167.2012.03425.x.

[27] M. Picot, M. Baldy-Moulinier, J. Daurès, P. Dujols, and A. Crespel. The prevalence of epilepsy and pharmacoresistant epilepsy in adults: a population-based study in a western european country. *Epilepsia*, 49(7):1230–1238, 2008.

[28] H. W. R. Powell et al. Material-specific memory in temporal lobe epilepsy: an fmri study. *Epilepsia*, 46(3):445–452, 2005. doi: 10.1111/j.0013-9580.2005.41404.x.

[29] M. E. Raichle, A. M. MacLeod, P. Z. Snyder, W. J. Powers, D. A. Gusnard, and G. L. Shulman. A default mode of brain function. *Proceedings of the National Academy of Sciences*, 98(2):676–682, 2001. doi: 10.1073/pnas.98.2.676.

[30] M. P. Richardson. Epilepsy networks: a new frontier for epileptology. *Epilepsy Currents*, 12(5):175–179, 2012.

[31] E. T. Rolls, M. Joliot, and N. Tzourio-Mazoyer. Implementation of a anatomical

parcellation of the AAL2 atlas for cerebral visualization and surface-based analysis. *NeuroImage*, 122:1–5, 2015. doi: 10.1016/j.neuroimage.2015.07.075.

[32] M. R. Sarkisian. Overview of the common types of focal and generalized seizures. *Comparative Medicine*, 51(3):201–226, 2001.

[33] J. Soares, P. Marques, V. Alves, and N. Sousa. A hitchhiker's guide to diffusion tensor imaging. *Frontiers in Neuroscience*, 7:31, 2013.

[34] S.-K. Song, S.-W. Sun, M. J. Ramsbottom, C. Chang, J. Russell, and A. H. Cross. Dysmyelination revealed through mri as increased radial (but unchanged axial) diffusion of water. *Neuroimage*, 17(3):1429–1436, 2002.

[35] J. Stretton, P. J. Thompson, E. L. Connally, , and et al. Medial temporal lobe epilepsy and the default mode network. *NeuroImage: Clinical*, 1(1):61–71, 2012. doi: 10.1016/j.nicl.2012.08.001.

[36] T. P. Sutula. Seizure-induced axonal sprouting: assessing connections between injury, local circuits, and epileptogenesis. *Epilepsy Currents*, 2(3):86–91, 2002.

[37] R. D. Thijs, R. Surges, T. J. O'Brien, and J. W. Sander. Epilepsy in adults. *The Lancet*, 393(10172):689–701, 2019. doi: 10.1016/S0140-6736(18)32596-0.

[38] D. J. Watts and S. H. Strogatz. Collective dynamics of 'small-world' networks. *Nature*, 393(6684):440–442, 1998. doi: 10.1038/30918.

[39] Y. Xu et al. Altered structural and functional brain networks in temporal lobe epilepsy: A systematic review. *Frontiers in Neurology*, 13:1020455, 2022. doi: 10.3389/fneur.2022.1020455.

[40] F.-C. Yeh and W.-Y. I. Tseng. NTU-90: A high-resolution white matter atlas with Q-space diffeomorphic reconstruction. *NeuroImage*, 58(1):91–99, 2011. doi: 10.1016/j.neuroimage.2011.06.021.

[41] F.-C. Yeh, V. J. Wedeen, and W.-Y. I. Tseng. Generalized $Q$-sampling imaging. *IEEE Transactions on Medical Imaging*, 29(9):1626–1635, 2010. doi: 10.1109/TMI.2010.2045126.

[42] F.-C. Yeh, L. Liu, T. K. Hitchens, and Y. L. Wu. Mapping generalized susceptibility-induced distortions in the human brain. *Magnetic Resonance in Medicine*, 77(2):603–612, 2017. doi: 10.1002/mrm.26131.

[43] F. Zhang, A. Daducci, Y. He, S. Schiavi, C. Seguín, R. E. Smith, C.-H. Yeh, T. Zhao,

and L. J. O'Donnell. Quantitative mapping of the brain's structural connectivity using diffusion mri tractography: A review. *NeuroImage*, 249:118870, 2022.

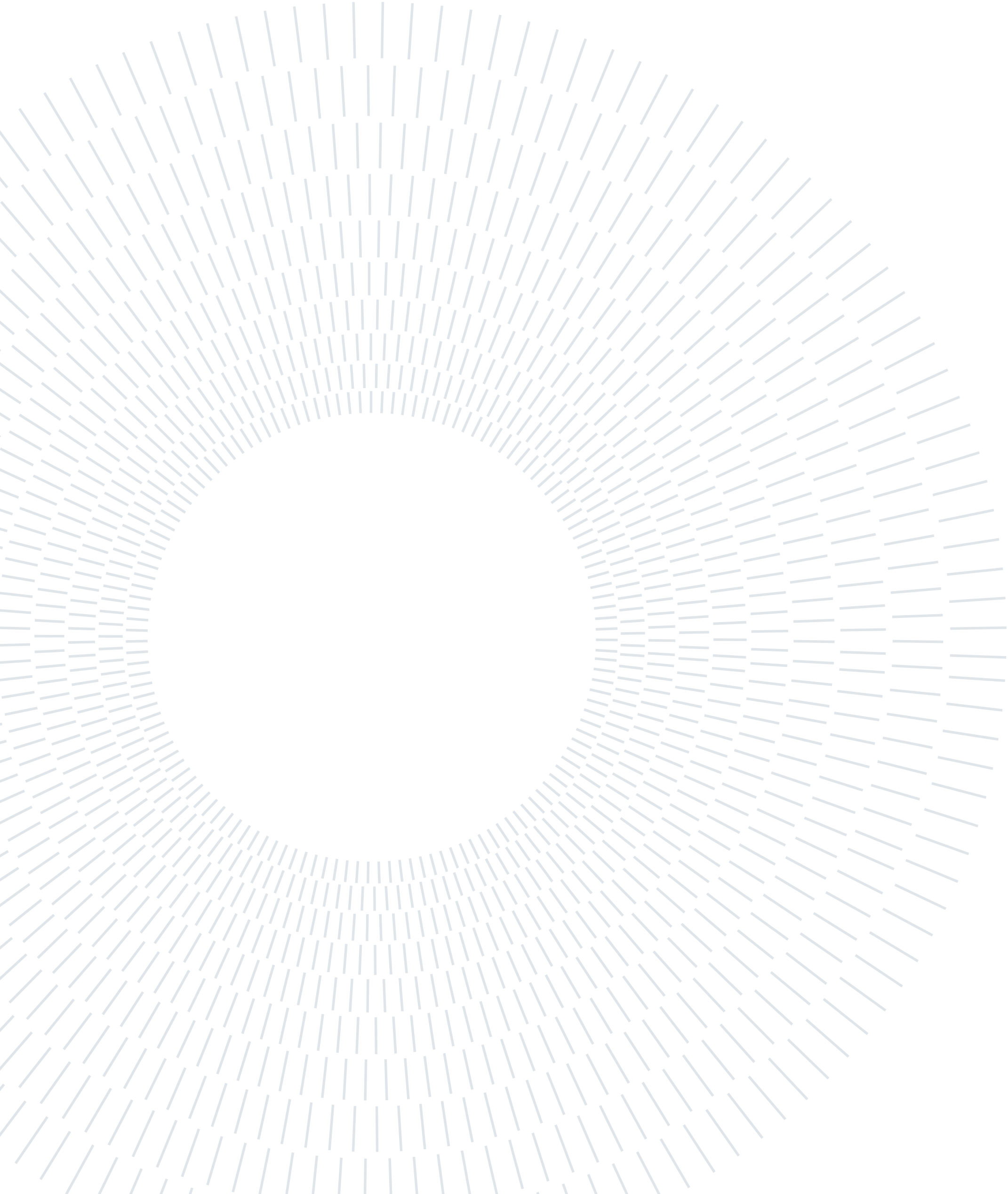

# Appendix A: Fundamentals of MRI Signal and Contrast

The MRI signal is primarily derived from the behavior of hydrogen nuclei (protons) when placed in a strong external magnetic field ($B_0$) and disturbed by radiofrequency (RF) pulses. The return of these protons to their equilibrium state is known as *relaxation*, which occurs through two independent processes: $T_1$ and $T_2$. The contrast of an image is determined by how the timing parameters of the pulse sequence Repetition Time ($TR$) and Echo Time ($TE$)—interact with these relaxation times.

## A.1 Longitudinal Relaxation ($T_1$) and $TR$

$T_1$ relaxation, also known as spin-lattice relaxation, is the process by which protons recover their magnetization along the direction of the $B_0$ field.

After a RF pulse rotates of 90 degrees the magnetization vector, tipping it into the transverse plane, protons release energy to the surrounding environment to return to their original longitudinal alignment.

Being Repetition Time ($TR$) the interval between successive excitation pulses,

- If $TR$ is short, tissues with long $T_1$(like CSF) do not have enough time to recover their magnetization before the next pulse, resulting in a lower signal (appearing dark).
- If $TR$ is long, most tissues fully recover, and the $T_1$ contrast is minimized.

## A.2 Transverse Relaxation ($T_2$) and $TE$

$T_2$ relaxation, or spin-spin relaxation, describes the loss of phase coherence among protons in the transverse plane due to local magnetic field fluctuations.

Immediately after an RF pulse, protons rotate in phase. Due to interactions between neighboring spins, they begin to "dephase," and the transverse signal decays.

Being Echo Time ($TE$) the time interval between the excitation pulse and the peak of the signal (echo) being read by the scanner,

- If $TE$ is short, the signal is captured before significant dephasing occurs, minimizing $T_2$ effects.
- If $TE$ is long, tissues with short $T_2$ (like muscle or white matter) lose their signal quickly, while tissues with long $T_2$ (like CSF or edema) remain bright.

## A.3 Summary of Weighting Parameters

By manipulating $TR$ and $TE$, the MRI sequence can be "weighted" to highlight specific tissue properties. The following table summarizes the standard configurations:

| **Image Weighting** | **TR** | **TE** | **Main Application** |
|---|---|---|---|
| $T_1$-Weighted | Short | Short | Anatomy and structural detail |
| $T_2$-Weighted | Long | Long | Pathology, edema, and CSF (bright) |
| Proton Density (PD) | Long | Short | Water concentration detail |

**Table 8.1:** Standard MRI weighting parameters.

In the context of Diffusion MRI, a sequence with long $TR$ and long $TE$ is typically used to minimize $T_1$ effects and allow enough time for the application of diffusion gradients. Consequently, the reference image (where $b = 0$) in a diffusion dataset is inherently a $T_2$-weighted image.

# Appendix B: Classical Diffusion Metrics and Tractography with DSI Studio

As detailed in the main text, classical diffusion metrics were extracted for each Region of Interest (ROI) of the AAL2 atlas. These metrics were processed for every subject, using the respective .qsrd.fz files within DSI Studio. Here the script of the main function:

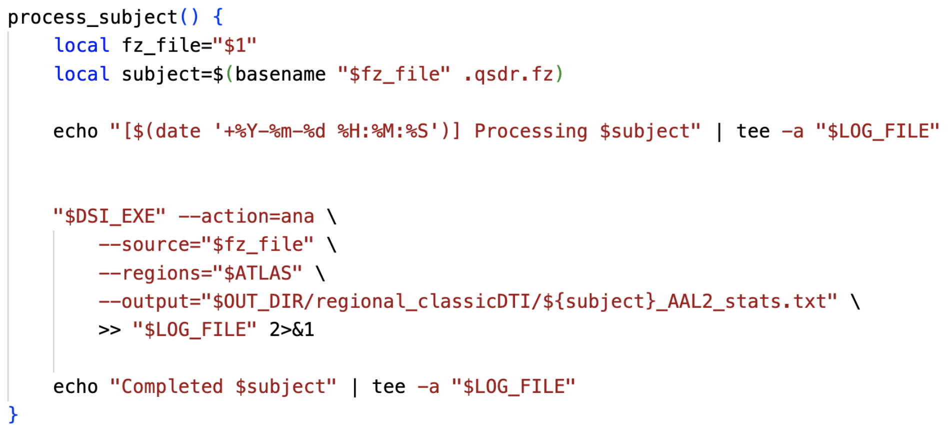

```
process_subject() {
    local fz_file="$1"
    local subject=$(basename "$fz_file" .qsdr.fz)

    echo "[$(date '+%Y-%m-%d %H:%M:%S')] Processing $subject" | tee -a "$LOG_FILE"


    "$DSI_EXE" --action=ana \
        --source="$fz_file" \
        --regions="$ATLAS" \
        --output="$OUT_DIR/regional_classicDTI/${subject}_AAL2_stats.txt" \
        >> "$LOG_FILE" 2>&1

    echo "Completed $subject" | tee -a "$LOG_FILE"
}
```

**Figure 8.1:** Definition of the function to extract classic diffusion metrics

We also performed Deterministic Tractography and, for a given atlas, computed a connectivity matrix, reflecting the count of fibers connecting two ROIs for each subject. This is the definition of the function:

```
process_subject() {
    local fz_file="$1"
    local subject=$(basename "$fz_file" .qsdr.fz)
    local temp="$OUT_DIR/temp_${subject}.tt.gz"

    echo "[$(date +%H:%M:%S)] Elaborate: $subject" | tee -a "$LOG_FILE"

    "$DSI_EXE" --action=trk \
        --source="$fz_file" \
        --method=0 \
        --seed_count=$SEED_COUNT \
        --thread_count=1 \
        --output="$temp" \
        --connectivity="$ATLAS" \
        --connectivity_type=count \
        --connectivity_mni \
        >> "$LOG_FILE" 2>&1

    # Move final output
    mv "${temp}.HCP-MMP_mni.number_of_tracts.connectivity.mat" \
       "$OUT_DIR/connectivity_matrices/${subject}_connectivity.mat"

    mv "${temp}.HCP-MMP_mni.number_of_tracts.connectogram.txt" \
       "$OUT_DIR/connectivity_matrices/${subject}_connectogram.txt"

    # Cleanup
    rm -f "$temp" "${temp}.HCP-MMP_mni."*

    echo "Completato: $subject" | tee -a "$LOG_FILE"
}
```

**Figure 8.2:** Definition of the function to perform Tractography and compute the connectivity matrices

# Appendix C: Local Network Metrics - Significant Differences

The following table refers to Level 1 in the described hierarchical framework and reports all nodal graph metrics showing a significant difference between control and TLE groups ($p < 0.05$, uncorrected).

**Table 8.2:** Significant differences in super-node metrics between Healthy Controls (HC) and TLE patients (Uncorrected $p < 0.05$). Each super-node represents an anatomical macro-region in the whole-brain supergraph.

| **Brain Region (ROI)** | **Graph Metric** | **Direction** | ***p*-value** | ***p*-adj (FDR)** |
|---|---|---|---|---|
| Precentral L | Clustering (B) | HC > TLE | 0.0201 | 0.5285 |
| | Local Eff. (W) | HC > TLE | 0.0227 | 0.5285 |
| | Local Eff. (B) | HC > TLE | 0.0192 | 0.5285 |
| Precentral R | Local Eff. (B) | HC > TLE | 0.0276 | 0.5285 |
| | Clustering (B) | HC > TLE | 0.0276 | 0.5285 |
| Frontal Sup 2 L | Local Eff. (W) | HC > TLE | 0.0088 | 0.5285 |
| | Clustering (B) | HC > TLE | 0.0204 | 0.5285 |
| | Local Eff. (B) | HC > TLE | 0.0194 | 0.5285 |
| Frontal Sup 2 R | Local Eff. (W) | HC > TLE | 0.0345 | 0.5285 |
| Frontal Mid 2 L | Local Eff. (W) | HC > TLE | 0.0017 | 0.3971 |
| | Local Eff. (B) | HC > TLE | 0.0033 | 0.4472 |
| | Clustering (B) | HC > TLE | 0.0032 | 0.4472 |
| Frontal Inf Oper L | Clustering (B) | HC > TLE | 0.0143 | 0.5285 |
| | Local Eff. (B) | HC > TLE | 0.0144 | 0.5285 |
| Supp Motor Area R | Degree | HC > TLE | 0.0342 | 0.5285 |
| | Betweenness | TLE > HC | 0.0413 | 0.5285 |
| Frontal Sup Medial R | Degree | HC > TLE | 0.0002 | 0.0877 |
| | Strength | HC > TLE | 0.0010 | 0.3080 |
| | Local Eff. (W) | TLE > HC | 0.0183 | 0.5285 |
| Frontal Sup Medial L | Degree | HC > TLE | 0.0193 | 0.5285 |
| Frontal Med Orb L | Degree | HC > TLE | 0.0077 | 0.5285 |
| | Strength | HC > TLE | 0.0192 | 0.5285 |

Continued on next page

**Table 8.2 – Continued from previous page**

| Brain Region (ROI) | Graph Metric | Direction | $p$-value | $p$-adj (FDR) |
|---|---|---|---|---|
| Frontal Med Orb R | Degree | HC > TLE | 0.0002 | 0.0877 |
| | Strength | HC > TLE | 0.0077 | 0.5285 |
| | Closeness | HC > TLE | 0.0222 | 0.5285 |
| Rectus L | Strength | HC > TLE | 0.0313 | 0.5285 |
| | Closeness | HC > TLE | 0.0284 | 0.5285 |
| Rectus R | Degree | HC > TLE | 0.0273 | 0.5285 |
| OFCant R | Degree | HC > TLE | 0.0030 | 0.4472 |
| | Strength | HC > TLE | 0.0048 | 0.5285 |
| | Closeness | HC > TLE | 0.0376 | 0.5285 |
| | Betweenness | HC > TLE | 0.0391 | 0.5285 |
| | Local Eff. (W) | TLE > HC | 0.0368 | 0.5285 |
| Insula R | Local Eff. (B) | HC > TLE | 0.0138 | 0.5285 |
| | Clustering (B) | HC > TLE | 0.0138 | 0.5285 |
| Hippocampus L | Degree | HC > TLE | 0.0366 | 0.5285 |
| Calcarine R | Degree | HC > TLE | 0.0236 | 0.5285 |
| Lingual L | Degree | HC > TLE | 0.0094 | 0.5285 |
| | Strength | HC > TLE | 0.0397 | 0.5285 |
| | Betweenness | HC > TLE | 0.0115 | 0.5285 |
| Occipital Mid L | Clustering (W) | TLE > HC | 0.0203 | 0.5285 |
| Occipital Sup L | Degree | HC > TLE | 0.0141 | 0.5285 |
| Occipital Sup R | Degree | HC > TLE | 0.0119 | 0.5285 |
| Fusiform L | Betweenness | HC > TLE | 0.0374 | 0.5285 |
| Postcentral L | Betweenness | TLE > HC | 0.0336 | 0.5285 |
| Postcentral R | Degree | HC > TLE | 0.0147 | 0.5285 |
| | Clustering (W) | TLE > HC | 0.0376 | 0.5285 |
| Parietal Sup L | Degree | HC > TLE | 0.0082 | 0.5285 |
| | Clustering (W) | TLE > HC | 0.0324 | 0.5285 |
| Parietal Sup R | Clustering (W) | TLE > HC | 0.0403 | 0.5285 |
| Parietal Inf L | Clustering (W) | TLE > HC | 0.0272 | 0.5285 |
| Angular R | Degree | HC > TLE | 0.0255 | 0.5285 |
| Paracentral Lob R | Clustering (B) | HC > TLE | 0.0327 | 0.5285 |
| | Local Eff. (B) | HC > TLE | 0.0331 | 0.5285 |
| Thalamus L | Betweenness | TLE > HC | 0.0459 | 0.5510 |
| Heschl L | Clustering (W) | TLE > HC | 0.0397 | 0.5285 |
| Temporal Sup R | Betweenness | HC > TLE | 0.0312 | 0.5285 |
| | Strength | HC > TLE | 0.0473 | 0.5600 |
| Temporal Pole Sup L | Clustering (W) | TLE > HC | 0.0070 | 0.5285 |
| Temporal Pole Sup R | Clustering (W) | TLE > HC | 0.0485 | 0.5600 |
| Temporal Pole Mid L | Degree | HC > TLE | 0.0426 | 0.5344 |
| | Clustering (W) | TLE > HC | 0.0222 | 0.5285 |
| Cerebelum Crus1 L | Strength | HC > TLE | 0.0208 | 0.5285 |

Continued on next page

**Table 8.2 – Continued from previous page**

| **Brain Region (ROI)** | **Graph Metric** | **Direction** | ***p*-value** | ***p*-adj (FDR)** |
|---|---|---|---|---|
| Cerebelum Crus1 R | Local Eff. (B) | HC > TLE | 0.0374 | 0.5285 |
| | Clustering (B) | HC > TLE | 0.0372 | 0.5285 |
| Cerebelum Crus2 L | Strength | HC > TLE | 0.0411 | 0.5285 |
| Cerebelum 4 5 L | Local Eff. (W) | HC > TLE | 0.0054 | 0.5285 |
| | Strength | HC > TLE | 0.0376 | 0.5285 |
| Cerebelum 7b L | Degree | HC > TLE | 0.0328 | 0.5285 |
| | Strength | HC > TLE | 0.0217 | 0.5285 |
| Cerebelum 10 L | Local Eff. (W) | HC > TLE | 0.0381 | 0.5285 |
| Vermis 3 | Local Eff. (W) | HC > TLE | 0.0262 | 0.5285 |
| Vermis 4 5 | Closeness | HC > TLE | 0.0392 | 0.5285 |
| Vermis 7 | Local Eff. (B) | HC > TLE | 0.0246 | 0.5285 |
| | Clustering (B) | HC > TLE | 0.0248 | 0.5285 |

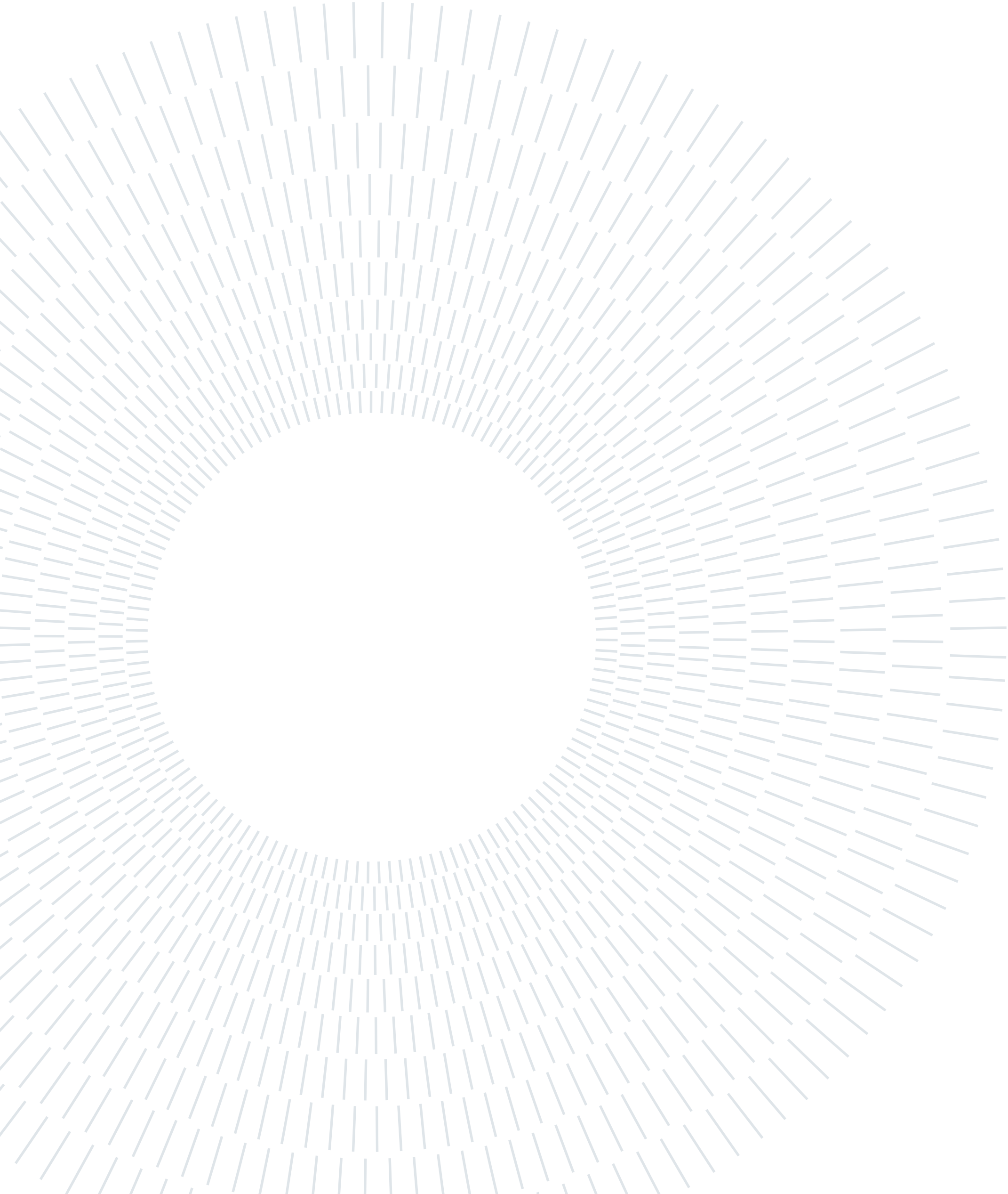

# List of Figures

# List of Tables